Interaction-induced localization and constrained dynamics in polar lattice gases

Von der QUEST-Leibniz-Forschungsschule
der Gotttfried Wilhelm Leibniz Universität Hannover
Zur Erlangung des Grades

Doktor der Naturwisseschaften
- Dr. rer. nat. -

genehmigte Dissertation
von

M. Sc. Wei-Han Li

2021

Referent:
Prof. Dr. Luis Santos (Leibniz Universität Hannover)

Korreferenten:
Prof. Dr. Jakub Zakrzewski (Jagiellonian Universität Krakau)
Dr. Luca Barbiero (Politecnico di Torino)

Tag der Disputation: 13.12.2021

Acknowledgements

This work is realized with significant contributions from our group members, whom I must acknowledge. I would like to thank Daniel Edler for his comprehensive assistance with programming and software applications, and Arya Dhar for his proficient t-DMRG skills that provides figures in Chapter 3. I thank as well Xiaolong Deng, for the fruitful discussions on disordered systems, and Prof. Luis Santos, for figure 6.7 (c) and 6.2 (b), and most importantly, for his guidance in both principle and practical ways.

Abstract

This Thesis is devoted to the study of particle mobility in polar lattice gases, that is, systems of particles with a large magnetic or electric dipole moment loaded in a deep optical lattice, which may move between sites via hopping. Our detailed analysis of different scenarios shows that inter-site dipole-dipole interactions largely handicap particle motion, resulting in a lattice dynamics that differs qualitatively, and not only quantitatively, to that expected both for non-dipolar gases, and for systems with exclusively nearest-neighbor interactions. We first discuss how the formation of dynamically-bound nearest-neighbor dimers for large enough dipolar interactions, results in an anomalously slow dynamics and quasi-localization due to the formation of dimer clusters. Moreover, we show that even modest inter-site interactions result in the formation of self-bound lattice droplets. We then extend the discussion to general states, placing the discussion in the frame of current studies on disorder-free localization, dynamical constraints and Hilbert-space fragmentation. We are particularly concerned with the difference between a polar lattice gas and a system with purely nearest-neighbor interactions. In the latter, strong-enough inter-site interactions lead to fragmentation, but resonant dynamics remains possible within a fragment, precluding disorder-free spatial localization. In contrast, in a polar gas, the presence of the dipolar tail shatters the Hilbert space, and in addition disrupts the resonant mechanism characteristic of the nearest-neighbor model. As a result, we show that the particle dynamics is dramatically slowed-down, and eventually localized in absence of any disorder, for interaction strengths within reach of experiments. Furthermore, although most of the results of this Thesis concern one-dimensional systems, most of the results can be extrapolated to higher dimensions. Moreover, we show that the dynamics in two-dimensional polar lattice gases presents peculiar features, due to the fact that dynamically-bound dimers experience a lattice different than that of individual particles. In particular, dimers in triangular lattices move in an effective kagome lattice, presenting an effective flat band. We show that the presence of flat-band dimers results in a peculiar multi-scaled quantum walk dynamics, and in a long-lived memory of initial conditions in absence of any disorder. The results in this Thesis open exciting perspectives in what concerns particle dynamics and disorder-free localization in on-going and future

experiments with magnetic atoms and polar molecules in optical lattices. Furthermore, our findings may be easily extrapolated to other power-law interactions, as those realizable using trapped ions.

The structure of this Thesis is as follows. In Chapter 1 we introduce key concepts of the physics of quantum gases in optical lattices. Chapter 2 discusses relevant ideas concerning ergodicity and localization in quantum systems, which are of interest for the rest of the Thesis. Chapter 3 is devoted to the analysis of dynamically-bound dimers in polar lattice gases, and in particular on how dimers clusterize due to the key role played by the dipolar tail. In Chapter 3 we discuss as well the formation of self-bound lattice droplets under conditions currently achievable experimentally. In Chapter 4 we focus on the analysis of localization in models with interactions only to nearest neighbors, reviewing some key ideas, and in particular the concept of Hilbert space fragmentation due to the conservation of nearest-neighbor links, and the crucial mechanism for resonant motion within a Hilbert space fragment. In Chapter 5 we show that the dipolar tail plays a crucial role in polar lattice gases, since on one side it shatters the Hilbert-space, and on the other side it disrupts the resonant motion mechanism characteristic of the nearest-neighbor model. Finally, in Chapter 6 we analyze the peculiar dynamics of nearest-neighbors in two-dimensional lattices. The Thesis ends in Chapter 7, where we discuss our conclusions and future perspectives.

Keywords:

Localization, Quantun Statistics, Polar lattice gases.

Contents

Chapter 1

Quantum gases in optical lattices

In the past two decades, spectacular experimental developments on ultra cold gases [1] have considerably advanced the field of quantum (analog) simulation of strongly-correlated systems [2, 3, 4], a realm previously restricted to condensed-matter and nuclear physics. This progress has been to a very large extent based on one hand on the ability to tune the interaction strength and its sign in atomic gases by means of Feshbach resonances [5, 6], and on the other hand on the capability to modify the dimensionality and particle mobility by means of optical potentials, especially optical lattices [7, 8, 9, 10, 11, 12]. As a result, strong correlations can be created even in dilute gases [1].

Quantum gases in optical lattices provide an extraordinarily controllable scenario for the study of many-body quantum systems under basically ideal conditions in which a desired Hamiltonian is cleanly realized. Major developments in this very active field include the realizations of the Bose-Hubbard model [13, 14, 15], the Fermi Hubbard model [16, 17], the Heisenberg-Ising model [18, 19, 20], or the periodically driven Hubbard model [21]. In this chapter we introduce the basics of optical lattices, as well as of the realization of lattice models with them. Due to its interest for this Thesis, we will pay special attention to polar lattice gases, and the realization of the extended Hubbard model.

1.1. Periodic optical potentials

A periodic optical potential is generated by the interference pattern created by two or more laser beams. The resulting laser profile results, via dipole force, in a conservative potential in which sufficiently cold quantum gases may be loaded [1, 7, 8]. The simplest possible periodic optical potential is formed by overlapping two counter-propagating beams. For a Gaussian laser profile along the z direction, this results in a trapping po-

tential of the form $V(r,z) \sim -V_0 e^{-2r^2/u^2(z)} \sin^2(kz)$, where V_0 is the maximum depth of the lattice potential, $k = 2\pi/\lambda$ is the wave vector, r is the distance from the center of the beam, and $u(z) = u_0\sqrt{1+z^2/z_R}$ is the $1/e^2$ radius with the Rayleigh length $z_R = \pi u_0^2/\lambda$. The resulting potential at the beam center has hence a spatial period $\lambda/2$, and hence atoms in optical lattices experience a periodic potential similar to that exerted by ions on electrons in solid-state systems. Periodic potentials in two dimensions can be formed by overlapping standing waves along different (e.g., orthogonal) directions, avoiding undesired interferences between them. Such a potential confines atoms into arrays of tightly confining 1D tubes (see Fig. 1.1 (a)). Interestingly, for deep lattices, atoms can move only along a given tube, allowing for the study of 1D strongly correlated gases. The simplest 3D lattice potential is provided by the overlapping of three orthogonal standing waves. For distances much smaller than the beam waist, the potential is approximately given by the sum of a homogeneous lattice potential $V(x,y,z) \sim V_0(\sin^2 kx + \sin^2 ky + \sin^2 kz)$ and a harmonic confinement due to the Gaussian beam profiles. Lattices of different geometries have been realized, including triangular [9], kagome [10], graphene-like [11], or even quasi-crystalline [12].

Spin-dependent lattices can be created as well, such that atoms with different magnetic sub-levels experience different potentials [22]. Using a standing wave configuration formed by two counter-propagating laser beams with linear polarization vectors forming an angle θ, the resulting laser field may be decomposed into a superposition of a spin-up and spin-down polarized standing waves, giving rise to lattice potentials $V_+ = V_0 \cos^2(kx+\theta/2)$ and $V_- = V_0 \cos^2(kx-\theta/2)$, which may be in this way employed as spin-dependent potentials for different sub-levels.

1.2. The Bose-Hubbard model

1.2.1. Wannier functions

We consider at this point the case of an infinite periodic potential (neglecting any additional intensity profile of the laser beams). The single-particle eigenstates for the energy band n are given by the Bloch functions $\phi_{\mathrm{n},\mathbf{q}}(\mathbf{r})$, where $\mathbf{q}$ is the quasi-momentum. Bloch functions are however extended over the whole lattice, and hence they are not particularly suitable for the study of deep lattices, where particles have a very reduced mobility. A more useful single-particle basis is provided by the Wannier functions, $\mathrm{w_n}(\mathbf{r}-\mathbf{R})$, centered at site $\mathbf{R}$. The Wannier functions are connected via Fourier transform to

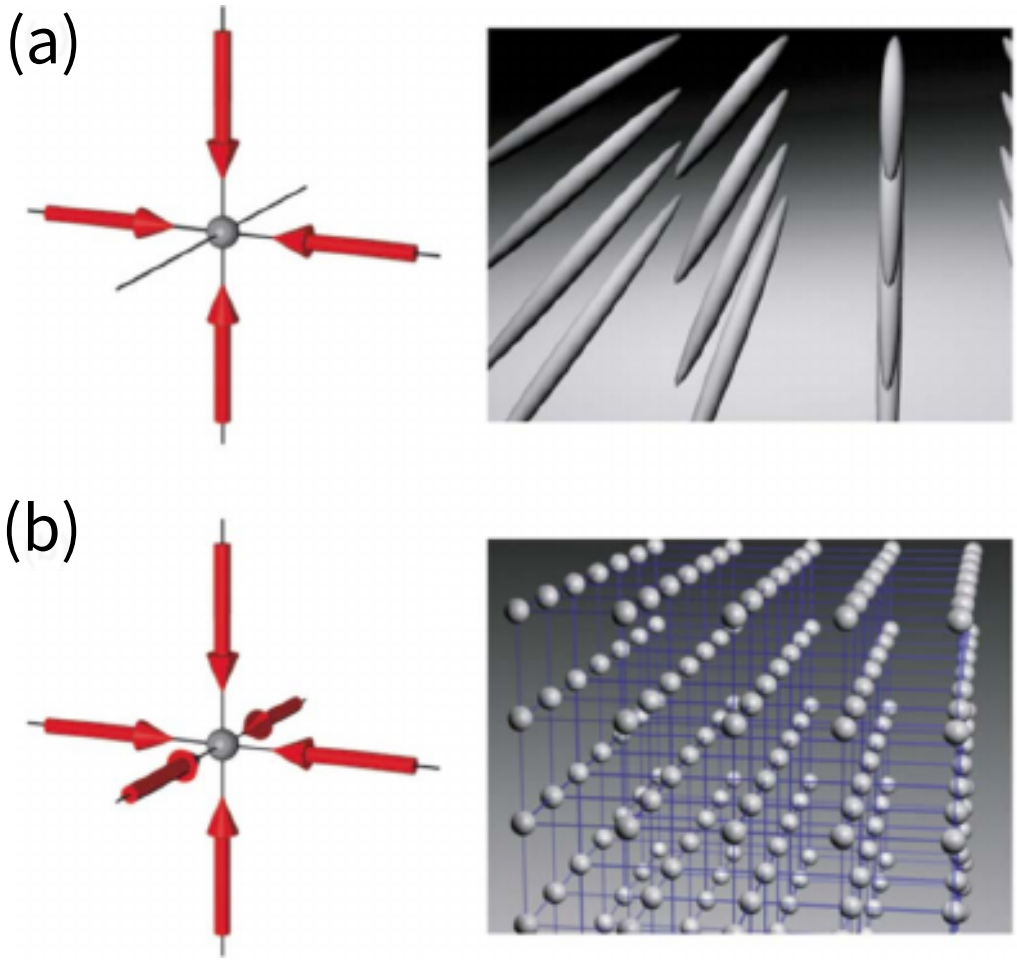

Figure 1.1: Optical lattices. (a) Two- and (b) three-dimensional optical lattices formed by superimposing two or three orthogonal standing waves. For a 2D optical lattice, the atoms are confined to an array of tightly confining 1D potential tubes, whereas in the 3D case the optical lattice can be approximated by a 3D cubic array of tightly-confining harmonic-oscillator potentials at each lattice site. Figure from Ref. [1].

the Bloch functions, $\phi_{\mathrm{n},\mathbf{q}}(\mathbf{r}) = \sum_{\mathbf{R}} \mathrm{w}_{\mathrm{n}}(\mathbf{r}-\mathbf{R})e^{i\mathbf{q}\cdot\mathbf{R}}$, where $\mathbf{R}$ is the lattice vector. For all bands n and sites $\mathbf{R}$, Wannier functions form a complete basis, and the field operator of an atom can be expanded in the form

$$\hat{\psi}(\mathbf{r}) = \sum_{\mathrm{n},\mathbf{R}} \mathrm{w}_{\mathrm{n}}(\mathbf{r}-\mathbf{R})\hat{a}_{\mathrm{n},\mathbf{R}}.$$

For a deep lattice, the gap between the lowest and second energy bands can be typically considered much larger than any other energy scale in the problem, and hence we can restrict our discussion to the lowest band.

1.2.2. Hopping

Using the expansion of the field operator in the basis of Wannier functions of the lowest band, the single-particle Hamiltonian

$$H = \int d^3\mathbf{r}\hat{\psi}^\dagger(\mathbf{r}) \left[\frac{-\hbar^2\nabla^2}{2m} + V_{latt}(\mathbf{r})\right] \hat{\psi}(\mathbf{r}), \tag{1.1}$$

with $V_{latt}(\mathbf{r})$ the lattice potential, can be rewritten in the form

$$H = -\sum_{\mathbf{R},\mathbf{R}'} J(\mathbf{R}-\mathbf{R}')\hat{a}^\dagger_{\mathbf{R}}\hat{a}_{\mathbf{R}'}. \tag{1.2}$$

where we do not write any longer the band index n = 0. In the previous equation,

$$J(\mathbf{R}-\mathbf{R}') = -\int d^3\mathbf{r} w(\mathbf{r}-\mathbf{R})^* \left[\frac{-\hbar^2\nabla^2}{2m} + V_{latt}(\mathbf{r})\right] w(\mathbf{r}-\mathbf{R}'), \tag{1.3}$$

is the hopping rates between the sites centers at $\mathbf{R}$ and $\mathbf{R}'$. For deep lattices the Wannier functions are strongly localized in a given site, and hence hopping reduces to only nearest-neighbor terms, leading to the tight-binding model

$$H_{hop} = -J \sum_{<i,j>} \left(\hat{a}^\dagger_i \hat{a}_j + H.c.\right), \tag{1.4}$$

where $< i, j >$ denotes pairs of nearest-neighbor sites, and we have assumed a uniform hopping rate in the lattice. By solving the corresponding Mathieu equation, it is possible to obtain an analytical expression for the hopping amplitude [23]

$$J = \frac{4}{\sqrt{\pi}} E_k \left(\frac{V_0}{E_k}\right)^{3/4} e^{-2\left(\frac{V_0}{E_k}\right)^{1/2}}, \tag{1.5}$$

where $E_k = \frac{\hbar^2 k^2}{2m}$ is the recoil energy associated to the laser photons. The associated band dispersion may be easily evaluated from the Fourier transform of the Hamiltonian, and it is of the form: $\varepsilon(\mathbf{q}) = -2J\sum_{i=x,y,z}\cos q_i d$, with $d = \pi/k$. Note that $J > 0$ and hence the lowest band energy occurs for $q = 0$.

1.2.3. Interactions

Short-ranged s-wave interactions are well described by a pseudopotential $g\delta(\mathbf{r})$, where $g = \frac{4\pi\hbar^2}{m}a$ is the interaction coupling constant, with a the s-wave scattering length, and m the particle mass. The sign and magnitude of the scattering length may be modified

by means of Feshbach resonances [24].

The interaction energy is hence given by the Hamiltonian

$$H_{int} = \frac{g}{2}\int d^3\mathbf{r}\hat{\psi}^\dagger(\mathbf{r})\hat{\psi}^\dagger(\mathbf{r})\hat{\psi}(\mathbf{r})\hat{\psi}(\mathbf{r}), \tag{1.6}$$

As above, we may expand on the basis of Wannier functions. Assuming bosonic particles, and neglecting interactions between different sites, due to the strong localization of the Wannier functions for deep lattices, the interaction Hamiltonian acquires the form:

$$H_{int} = \frac{U}{2}\sum_j \hat{n}_j(\hat{n}_j - 1), \tag{1.7}$$

where $U = g\int |\mathrm{w}_0(\mathbf{r})|^4 d^3\mathbf{r}$, and $\hat{n}_j = \hat{a}_j^\dagger \hat{a}_j$ is the number operator of atoms on the same lattice site. Obviously, the on-site interaction term is only nonzero if $n_j \geq 2$. Note that the interaction U is the same for all sites, since we assume that the lattice is spatially homogeneous. To a good approximation, U may be easily computed by approximating at the lattice minima the lattice potential by an effective harmonic oscillator, with frequency $\omega_{eff} = 2\sqrt{\frac{V_0}{E_k}}\frac{E_k}{\hbar}$. As a side remark, note that at Feshbach resonances higher-band physics may become relevant [16].

Equation (1.4) together with Eq. (1.7) results in the Bose-Hubbard model

$$H = -J\sum_{<i,j>}\left(\hat{a}_i^\dagger \hat{a}_j + H.c.\right) + \frac{U}{2}\sum_j \hat{n}_j(\hat{n}_j - 1) - \mu\sum_j \hat{n}_j, \tag{1.8}$$

where we have added the chemical potential μ.

1.3. Ground-state phases of the Bose-Hubbard model

The relatively simple Bose-Hubbard Hamiltonian is characterized by the competition between lattice hopping, which favors mobility, and on-site interactions, which have a localizing effect. This competition results in an interesting ground-state physics, which we briefly discuss in this section.

1.3.1. Ground-state phase diagram

We first consider the case without hopping, $H = \sum_j h_j$, with $h_j = \frac{U}{2}\hat{n}_j(\hat{n}_j - 1) - \mu\hat{n}_j$. The eigenstates of h_j are Fock states $|n\rangle$ with a definite number of bosons n per site. These states have an energy $E_n^{(0)} = \frac{U}{2}n(n-1) - \mu n$. The energy is then minimized for

$n = \left[\frac{\mu}{U} - \frac{1}{2}\right]$, where $[\ldots]$ means the closest integer. Hence in absence of hopping the ground-state is characterized by a fixed number of atoms per site $\bar{n}$ for $\bar{n} - 1 < \mu/U < \bar{n}$.

For a finite hopping, we may introduce the mean-field decoupling $\hat{a}_i^\dagger \hat{a}_j \simeq -\psi^2 + \psi\left(\hat{a}_i^\dagger + \hat{a}_j\right)$, with $\psi = \langle \hat{a}_j^\dagger \rangle = \langle \hat{a}_j \rangle$. In this approximation we neglect the terms of second order fluctuations $\delta\hat{a}_j = \hat{a}_j - \psi$. The hopping Hamiltonian may then be re-written in the form:

$$H_{TUN} \simeq zJ \sum_j \left(\psi^2 - \psi\left(\hat{a}_j^\dagger + \hat{a}_j\right)\right), \tag{1.9}$$

where z is the coordination number, that is, the number of nearest-neighbors in the particular lattice geometry considered. We may then write the overall Hamiltonian in a decoupled form: $H \simeq \sum_j \hat{h}_j$, with $\hat{h}_j = \hat{h}_j^{(0)} + \hat{V}_j$, $\hat{h}_j^{(0)} = \frac{U}{2}\hat{n}_j(\hat{n}_j - 1) - \mu\hat{n}_j + zJ\psi^2$ and $\hat{V}_j = -zJ\psi(\hat{a}_j^\dagger + \hat{a}_j)$.

Assuming $\hat{V}_j$ as a perturbation, we may perform perturbation theory, to obtain the corrected energy of the ground state $|\bar{n}\rangle$: $E_{\bar{n}} = E_{\bar{n}}(J = 0) + zJr_{\bar{n}}^2\psi^2 + \mathcal{O}(\psi^4)$, with

$$r_{\bar{n}} = 1 + \frac{zJ(\bar{n}+1)}{\mu - U\bar{n}} - \frac{zJ\bar{n}}{\mu - U(\bar{n}-1)}. \tag{1.10}$$

For $r_{\bar{n}} < 0$ the system minimizes the energy by having $\psi \neq 0$, characterizing the so-called superfluid phase. In contrast, for $r_{\bar{n}} > 0$, the energy is minimized by $\psi = 0$, and the system is in an insulating phase known as Mott insulator. The separatrix between both phases is given by $r_{\bar{n}} = 0$, which leads to the condition:

$$\frac{\mu_\pm}{U} = \frac{1}{2}\left[2\bar{n} - 1 - \frac{zJ}{U}\right] \pm \frac{1}{2}\sqrt{1 - 2\frac{zJ}{U}(1+\bar{n}) + \left(\frac{zJ}{U}\right)^2}. \tag{1.11}$$

The Mott region lies between these two curves, which in the plane $(J/U, \mu/U)$ form the so-called Mott lobes (see Fig. 1.2(a)). Note that for $J = 0$ the Mott lobe for $\bar{n}$ occupies the region $\bar{n} - 1 < \mu/U < \bar{n}$, that is, the region discussed above for the case without hopping. Hence the Mott phase is characterized by an incompressible nature, that is, the occupation $\langle \hat{n} \rangle$ is kept fixed within the lobe. The vertical width of the Mott lobe in the $(J/U, \mu/U)$ diagram constitutes the energy gap necessary to create particle-hole excitations in the Mott insulator.

The tip of the Mott lobes is given by the condition $\mu_+ = \mu_-$ for a given $\bar{n}$, which results in the critical U/J ratio for getting a Mott insulator with $\bar{n}$ particles per site:

$$\left(\frac{U}{zJ}\right)_c = 1 + 2\bar{n} + \sqrt{(1-2\bar{n})^2 + 1} \tag{1.12}$$

For $\bar{n} = 1$, one obtain the critical $\left(\frac{U}{zJ}\right)_{cr} \simeq 5.83$. Although the mean-field decoupling formalism discussed above provides a reasonably good approximation to the actual phase diagram, it significantly deviates from the actual values, especially in the case of one-dimensional systems ($z = 2$). Density-matrix renormalization group (DMRG) calculations provide a critical value $\left(\frac{U}{zJ}\right)_c \simeq 3.84$, much lower than the mean-field result.

In the cubic lattices and effectively unit filling, the existence of a quantum phase transition from a homogeneous condensate to a Mott-insulator with a nonzero gap has been proven rigorously in a model of hard-core bosons in the presence of a staggered field [25].

1.3.2. Wedding cake structure

Up to this point we did not consider any overall harmonic confinement. The latter is however the case in typical experiments. This external potential plays actually an important role, since it allows for spatial regions with integer filling (note once more that Mott insulators are characterized by a given integer filling). An overall harmonic confinement leads to an extra term

$$H_T = \frac{m}{2}\Omega^2 D^2 \sum_j j^2 \hat{n}_j^2, \tag{1.13}$$

with Ω the frequency of the harmonic oscillator, D the lattice spacing, and we consider that the site $j = 0$ is at the trap center (we consider here for simplicity a one-dimensional lattice, although the ideas can be easily extrapolated to higher dimensional lattices). We can then define the local chemical potential, $\mu_j = \mu_0 - \frac{m}{2}\Omega^2 D^2 j^2$, where μ_0 is the chemical potential at the trap center. Employing local-density approximation, we can easily find the spatial distribution of the different phases in the trap by looking in the $(J/U, \mu/U)$ diagram of Mott lobes the phase that correspond to the local chemical potential and the particular hopping considered. This provides a typical wedding cake structure of the different phases (see Fig. 1.2(b)).

1.3.3. Experimental realization

The Bose-Hubbard model was realized in breakthrough experiments at I. Bloch' lab in 2002 [13]. In those experiments they realized the Mott-insulator-to-superfluid transition with cold bosons in an optical lattice. This was performed combining two key observations. First, the trapping, including the trap was abruptly switched-off. The atoms fell in

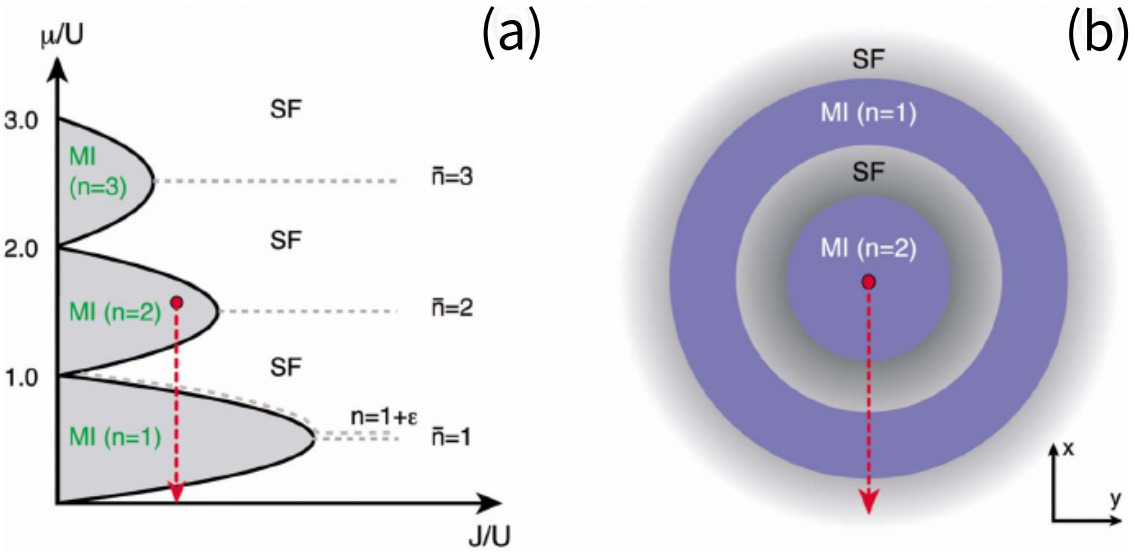

Figure 1.2: (a) Mean-field phase diagram of the Bose-Hubbard model at zero temperature with superfluid and Mott-insulator phases. Dashed lines, which indicate constant integer density $\langle \hat{n} \rangle = n = 1, 2, 3$, reach the tip of the Mott lobes. For $n = 1 \pm \varepsilon$ the line of constant density stays outside the $n = 1$ Mott-insulator since a fraction ε of the particles (or holes) remains superfluid down to the limit $J \to 0$. (b) In an external trap with an $n = 2$ Mott-insulator phase in the center, a series of Mott-insulator and superfluid regions appear when moving toward the edge of the cloud, following a wedding-cake structure. Figures from Ref. [1].

gravity into a detector. This so-called time-of-flight measurement provides to a good approximation a picture of the momentum distribution within the lattice. In the superfluid phase, where coherence is large, they observed the formation of well defined interference fringes. In contrast, for a sufficiently large lattice depth V_0, and hence a sufficiently small hopping J, they observed the blurring of the interference fringes, finally obtaining an incoherent Gaussian-like background, as one would expect from the Mott insulator phase (note that in that phase the atoms are strongly localized to a single site, and hence there is no coherence that would lead to interference fringes).

In a second experiment they probed directly the Mott gap. Within the Mott regime, they tilted the lattice, quickly went into the superfluid regime, and then expand in time-of-flight. If the tilting was steep enough (in other words, if the gap was overcome), excitations were created in the Mott insulator, which were later on translated after the quench into the superfluid regime into the broadening of the peaks of the interference pattern. Measuring the width of the peaks hence provided key information about the energy gap in the Mott phase.

Later experiments allowed for the direct observation of the wedding cake structure,

first indirectly [26, 27], and later directly by means of site resolved in-situ measurement using atomic quantum microscopes [28, 29].

1.4. Fermi-Hubbard model

1.4.1. Mott-metal transition

Using similar arguments it is possible to derive the Hamiltonian for spin-(or pseudo-spin)-1/2 Fermi systems, the so-called Fermi-Hubbard model

$$H = -J \sum_{<i,j>,s} \left(\hat{a}_{i,s}^{\dagger} \hat{a}_{j,s} + H.c. \right) + U \sum_{j} \hat{n}_{j,\uparrow} \hat{n}_{j,\downarrow}, \tag{1.14}$$

where $s = \uparrow, \downarrow$ denotes the two possible spin states, and of course now the operators fulfill Fermi anti-commutation rules. Note that in the Fermi-Hubbard model, in addition to the occupation of the site, we have the additional spin degree of freedom. For a single-component (polarized) Fermi gas, Pauli exclusion would forbid to place more than one particle per site. A band-insulator, and not a Mott-insulator, would hence result if unit filling is reached.

In contrast, for a two-component Fermi gas, we may have up to two particles of opposite spin per site. Those two particles interact via short-range interactions leading to an on-site interaction term, characterized by the coupling constant U. A band-insulator results if the filling factor two is reached. In addition, we may have as for the bosonic case a Mott insulator with one fermion per site if U/J is sufficiently large. Otherwise the system would be in an itinerant metallic state. Up to this point the physics is similar to that found in the Bose-Hubbard model. The Mott-metal transition was indeed observed in ultra cold Fermi gases in optical lattices by the group of T. Esslinger at ETH [30] and that of I. Bloch at Mainz [31].

1.4.2. Super-exchange and the Heisenberg model

As mentioned above, the site occupation is just one part of the problem, the other part is given by the spin degree of freedom. In particular, within the Mott insulator phase with one fermion per site, what is the ground-state spin configuration? In order to answer this question, we should introduce the idea of super-exchange, and the resulting spin model. This discussion nicely illustrates the potential of ultracold lattice gases for the simulation of spin models of great interest in quantum magnetism and high-temperature

superconductivity.

Let us consider $U \gg J$ and only two neighboring sites, $j = 1, 2$. The Fermi-Hubbard Hamiltonian acquires the form $H = H_0 + H_1$, with $H_0 = U \sum_{j=1,2} \hat{n}_{j\uparrow}\hat{n}_{j\downarrow}$, and $H_1 = -J \sum_{s=\uparrow,\downarrow}(\hat{a}^\dagger_{1s}\hat{a}_{2s} + \hat{a}^\dagger_{2s}\hat{a}_{1s})$. For $U \gg t$, we can consider H_0 as the zeroth order Hamiltonian and H_1 as a perturbation. Let us consider states with two atoms (of in principle whatever spin) in the two sites. Since doubly occupied sites will be very energetic, the ground-state manifold is four-fold: $\{|\uparrow,\uparrow\rangle, |\uparrow,\downarrow\rangle, |\downarrow,\uparrow\rangle, |\downarrow,\downarrow\rangle\}$. Using second-order perturbation theory, and properly taking into account Pauli exclusion and anticommutation rules, we obtain an effective Hamiltonian within the ground-state manifold of H_0:

$$H^{(2)} = \frac{-2J^2}{U}\left(|\uparrow,\downarrow\rangle\langle\uparrow,\downarrow| + |\downarrow,\uparrow\rangle\langle\downarrow,\uparrow| - |\uparrow,\downarrow\rangle\langle\downarrow,\uparrow| + |\downarrow,\uparrow\rangle\langle\uparrow,\downarrow|\right). \tag{1.15}$$

Using Pauli matrices, we may then introduce the spin operators $\hat{\sigma}^+_j = \frac{1}{2}(\hat{\sigma}^x_j + i\hat{\sigma}^y_j) = \hat{a}^\dagger_{j\uparrow}\hat{a}_{j\downarrow}$, $\hat{\sigma}^-_j = \frac{1}{2}(\hat{\sigma}^x_j - i\hat{\sigma}^y_j) = \hat{a}^\dagger_{j\downarrow}\hat{a}_{j\uparrow}$, and $\hat{\sigma}^z_j = \hat{n}_{j\uparrow} - \hat{n}_{j\downarrow}$. The Hamiltonian $H^{(2)}$ then transforms into the form $\frac{J^2}{U}\boldsymbol{\sigma}_1 \cdot \boldsymbol{\sigma}_2$. The effective spin-spin interaction at nearest neighbors that occurs, despite of the on-site character of the inter-particle interactions, due to second-order virtual excursions to the neighboring sites, receives the name of super-exchange. This effect was first experimentally observed by I. Bloch's group in 2007 [32]. It is easy generalized to a multi-site system, leading to the isotropic Heisenberg Hamiltonian:

$$H = \frac{J^2}{U}\sum_{<i,j>} \boldsymbol{\sigma}_i \cdot \boldsymbol{\sigma}_j. \tag{1.16}$$

A more general case occurs when the hopping of the different spin components $(J_\uparrow, J_\downarrow)$ and/or their interactions $(U_{\uparrow\uparrow}, U_{\uparrow\downarrow}, U_{\downarrow\downarrow})$ are different. This is suggested by utilizing Mott insulators of two-component bosons [33, 34], with which one obtains XXZ models of the form:

$$H = \sum_{<i,j>}\left[\pm J_\perp(\hat{\sigma}^x_i\hat{\sigma}^x_j + \hat{\sigma}^y_i\hat{\sigma}^y_j) + J_z\hat{\sigma}^z_i\hat{\sigma}^z_j\right], \tag{1.17}$$

with $+J_\perp$ for fermions and $-J_\perp$ for bosons, $J_\perp = J_\uparrow J_\downarrow / U_{\uparrow\downarrow}$, $J_z = (J^2_\uparrow + J^2_\downarrow)/2U_{\uparrow\downarrow}$ for fermions, and $J_z = (J^2_\uparrow + J^2_\downarrow)/2U_{\uparrow\downarrow} - J^2_\uparrow/U_{\uparrow\uparrow} - J^2_\downarrow/U_{\downarrow\downarrow}$ for bosons.

1.4.3. Fermi-Hubbard antiferromagnet

Note that the prefactor of Eq. (1.16) is positive, and hence the effective spin coupling is antiferromagnetic, that is, the spins minimize their spin interaction energy by being antiparallel to each other. Long-range antiferromagnetism was first observed in M. Greiner's

group at Harvard in 2017 [35].

Since then, the study of the 2D Fermi-Hubbard model has constituted one of the major research focuses in the physics of cold gases. Particularly interesting is the relation with high-temperature superconductivity. In particular, when moving away from half-filling, that is, from one atom per site, holes may pair in d-wave, leading to the so-called d-wave superconductivity, which is expected to play a crucial role in high-temperature superconductivity in cuprates.

1.5. extended Hubbard model

1.5.1. Polar lattice gases

Contact-interacting particles realize lattice models with merely on-site interactions, although for the super-exchange discussed above, effective small nearest-neighbor terms may appear at second order in perturbation theory. Much richer models can be realized by systems that present longer-range power-law-decaying interactions. The latter include experiments on trapped ions where power-law interactions $1/r^{s=0,\dots,3}$ may be engineered [36, 37]. It is also the case of Rydberg atoms [38, 39], which may present strong van der Waals interactions to nearest neighbors and dipole-dipole interactions.

Particularly relevant are as well experiments on polar lattice gases, which will play a key role in this Thesis. These experiments are performed using either magnetic atoms, with a large magnetic moment $\mathbf{d}_m$, or polar molecules, with an electric dipole moment $\mathbf{d}_e$. In general, the dipolar coupling is much higher in the electric case, the typical magnitude of $\mathbf{d}_e$ for an atomic or molecular system is $|\mathbf{d}_e| = q_e a_0$, where $a_0 = 4\pi\varepsilon_0\hbar^2/q_e^2 m_e$ is the Bohr radius, while the magnetic dipole is a multiple of the Bohr magneton $\mu_\mathrm{B} = q_e\hbar/2m_e$. The ratio of $\mathbf{d}_e/\mathbf{d}_m$ scales as $1/\alpha$, where $\alpha \simeq 1/137$ is the fine structure constant. Electric dipole moments can be created either by an external electric field, or by dressing resonantly different rotational states. Magnetic dipole moments are small in alkali atoms, but they may be particularly large in atoms like chromium, erbium, dysprosium and europium, which present dipole moments of several Bohr magnetons. For more details on dipolar atoms and molecules we refer to Ref. [40] and references therein.

Spin-exchange interactions have been observed in lattice gases of chromium atoms [41] and of KRb polar molecules [42]. Although inelastic losses [43, 44] make it challenging to realize extended Hubbard models with strong dipole-dipole interactions with polar molecules, the problem may be overcome by using fermionic molecules [45] and employing

recently developed shielding methods [46]. Furthermore, recent experiments using erbium atoms have already realized an extended Hubbard model with nearest-neighbor interactions [47]. Although in those experiments the nearest-neighbor interactions (compared to the hopping rate) were relatively modest, inter-site dipolar interactions may be significantly enhanced in lanthanide gases when confined in UV lattices. Polar quantum lattice gases constitute therefore a promising candidate for studying the dynamics of extended models with strong inter-site $1/r^3$ interactions. In the following, we will focus on dipolar gases, discussing some relevant issues associated to the dipole-dipole interaction.

1.5.2. Dipole-dipole interaction

Let us consider two particles with dipole moments, $\mathbf{d}_{1,2}$ at a relative distance $\mathbf{r} = \mathbf{r}_2 - \mathbf{r}_1$ (Fig. 1.3 (a)). The interaction energy is governed by the dipole-dipole interaction (DDI)

$$V_{\mathrm{dd}} = \frac{C}{4\pi r^3}\left[\mathbf{d}_1 \cdot \mathbf{d}_2 - 3(\mathbf{d}_1 \cdot \hat{\mathbf{r}})(\mathbf{d}_2 \cdot \hat{\mathbf{r}})\right]. \tag{1.18}$$

The constant C is the inverse permittivity of vacuum $1/\varepsilon_0$ for, $\mathbf{d}$, being an electric dipole moment, and the permeability of vacuum, μ_0, for $\mathbf{d}$ being a magnetic dipole moment, and $\hat{\mathbf{r}}$ is a unit vector parallel to the line joining the centers of the two magnetic moments. Assuming a polarized sample (Fig. 1.3 (b)-(d)), where all dipole moments point in the same direction, the interaction becomes of the form:

$$V_{\mathrm{dd}} = \frac{C}{4\pi r^3}|\mathbf{d}|^2(1 - 3\cos^2\theta). \tag{1.19}$$

As θ varies between 0 and $\pi/2$, the factor $1 - 3\cos^2\theta$ varies between -2 to 1. Thus the interaction is repulsive for dipoles placed side-by-side, whereas it is attractive, and twice stronger than the side-by-side case, for dipoles in a head-to-tail configuration. At the special value, the so-called "magic angle", $\theta_m = \arccos(1/\sqrt{3})$ the dipole-dipole interaction vanishes.

From general results of scattering theory, a central potential falling off at large distances as $1/r^n$ has scattering phase shifts at low momentum limit, $\delta(k) \sim k^{n-2}$, for the partial wave components with angular momenta $l \leq (n-3)/2$, and $\delta_l(k) \sim k^{2l+1}$ for $l < (n-3)/2$. In the case of the dipolar interaction, $\delta_l \sim k$, and all partial wave components contribute to the scattering amplitude. Moreover, due to the anisotropy of the dipolar interaction, partial waves with different angular momenta couple with each other. This property has an interesting consequence in the case of a polarized Fermi gas, where short-range interactions

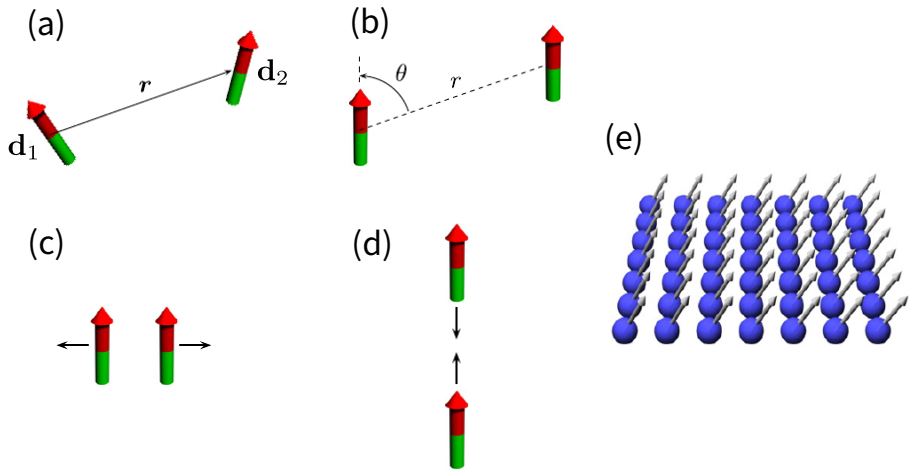

Figure 1.3: Two particles interacting via the dipole-dipole interaction. (a) Non-polarized case; (b) polarized case; (c) two polarized dipoles side by side repel each other;(d) two polarized dipoles in a head-to-tail configuration attract each other; (e) a gas of polarized dipoles in a 2D optical lattice. Figure from Ref. [40].

freeze out at low temperatures when entering the degeneracy regime. In contrast, dipolar interactions remain relevant all the way down to zero temperature. This may be used to perform evaporative cooling of polarized fermions, without the need of sympathetic cooling via a bosonic species [48]. Finally, we note as well that due to its anisotropy, the dipole-dipole interaction can induce spin flips, leading to dipolar relaxation. The cross section for dipolar relaxation scales with the cube of the dipole moment [49], and therefore is crucial in spin systems with strong dipolar interactions.

1.5.3. Extended Bose-Hubbard model

For a lattice gas of polarized dipoles, inter-site interactions become particularly important, and the system is well described by the extended Hubbard model:

$$H = -J \sum_{<i,j>} \left(\hat{a}_i^\dagger \hat{a}_j + H.c.\right) + \frac{U}{2} \sum_j \hat{n}_j(\hat{n}_j - 1) + \frac{1}{2} \sum_l \sum_{i,j \neq i} U_{ij} n_i n_j, \tag{1.20}$$

where $U_{ij} = \frac{C|\mathbf{d}|^2}{4\pi|\mathbf{r}_i - \mathbf{r}_j|^3}(1 - 3\cos^2\theta_{ij})$, with θ_{ij} the angle between $\mathbf{r}_i - \mathbf{r}_j$ and the dipole moment. As discussed in this Thesis, the ratio between the nearest-neighbor dipolar interaction and the hopping rate (and for soft-core systems that between the on-site interactions and the nearest-neighbor interactions) plays a key role in the dynamics of the system. The derivation of the extended Hubbard model is performed in a similar way as

for the Hubbard model with only short-range interactions. We should mention however, that the dipole-dipole interaction may lead to additional terms, not included in the extended Hubbard model above, and which may play a relevant role if the optical lattice is not sufficiently deep. This is the case, in particular, of collisionally-assisted hopping, e.g. terms of the form $\hat{a}_j\hat{n}_{j+1}\hat{a}_{j+2}$ [50], which may play a relevant role for large dipole moments in shallow lattices. We will not consider these terms in this Thesis, assuming that the lattice is deep enough.

1.5.4. Ground-state phases of polar lattice gases

Whereas, as discussed above, the standard Bose-Hubbard model presents only a superfluid phase and Mott-insulator phases in the ground-state, the extended Hubbard model displays a much richer landscape of ground-state phases due to the interplay between inter-site and on-site interactions, hopping, and (for dimensions larger than one) interaction anisotropy. Here we just illustrate the richness of the possible phases with two particularly relevant examples.

If the dipole is perpendicular to the lattice plane, the inter-site dipolar interaction is repulsive, eventually favoring crystalline configurations in which they avoid being at neighboring sites. A more intriguing phase may occur if the system remains superfluid while presenting a crystalline modulation, the so-called lattice supersolid phase. In this sense, it has been shown by means of Quantum Monte Carlo calculations [51] that a supersolid may be stabilized against phase separation in an extended Bose-Hubbard model with just nearest neighbour interactions, as long as the filling of the lattice is larger than $1/2$ and $V > U/z$, where z is the coordination number we have already introduced in our discussion of the Mott insulator phase.

Other interesting phase that may occur in (one-dimensional) extended Bose-Hubbard models is the so-called Haldane insulator phase [52]. Let us consider the case of a filling factor $\bar{n} = 1$ per site. Let us assume that in addition to singly-occupied sites we may have empty and doubly-occupied sites. The system may then be mapped to a spin-1 lattice model with extended interactions, realizing a so-called Haldane spin-1 chain. It is known that such system may present a rather intriguing phase characterized by string correlations, which for the case of the extended Hubbard model imply that a site with zero (two) particles is followed by arbitrary number of singly-occupied sites, then by a site with two (zero) particles, and so on.

Other interesting possibilities include, e.g., the possibility of having interlayer super-

fluidity [53], pair superfluidity [54] and supersolidity [55], and interlayer filaments [56, 57]. For a more throughout discussion on the rich ground-state physics of dipolar lattice gases we refer to the reviews [40] and [58]. Finally, we would like to note that none of these intriguing ground-state phases have been as yet experimentally realized, and that experiments on polar lattice gases can be considered at this moment in its very infancy. In this Thesis, we will analyze in detail the particle dynamics in polar lattice gases. As we will show, this dynamics may be largely handicapped for sufficiently large V/J, which may eventually constitute a problem to take into consideration when creating ground-state phases.

1.6. Quantum gases out of equilibrium

Since experiments on ultra cold gases may be performed under conditions of nearly perfect isolation, cold gases constitute an excellent tool for the study and understanding of the dynamics of isolated quantum many-body systems, and in particular under which conditions these systems when brought out of equilibrium thermalize or not. In this brief section we mention, without any purpose of being exhaustive, some of the key experiments on the dynamics of many-body quantum systems, which illustrate very well the possibilities open by cold gases experiments.

As discuss in the next chapter, thermalization may be prevented due to integrability. This is in particular the case of one-dimensional or quasi-one-dimensional systems. An especially interesting experiment in this sense was performed at D. Weiss' lab at Penn State University [59]. In that experiment, they studied the relaxation dynamics of a one-dimensional Bose gas, showing that as long as the system remained one-dimensional no relaxation towards a thermal state was observed. Such a lack of thermalization results from the (nearly) integrable character of the one-dimensional contact-interacting gas [60]. Later experiments on matter-wave interference of coherently split one-dimensional Bose gases at J. Schmiedmayer's group in Vienna revealed the occurrence of prethermalization [61], since after an initial rapid decoherence, the system reached a quasi-steady state, which can be described by effective temperature several times lower than the thermal temperature.

Cold gases in optical lattices offer as well interesting possibilities for the exploration of the dynamics of isolated quantum many-body systems. Quench experiments may be employed to study the relaxation dynamics towards equilibrium, as in experiments at I. Bloch's group in 2012 [62], in which starting with a patterned density with alternating

empty and occupied sites in isolated Hubbard chains, they suddenly switched on the tunnel coupling along the chains, observing a fast relaxation of the measured observables to steady-state values. Later experiments in the same group [63] studied the propagation of correlations via quasiparticle pairs across a quenched one-dimensional quantum gas in an optical lattice, resulting in an effective light cone for the quantum dynamics. These results demonstrated the existence of a Lieb-Robinson bound, which is an effective "speed of light" that limits the propagation of correlations.

Interestingly, interactions may affect the transport of particles in an optical lattice even for modest ratios between on-site interactions and inter-site hopping. This was clearly revealed at I. Bloch's group in experiments in which an initially confined Fermi gas was allowed to expand freely in an optical lattice. They showed that even weak interactions may lead to a severe slow down of particle transport [64], directly linked to the formation or preformation of repulsively-bound pairs [65] (see Sec. 2.5).

Experiments in optical lattices have revealed also interesting non-equilibrium dynamics in what concerns spin models. As an example, experiments at I. Bloch's group have directly observed using in-situ correlation measurement the formation of two-magnon bound states in a one-dimensional Heisenberg spin chain formed by ultra-cold bosons in an optical lattice [18]. Later experiments in the same group studied the decay of an imprinted spin spiral, finding diffusive spin transport in one-dimensional systems, and superdiffusive behavior in two dimensions [19]. Recent experiment at W. Ketterle's group at MIT have studied spin transport in an XXZ model, after quantum quenches from imprinted spin-helix patterns, showing ballistic behavior for XX models, and diffusive behavior in the Heisenberg limit [20].

Cold atoms also offer remarkable possibilities for the study of dynamics in disordered many-body systems. Disorder may be induced in an optical lattice by means of a speckle potential [66], whereas quasi-disorder may be created by means of an additional incommesurate lattice [67]. Seminal experiments have recently explored the dynamics of particles in the presence of disorder, in particular many-body localization [68, 69].

We should finally mention that many of the above-mentioned experiments would not have been possible without the development of quantum gas microscopes [70, 71], a detection technique that combines fluorescence imaging and laser cooling. This technique has made possible in-situ site-resolved single-atom detection, overcoming the limitations previously posed by time-of-flight techniques. Moreover, quantum gas microscopes not only revolutionized the detection, but also the control, manipulation, and preparation of

lattice gases.

Chapter 2

Localization and ergodicity in quantum systems

Recent years have witnessed a major interest on the dynamics of isolated many-body quantum systems [72, 73, 74]. As briefly discussed in Sec.1.6, this interest has been largely triggered by impressive experimental developments, especially in cold gases [1] and trapped ions [36], which realize almost perfect isolation [37, 75, 76]. A fundamental question concerning the dynamics of many-body quantum systems concerns the thermalization of out-of-equilibrium systems, or their lack of it. In general, many-body systems are believed to thermalize as a consequence of the eigenstate thermalization hypothesis [77, 78, 79, 80]. Two prominent exceptions to this paradigm are provided by integrable systems [81, 82, 83, 84] and disordered systems, in which many-body localization may occur [85, 86, 87, 88]. Progress on many-body localization has been recently followed by interest on localization in absence of disorder [89, 90, 91, 92, 93, 94, 95, 96, 97, 98, 99, 100, 101, 102, 103, 104, 105, 106, 107, 108].

In this Chapter, we review key ideas such as the eigenstate thermalization hypothesis, integrability, and localization in the presence and absence of quenched disorder. The latter discussion will particularly relevant for this Thesis, since as discussed in the following chapters, polar lattice gases offer an interesting scenario for disorder-free interaction-induced localization.

2.1. Eigenstate thermalization hypothesis

How statistical mechanics emerges from the unitary evolution of quantum systems is a fundamentally relevant problem [109]. In this section we introduce the concept of

eigenstate thermalization hypothesis that provides for rather general quantum systems the necessary bridge between quantum evolution and statistical mechanics.

Let us suppose that an isolated system is prepared in a non-stationary state with a well-defined mean energy, and subextensive energy fluctuations. An observable $\hat{O}$ is said to thermalize if (i) after some relaxation time, the average expectation value of this observable agrees with the microcanonical expectation value, and (ii) temporal fluctuations of the expectation value about the microcanonical prediction are small at most later times. This implies that the long-time average accurately describes the expectation value of $\hat{O}$ at almost all times and agrees with the microcanonical prediction.

In real systems thermal expectation values of observables depend on the energy density (temperature), and relaxation times are observable dependent. In a series of groundbreaking works in the 1990s [78, 110, 111], Srednicki introduced the concept of eigenstate thermalization hypothesis (ETH). In the basis of the eigenstates of a Hamiltonian, ETH can be formulated as an ansatz for the matrix elements of observables [111],

$$O_{mn} = O(\bar{E})\delta_{mn} + e^{-S(\bar{E})/2} f_O(\bar{E}, \Delta) R_{mn}, \tag{2.1}$$

where $\bar{E} = (E_m + E_n)/2$, $\Delta = E_n - E_m$, and $S(\bar{E})$ is the thermodynamic entropy at energy $\bar{E}$. Importantly, $O(\bar{E})$ and $f_O(\bar{E}, \Delta)$ are smooth functions of their arguments, the value of $O(\bar{E})$ is identical to the expectation value of the microcanonical ensemble at energy $\bar{E}$, and $f_O(\bar{E}, \Delta)$ determines the linear response following a perturbation about equilibrium and the fluctuation-dissipation relation of the ensemble [112]. R_{mn} is a random variable with zero mean and unit variance, if the system obeys time-reversal symmetry, the Hamiltonian can be chosen to be real and so will be the matrix of observables, then $R_{nm} = R_{mn}$ and $f_O(\bar{E}, -\Delta) = f_O(\bar{E}, \Delta)$, otherwise $R_{nm} = R^*_{mn}$ and $f_O(\bar{E}, -\Delta) = f^*_O(\bar{E}, \Delta)$.

It is generally expected that Eq. (2.1) holds for all physical observables for which statistical mechanics applies. For a given Hamiltonian $H|n\rangle = E_n|n\rangle$ and a time evolved state $|\psi(t)\rangle = \sum_n e^{\frac{-i}{\hbar}E_n t} C_n |n\rangle$, the long-time average of $\hat{O}$ is

$$\bar{O} = \lim_{T\to\infty} \frac{1}{T} \int_0^T \langle\psi(t)|\hat{O}|\psi(t)\rangle \, \mathrm{d}t = \sum_m |C_m|^2 O(E_m) = \mathrm{Tr}[\hat{\rho}_{\mathrm{DE}}\hat{O}], \tag{2.2}$$

where $O(E_m)$ constructs the first term of Eq. (2.1), and $\hat{\rho}_{\mathrm{DE}} = |\psi_I\rangle\langle\psi_I|$ is the density matrix of the diagonal ensemble. On the other hand, statistical mechanics predicts

$$O_{\mathrm{ME}} = \mathrm{Tr}[\hat{\rho}_{\mathrm{ME}}\hat{O}], \tag{2.3}$$

where $\hat{\rho}_{\rm ME}$ is the density matrix of the microcanonical ensemble. For a well-defined mean energy, $\mathrm{Tr}[\hat{\rho}_{\rm ME}H] = \mathrm{Tr}[\hat{\rho}_{\rm DE}H] = \langle E\rangle$, and if the energy fluctuations $\delta E^2_{\rm DE} = \mathrm{Tr}[\hat{\rho}_{\rm DE}H^2] - \langle E\rangle^2$ and $\delta E^2_{\rm ME} = \mathrm{Tr}[\hat{\rho}_{\rm ME}H^2] - \langle E\rangle^2$ are sufficiently small, the smooth function $O(E_m)$ can be represented by the Taylor expansion

$$O(E_m) = O(\langle E\rangle) + (E_m - \langle E\rangle)O'(\langle E\rangle) + \frac{1}{2}(E_m - \langle E\rangle)^2 O''(\langle E\rangle) + \cdots . \tag{2.4}$$

Substituting the series into Eq. (2.2) and Eq. (2.3) one obtains

$$\bar{O} \sim O_{ME} + \frac{1}{2}(\delta E^2_{\rm DE} - \delta E^2_{\rm ME})O''(\langle E\rangle). \tag{2.5}$$

If the energy fluctuations in the time-evolving system are subextensive, which is generically the case in systems described by a local Hamiltonian, then the second term is a small subextensive correction to $O_{\rm ME}$, which is negligible for large systems. It is remarkable that, using ETH, one can show that $\bar{O} \sim O_{\rm ME}$ without the need of making any assumption about the components of the wavefunction C_m. The fluctuations of $\hat{O}$ can be evaluated in a similar a way, for a long-time evolution,

$$\overline{\delta O^2} = \lim_{T\to\infty}\frac{1}{T}\int_0^T \langle\psi(t)|(\hat{O}-\bar{O})^2|\psi(t)\rangle\,\mathrm{d}t = \sum_m |C_m|^2 O^2(E_m) - \bar{O}^2 = \mathrm{Tr}\left[\hat{\rho}_{\rm DE}\hat{O}^2\right] - \bar{O}^2, \tag{2.6}$$

and for the microcanonical ensemble, $\delta O^2_{\rm ME} = \mathrm{Tr}\left[\hat{\rho}_{\rm ME}\hat{O}^2\right] - O^2_{\rm ME}$. Introducing the Taylor series of $O(E_m)$, one finds

$$\overline{\delta O^2} \sim \delta O^2_{\rm ME} + \frac{1}{2}(\delta E^2_{\rm DE} - \delta E^2_{\rm ME})\; O^{2\prime\prime}(\langle E\rangle), \tag{2.7}$$

i.e., the long-time average fluctuations of $\hat{O}$ thus scale as the equilibrium statistical fluctuations, $\delta O_{\rm ME}$.

A straightforward generalization to mixed states can be done by the substitutions, $C^*_m C_n \mapsto \rho_{mn}$ and $|C_m|^2 \mapsto \rho_{mm}$, where ρ_{mn} are the matrix elements of the initial density matrix in the basis of the eigenstates of the Hamiltonian. Moreover, due to ensemble equivalence one can use a canonical, or other equilibrium density matrix instead of the microcanonical ensemble.

2.2. Integrable systems

A major exception to the ETH paradigm is provided by integrable systems, in which the presence of extensive number of integrals of motion breaks ergodicity.

In classical mechanics, integrability demands that the N-particle Hamiltonian, $H = H(\cdots x_j \cdots ; \cdots k_j \cdots ; t)$, can be transformed to canonical variables Q_j, P_j, in which all of the P_j's are mutually independent integrals of motion (constants of motion), and all Q_j's are cyclic. That is, there exists a canonical transformation $H \mapsto \tilde{H}(\cdots Q_j \cdots ; \cdots P_j \cdots ; t) = \tilde{H}(\cdots P_j \cdots ; t)$ [113], such that the equations of motion are simply solved as

$$\frac{\partial P_j}{\partial t} = -\frac{\partial \tilde{H}}{\partial Q_j} = 0 \Rightarrow P_j(t) = P_j(0), \tag{2.8}$$

$$\frac{\partial Q_j}{\partial t} = \frac{\partial \tilde{H}}{\partial P_j} = \omega_j(\cdots P_j \cdots) \Rightarrow Q_j(t) = \omega_j t + Q_j(0). \tag{2.9}$$

As a result, the time evolution of a many-body state of an integrable system performs a toroidal trajectory in phase space.

The direct translation of the concept of integrability in quantum systems is problematic. If the N independent integrals of motion P_j are directly taken by N mutually commuting operators, once these operators share the same eigenstates with the Hamiltonian, then they can be represented by means of each other [81], and therefore the meaning of "independent" is unclear. Moreover, integrals of motion alone can be trivial, since every Hamiltonian has infinite conserved quantities given by its eigenstate projectors, but this does not imply anything.

A different approach to translate the classical idea of integrability into quantum mechanic is to restrict only to systems which support scattering without diffraction [81]. Diffraction-free scattering rarely happens with generic interactions that possess a decaying tail, with the special exception of the inverse-square potential $V(r) \propto 1/r^2$, and its transformations. Most of the integrable systems consist of particles with short-rang interactions, such as contact interactions (characterized by a δ pseudo-potential) or nearest-neighbor interactions. A well-known representative example of integrable system is the XXZ model, Eq. (1.17), whose integrability will be discussed below. It has also been pointed out that the locality properties of the integrals of motion play a determinant role in quantum integrable models [114, 115]. The quantities should be describable by either local operators or summations of finite local operators [115], such that trivial non-local integrals of motion, in particular the projectors of eigenstates or arbitrary powers of the

Hamiltonian, are irrelevant.

Integrable systems do not exhibit thermalization. From the classical point of view, the time evolution of an integrable system is constrained by integrals of motion, and the time average and the microcanonical ensemble average do not need to agree. Nevertheless, a many-body state might still uniformly fill the available phase space. In other words, the long-time average could still be described by some ensemble average, but it needs to be a generalized microcanonical ensemble that accounts for all conserved quantities in the system [116]. In the language of quantum mechanics, the failure of integrable quantum systems to exhibit eigenstate thermalization can be traced back to the fact that they have an extensive number of nontrivial (local/extensive) conserved quantities $\hat{I}_k$. However, the presence of generic dephasing may allow observables in integrable systems to relax to stationary values and remain close to those values at most later times. The equilibrium of such a system may be given by the so-called generalized Gibbs ensemble (GGE) [117], whose density matrix

$$\hat{\rho}_{\mathrm{GGE}} = \frac{\exp(-\sum_k \lambda_k \hat{I}_k)}{\mathrm{Tr}\left[\exp(-\sum_k \lambda_k \hat{I}_k)\right]}, \tag{2.10}$$

is obtained by maximizing the entropy under the time-evolution constraints imposed by integrals of motion. For each k, the Lagrange multipliers, λ_k, are determined by requiring that $\mathrm{Tr}[\hat{\rho}_{\mathrm{GGE}}\hat{I}_k]$ equals the expectation value of $\hat{I}_k$ in the initial state. So far, by studying few-body observables after relaxation, GGE has been verified in a large number of studies of integrable models (see e.g. Ref. [112] and references therein).

2.2.1. XXZ model

One of the most important and well-studied integrable models is the one-dimensional XXZ model, Eq. (1.17). It may be realized using cold bosons in an optical lattices in the hard-core regime, in which the on-site interactions are strong enough to prevent double occupancies, and hence the on-site occupation is limited to 0 or 1. The mapping between the XXZ model and the hard-core bosons is given by the Holstein-Primakoff transformation:

$$\begin{cases} \hat{\sigma}_j^x = \hat{a}_j^\dagger + \hat{a}_j \\ \hat{\sigma}_j^y = -i(\hat{a}_j^\dagger - \hat{a}_j) \\ \hat{\sigma}_j^z = (2\hat{n}_j - 1)\ . \end{cases} \tag{2.11}$$

In the hard-core boson formulation the Hamiltonian of the model becomes of the form:

$$H_{\mathrm{XXZ}} = \sum_j -J(\hat{a}^\dagger_{j+1}\hat{a}_j + \hat{a}^\dagger_j\hat{a}_{j+1}) + V\hat{n}_{j+1}\hat{n}_j, \tag{2.12}$$

which is the clean nearest neighbor model that we consider in Chapter 4. The nearest-neighbor interactions and the nearest-neighbor hopping guarantee diffraction-free scattering [82]. The scattering matrix satisfies the Yang-Baxter equation [83], and an analytical form of the integrals of motion is available [84] by means of Bethe ansatz [82, 118].

2.2.2. Bethe Ansatz

The basic idea of the Bethe Ansatz is that the system present diffraction-free scattering, such that one can use momenta $k_1, k_2 \cdots$ to label the many-body state $\Psi(x_1, x_2 \cdots)$. For a 1D system, the N-particle wave function can be represented as

$$\begin{aligned}\Psi(x) \to \sum_{\mathrm{Pr}} A(\mathrm{Pr}) \exp\left[i\sum_{j=1}^{N} x_j\, k_{n_j}\right] \\ + \underbrace{\int_{k'_1} \cdots \int_{k'_N}}_{\substack{K,E \text{ fixed} \\ k'_1<\cdots<k'_N}} S\left[k'_1 \cdots k'_N\right] \exp\left[i\sum_{j=1}^{N} x_j k'_j\right] dk'_1 \cdots dk'_N,\end{aligned} \tag{2.13}$$

where "Pr" denotes all the $N!$ permutations of $(n_1, n_2 \cdots)$ with $n_j \in [1, N]$, and $A(\mathrm{Pr})$ is the amplitude for each permutation. The first term of the equation is given by the permutations of the N incoming momenta k_j. It describes all possible two-body scattering processes. The last term describes diffraction, representing many-body interactions, and serving as the many-body scattering that will be needed to thermalize the momenta. The label "K, E fixed" denotes the conservation of the total momentum and energy for outgoing momenta k'_j.

For very few cases, e.g., the inverse-square interaction $V(r) \propto /r^2$ mentioned above, the diffraction term vanishes, the systems become exactly solvable, and the many-body scattering reduces into series of two-body process [81]. Consequently, for an integrable system the Bethe ansatz takes the form

$$\Psi(x) = \sum_{\mathrm{Pr}} A(\mathrm{Pr}) \exp\left[i\sum_{j=1}^{N} x_j\, k_{n_j}\right]. \tag{2.14}$$

To determine $A(\mathrm{Pr})$, notice that the $N!$ terms in sum can be grouped into pairs of Pr and

$\overline{\mathrm{Pr}}$, so that Pr is identical to $\overline{\mathrm{Pr}}$ except $\mathrm{Pr}_j = \overline{\mathrm{Pr}}_{j+1}$, $\mathrm{Pr}_{j+1} = \overline{\mathrm{Pr}}_j$ and $k_{n_j} = k_{\bar{n}_{j+1}} \equiv k$, $k_{\bar{n}_j} = k_{n_{j+1}} \equiv \bar{k}$. Equation (2.14) then becomes

$$\Psi(x) = \sum_{\text{pair}} \left[A(\mathrm{Pr}) e^{i(x_j k + x_{j+1}\bar{k})} + A(\overline{\mathrm{Pr}}) e^{i(x_j \bar{k} + x_{j+1} k)} \right] \exp\left[i \sum_{l \neq j, j+1} x_l \, k_{n_l} \right]. \tag{2.15}$$

The term $A(\mathrm{Pr}) e^{i(x_j k + x_{j+1}\bar{k})} + A(\overline{\mathrm{Pr}}) e^{i(x_j \bar{k} + x_{j+1} k)} = \psi(x_j, x_{j+1})$ is a two-body scattering wave function. For a 1D system with conserved total momentum and energy, $A(\mathrm{Pr})$ and $A(\overline{\mathrm{Pr}})$ can differ in a phase, θ. Galilean invariance implies that θ depends only on the relative momentum, i.e., $\theta = \theta(k - \bar{k})$. Reversing the scattering, one sees that the phase shift must be an odd function, so $\theta(\bar{k} - k) = -\theta(k - \bar{k})$. Therefore, one has the relative amplitude

$$A(\mathrm{Pr}) / A(\overline{\mathrm{Pr}}) = -e^{i\theta(\bar{k} - k)}, \tag{2.16}$$

and a general two-body wavefunction

$$\psi(x_1, x_2) = e^{i(x_1 k_1 + x_2 k_2)} - e^{i\theta(k_2 - k_1)} e^{i(x_1 k_2 + x_2 k_1)}. \tag{2.17}$$

The negative sign is added for the hard-core requirement, so if there is no scattering, $\theta = 0$ and $A(\overline{\mathrm{Pr}}) = -A(\mathrm{Pr})$, the wavefunction $\psi(x_j, x_{j+1})$ vanishes for $x_j \to x_{j+1}$.

Substituting the Bethe ansatz, Eq. (2.14), into the XXZ Hamiltonian, Eq. (2.12), for $x_{j+1} > x_j + 1$, gives

$$\begin{aligned} E\Psi &= \sum_{j=1}^{N} \left[\Psi(\cdots x_j + 1 \cdots) + \Psi(\cdots x_j - 1 \cdots) \right] \\ \Rightarrow E &= -2J \sum_{j=1}^{N} \cos(k_j) \equiv \sum_{j=1}^{N} \omega(k_j). \end{aligned} \tag{2.18}$$

Considering that the particles cannot hop into the same site, due to the hard-core constraint, in order to extend the above function to the full range including $x_{j+1} \geq x_j$, one should impose the condition

$$\sum_{NN} \left[\Psi(\cdots x, x \cdots) + \Psi(\cdots x + 1, x + 1 \cdots) \right] = V \sum_{NN} \Psi(\cdots x, x + 1 \cdots), \tag{2.19}$$

where the summation is taken over all pairs of nearest-neighbor particles. Since, as shown by Eq. (2.15), a many-body function $\Psi(\cdots x, x' \cdots)$ can be grouped into pairs, so that

each pair has the two-body state $\psi(x, x')$ as a factor, then the above condition reduces to

$$\psi(\cdots x, x \cdots) + \psi(\cdots x+1, x+1 \cdots) = V\psi(\cdots x, x+1 \cdots). \tag{2.20}$$

Putting it into Eq. (2.17) gives the phase shift

$$e^{i\theta(k'-k)} = \frac{1 + e^{i(k+k')+(V/J)e^{ik'}}}{1 + e^{i(k+k')+(V/J)e^{ik}}}. \tag{2.21}$$

And by imposing periodic boundary conditions, one has

$$e^{ikL} \prod_{k' \neq k} \mp e^{i\theta(k'-k)} = 1, \tag{2.22}$$

where the upper(lower) sign is for bosons(fermions). Taking the logarithm of this equation, one determines the k's by employing the equation $kL = 2\pi I_k + \sum_{k' \neq k} \theta(k'-k)$, where I_k are integers for fermions or odd number of bosons, and half integers for even number of bosons.

2.2.3. Long-range hops or long-range interactions

With the knowledge of the Bethe ansatz solution of the XXZ model, it is easy to see that a long-range hopping or interaction generally violates integrability. For example, if the system has hopping that is next-to-nearest neighbor, the dispersion relation, Eq. (2.18), will be quadratic in $\cos(k)$. Thus the conservation of momentum and energy of any two-body process allows four solutions. Two of them are permutations of the incoming momenta, but the other two are diffraction channels. And if long-range interactions exist, the many-body ansatz will not be two-body reducible, the terms in Eq. (2.19) become $\Psi(\cdots x, x \cdots) + \Psi(\cdots x+1, x+1 \cdots) = V\Psi(\cdots, x-r, \cdots, x, \cdots, x+r, \cdots)$, and the scattering phase shift of Eq. (2.21) fails. Such systems are believed to thermalize, in fact, previous researches have already shown the ergodicity for quantum lattice geses with next-to-nearest neighbor hopping/interaction [119, 120], and for dipolar lattice gases [121].

2.3. Quantum ergodicity

The idea of ergodicity is also problematic in quantum mechanics. In classical mechanics, ergodicity implies that the motion of a many-body state has no constant of motion, except the conservation laws due to the overall symmetries, such as the total

energy for time-translation invariance, $\partial H/\partial t = 0$, the center-of-mass momentum for space-translation invariance, $\partial H/\partial R_{CM} = 0$, etc. Trajectories in ergodic systems cover all the available phase space region. This concept essentially leads to the equal a priori probability assumption, crucial for the idea of ensemble average [122], which captures the long-time average of observables in statistical mechanics. But in a quantum system, there is no idea of trajectory according to the uncertainty principle. In fact, to describe a quantum state $|\psi\rangle$ evolving into another state $|\phi\rangle$, one calculates the overlapping between them $\langle\phi|\psi\rangle$. And since the Schrödinger equation is a linear differential equation, $|\psi\rangle_t = e^{\frac{-i}{\hbar}Ht}|\psi\rangle$, if the two states are evolved with the same Hamiltonian, the overlapping will be a constant in time. So if initially $\langle\phi|\psi\rangle = 0$, then $|\psi\rangle$ will never "visit" $|\phi\rangle$, and the ergodic hypothesis fails.

2.3.1. Random matrix theory and level statistics

A promising solution to this difficulty, is provided by the idea of quantum chaos and the related random matrix theory [123, 124, 125]. This theory studies the statistical properties of a complex quantum system, whose Hamiltonian can be described by a random hermitian matrix. Energy levels in random matrix theory obey Wigner-Dyson statistics. For a system with time-reversal symmetry, where the Hamiltonian is real and symmetric, the matrix elements are drawn from the so-called Gaussian orthogonal ensemble (GOE). The probability distribution for the corresponding level separations may be captured by the Wigner surmise

$$P(\delta) = \frac{\pi}{2}\delta e^{\frac{-\pi}{4}\delta^2}, \tag{2.23}$$

where δ is the separation between two adjacent energies, and the average δ is set to one. The GOE distributions exhibit two generic properties, (i) level repulsion, as the probability $P(\delta)$ vanishes when $\delta \to 0$, and (ii) a Gaussian decay at large energy separation. A simplified derivation of Eq. (2.23) can be found in Ref. [112]. Note that though here, in order to exemplify, we consider time-reversal symmetry, it is not essential for GOE spectra [126, 127].

The universality of random matrix theory is based on two conjectures. The first one is due to Bohigas, Giannoni, and Schmit, and states that the level statistics of quantum systems that have a classical chaotic counterpart are described by random matrix theory [128]. This conjecture has been verified in many cases [112]. So far, only non-generic counterexamples are found that violate this conjecture [129]. Indeed the emergence of

Wigner-Dyson statistics for the level separations is often considered as a defining property of a quantum chaotic system, even if there is no classical counterpart for such a system. The second conjecture is due to Berry [130]. It states that in the semi-classical limit ($\hbar \to 0$) of a quantum system whose classical analogue is chaotic, the Wigner function [131, 132] of eigenstates averaged over a vanishing small phase space reduces to the microcanonical distribution, and an observable is the same as in the microcanonical ensemble average.

The level statistics for quantum integrable systems was first addressed by Berry and Tabor [133]. Considering again a random matrix, but now with only diagonal terms (i.e., $H_{ij} = 0$ for $i \neq j$), this matrix represents a complex many-body system without inter-state correlation. For example, an array of independent harmonic oscillators with incommensurate frequencies, in which all possible total energies of the system can form such a random diagonal matrix. If the energies are uncorrelated random numbers, the probability of having n energy levels in a certain interval $[E, E+\Delta E]$ follows a Poissonian distribution: $Ps(n;\lambda) = \frac{\lambda^n}{n!}e^{-\lambda}$, where λ is the average number of energy levels in the interval. Assuming $\Delta E \propto \lambda$, the distribution for the separations of adjacent energies is obtained by requiring $n = 0$, so $P(\Delta E) = Ps(0;\Delta E) = e^{-\Delta E}$. Setting the average separation to one, $\Delta E \to \delta$, gives

$$P(\delta) = e^{-\delta}. \tag{2.24}$$

This distribution is very different from the expected from random matrix theory, Eq. (2.23). It has no level repulsion at $\delta \to 0$, and decays exponentially.

Berry and Tabor conjectured that, for quantum systems whose classical counterpart is integrable, the energy eigenvalues behave like a series of non-correlated random variables, that implies Poissonian statistics [133]. While for integrable quantum systems with no classical counterpart, there are exceptions [134]. In spite of that, as few-particle spectra become denser when going to the semi-classical limit (by either $E \to \infty$ or $\hbar \to 0$), and their level statistics approaches either the Poissonian or the Wigner-Dyson statistics, in many-particle systems one can achieve the same by taking the thermodynamic limit $L \to \infty$ and $N \to \infty$. It suggests that the level statistics indicators can also be applied to characterize a quantum many-body system that does not have a classical counterpart. Previous works have already demonstrated the potential of level statistics for the study of a quantum integrable system, for instance for spin-$\frac{1}{2}$ lattice models, quantum lattice gases consisting of interacting spinless fermions [142], or hard-core bosons [120].

Equations (2.23) and (2.24) are now regularly used for the analysis of quantum many-body systems. The statistics of the energy levels of a many-body Hamiltonian serves as

one of the main indicators of quantum chaos.

2.3.2. The two-level ratio

A convenient and widely-employed way to distinguish between Wigner-Dyson and Poisson statistics, is to calculate the two-level ratio [142]

$$r_\alpha = \frac{\min\{\delta_\alpha,\ \delta_{\alpha+1}\}}{\max\{\delta_\alpha,\ \delta_{\alpha+1}\})}, \tag{2.25}$$

where α is the label of an eigenstate, and $\delta_\alpha = E_{\alpha+1} - E_\alpha > 0$, is the difference between two adjacent energy levels. The mean value of the r_α for the two statistics is:

$$\bar{r} = \frac{1}{\Omega}\sum_{\alpha=1}^{\Omega} r_\alpha \simeq \begin{cases} 0.386 & \text{for Poisson,} \\ 0.529 & \text{for Wigner-Dyson.} \end{cases} \tag{2.26}$$

Note that Eq. (2.26) implies infinite temperature, as each state is assumed to be equally possible in the average. However, one may also evaluate the average $\bar{r}$ in a given spectral window.

Deviations from Poisson (or Wigner-Dyson) statistics are usually the result of symmetries of the Hamiltonian, which result in commensurability of the spectra and additional degeneracies. If the Hamiltonian has an overall symmetry, e.g., translation, reflection, particle-hole, etc., the energy levels can have extra degeneracies, and the statistics may be neither Poissonian nor Wigner-Dyson [135]. The underlying distributions of Eq. (2.23) and (2.24) can only be recovered when measurements are taken within the sub-space of the same conserved values. This consideration has been implemented in researches for various quantum lattice systems, as e.g. total momentum conservation in one-dimensional lattice models with next-to-nearest-neighbor hopping / interaction[120], or spin conservation in Heisenberg chains [136].

2.4. Many-body localization

In addition to integrable systems that might exhibit equilibrium characterized by the generalized Gibbs ensemble, there is an important class of systems that fail to equilibrate in any sense, and in which many-body eigenstates violate the eigenstate thermalization hypothesis. These are Anderson-localized systems. The concept of localization was first introduced by P. W. Anderson [137], and typically applies to systems with quenched

disorder.

The essential physics of Anderson localization can be illustrated with a tight-binding model of a single particle hopping in a lattice disturbed by a static random on-site potential. For strong enough disorder, in one- and two-dimensional systems all the eigenstates are exponentially localized, with wave functions that have the asymptotic long distance form $\psi_n(\mathbf{r}) \propto e^{-|\mathbf{r}-\mathbf{R}_n|/\xi}$, where ξ is the localization length depending on the disorder strength and the energy eigenvalue. This state a is localized near the site $\mathbf{R}_n$, and a particle remains localized near this location, if initially placed there. In other words, memory of the initial conditions is preserved in a local observable for infinite times. This manifestly constitutes a failure of the eigenstate thermalization hypothesis.

Recently, intensive efforts are made to investigate disordered many-body systems [85, 86, 87, 88], in which many-body localization (MBL) may occur, even though it's existence at thermodynamic limit is still a debate [138, 139, 140, 141]. Contrary to typical problems in many-body quantum system, the study of MBL is not focused on the ground-state or low-energy regime, but rather on the general spectrum of excited and even highly-excited states. In the non-interacting limit, the many-body eigenstates are simply product states of single-particle wave functions, and the system is hence fully localized. For finite interactions, the eigenstates can be constructed perturbatively if the on-site disorder is sufficiently larger than the interactions. Since in this regime the typical level splittings between neighboring sites are much larger than the interactions, the states on different sites are typically only weakly hybridized. This argument leads to the conclusion that for sufficiently strong disorder, particle or energy transport is absent, the eigenstate thermalization hypothesis therefore does not occur at any order in perturbation theory and MBL arises.

Although the perturbative argument is limited to the weak interaction regime, for one-dimensional disordered lattices, numerical evidence by exact diagonalization [142, 143], and analytical proof that follows physically reasonable assumptions [144] indicate that while the high-energy eigenstates do obey the eigenstate thermalization hypothesis for weak disorder, for strong-enough disorder all of the eigenstates violate it. Apparently, the violation of the eigenstate thermalization hypothesis occurs even for interactions exceeding the perturbative regime.

Based on the impressive experimental progress in ultracold gases in optical lattices, as discussed in Chapter 1, particular attention has been paid in recent years on the observation in those systems of Anderson (single particle) localization and MBL in the presence

of disorder [66, 67, 68, 145, 146, 147, 148].

2.4.1. Local integrals of motion

The level statistics (Sec. 2.3) has been applied for analysing the MBL transition [142, 143]. The spectrum reveals Wigner-Dyson statistics (with $\bar{r} \sim 0.529$) if the imposed disorder is less than a certain magnitude, indicating an ergodic phase. In contrast, disorder that exceeds the critical value leads to the MBL phase, which is characterized by a Poissonian spectrum (with $\bar{r} \sim 0.386$). Notably, this implies an unconventional type of integrals of motion that are exponentially localized, the so-called local integrals of motion (LIOM) [149]. Though the presence of disorder prevents diffraction-free scattering and the analytical integrability, the dynamics of particles in a strongly disordered lattice challenges the basic assumption of thermalization. The occurrence of the MBL phase conserves the positions of particles or the spin configurations, and permanently prevents the system from reaching equilibrium. Recent studies [144, 150, 151, 152, 153] have shown, both analytically and numerically, that MBL in systems with increasing disorder is asymptotically described by the emergence of LIOMs.

To be concrete, spin-$\frac{1}{2}$ lattices may be taken as a prototype model. Note that, as shown in Eq. (2.11), the spins are equivalent to hard-core bosons. It was suggested [150, 152] that with a strong on-site random potential, an MBL Hamiltonian can be written as a non-linear functional of a complete set of localized operators of pseudo-spins $\boldsymbol{\tau}_j$, that is,

$$\begin{aligned} H &= H(\sigma^x, \sigma^y, \sigma^z) \\ &\to h_0 + \sum_{\alpha} h_\alpha \tau_\alpha^z + \sum_{i,j} J_{ij} \tau_i^z \tau_j^z + \sum_{n=1}^{\infty} \sum_{i,j,\{k\}} K^n_{i\{k\}j} \tau_i^z \tau_{k_1}^z \cdots \tau_{k_n}^z \tau_j^z, \end{aligned} \tag{2.27}$$

where the K^n terms represent $(n+2)$-pseudo-spin interactions, the summations are restricted so that each interaction term is not repeatedly counted. The Ising spins τ_j^z (so-called l-bits) commute mutually with each other and with the Hamiltonian, thus the eigenstates of H are simultaneous eigenstates of all the τ_j^z. The intuition underlying Eq. (2.27) is that, since there is no transport in the MBL phase, there should be a set of localized conserved quantities behaving as constants of motion when the system evolves according to this Hamiltonian. For instance, for a system of hard-core bosons that fully localized in a disordered lattice, the τ_j^z are identical to the occupation numbers of the localized single-particle orbitals.

The localization of pseudo-spins $\boldsymbol{\tau}_j$ implies that their representation in $\boldsymbol{\sigma}_j$ operators

is given by a summation of $\boldsymbol{\sigma}_j$ products on nearby sites. The weight of each product term decay exponentially with the distance between the farthest $\boldsymbol{\sigma}_j$ that are involved. These exponential tails mediate interactions between the pseudo-spins that also fall off exponentially [152],

$$J_{\text{eff}} = J_{ij} + \sum_{n=1}^{\infty} \sum_{\{k\}} K^n_{i\{k\}j} \tau^z_{k_1} \cdots \tau^z_{k_n}. \tag{2.28}$$

In other words, the pseudo-spins $\boldsymbol{\tau}_j$ are dressed $\boldsymbol{\sigma}_j$, with local dressing that makes each τ^z_j conserved, and leads to the effective interactions above among $\boldsymbol{\tau}_j$s. The prototype model assumes that the τ^z_j has binary spectrum, and that the full spin algebra can be constructed with ladder operators $\tau^{\pm}_j$. More details on the construction of $\boldsymbol{\tau}_j$ for specific models are reviewed in Ref. [149].

2.4.2. Logarithmic growth of entanglement entropy

The assumption of LIOMs is sufficient to understand the MBL phenomenology, and very particularly the numerically observed logarithmic growth of entanglement in the MBL phase [154, 155]. In thermalizing systems, the interaction of two bits, A and B, causes them to become entangled with each other. The subsequent interaction of bits B and C produces entanglement not just between B and C but generically also between A and C. As a result, entanglement spreads typically ballistically. The situation is very different for the l-bits, since two l-bits can get entangled only by their direct interaction and not through a mutual interaction with a third l-bit. The latter is because the l-bit Hamiltonian (2.27) has no dissipation (no spin flips). As mentioned above the interaction between l-bits decays exponentially with the distance L between them, $J_{\text{eff}} \sim J_0 \exp(-L/\xi)$. If these two l-bits are initially not entangled, the interaction entangles them after a time t such that $tJ_{\text{eff}} \sim 1$. Hence, after a time t, entanglement is created between all l-bits within a distance $L \sim \xi \ln(tJ_0)$, explaining hence the observed logarithmic growth of entanglement with time within the MBL phase.

2.5. Disorder-free many-body localization

In recent years, various studies have posed the interesting question of whether MBL demands disorder, or whether in contrast many-body interacting systems may present MBL or MBL-like physics in the absence of disorder. Various scenarios have been considered.

A first scenario for disorder-free MBL is provided by system with two species of particles, one light and one heavy [94, 95]. Given a random initial distribution of the heavy

particles, one can then consider a Born-Oppenheimer approximation to the states of the light particles. If the heavy particles produce enough constraints (effective disorder), the light particles are localized by the heavy ones.

Another class of models is that of particles in the presence of a linear potential gradient. In the noninteracting limit, these models display the well-known Wannier-Stark localization. Beyond a critical value of the potential gradient these models exhibit nonergodic behavior as indicated by their spectral and dynamical properties [101]. In particular, these systems exhibits the so-called Stark-MBL [100], which is similar (but not identical) to the conventional MBL in disordered lattices. Very recently, Stark-MBL has been revealed in the context of ultracold gases, both in neutral atoms in optical lattices [105] and in trapped ions with long-range spin-exchange [107].

A candidate arising from pure many-body effects was suggested decades ago [156, 157], namely the system constituted by ^{3}He impurities in solid ^{4}He. Because of the power-law interactions between the impurities, the hop of a single impurity to a neighboring site then changes the energy of the system by an amount that depends on the locations of other impurities. Once the hopping is weak enough, random initial positions of the impurities are argued to localize by itself. In fact, due to the finite band width, many-body bound states can generally occur in lattices for strong-enough interactions. For an attractive interaction, $U < 0$, a pair of atoms at the same site will form a thermodynamically stable bound state for sufficiently large $|U|$. For $U > 0$, the pair is expected to be unstable, and will separate apart to minimize the repulsive interaction. This process is however forbidden if the repulsion is sufficiently large.

Dynamically stable (though possible not thermodynamically stable) repulsively-bound pair at the same site were observed in quantum gases in optical lattices [65, 158]. The origin for this repulsively-bound pair is provided by momentum and energy conservation, since there are no free scattering states available if the repulsive interaction exceeds the band width $\sim 2zJ$ (where z is, again, the coordination number). The repulsively bound state is actually the precise analog of the standard bound state below the band for attractive interactions, and there is a perfect symmetry around the band center. The presence of repulsively-bound pairs, even for weak interactions, leads to a strong slow-down of the dynamics [64, 159].

In this Thesis, we will show that polar lattice gases provide an excellent candidate for the observation of anomalously slow dynamics and MBL-like physics in disorder-free systems.

Chapter 3

Dimer clusters and self-bound lattice droplets in 1D polar lattice gases

In addition to energy conservation, tight-binding dynamics in deep optical lattices is largely determined by the finite bandwidth. This leads to the dynamical formation of (meta)stable states. A prominent example is that of a repulsively-bound pairs discussed at the end of the previous Chapter. Interestingly, in extended Hubbard models, strong-enough inter-site interactions, even just between nearest-neighbors, lead to non-local repulsively-bound pairs [160, 161] and clusters at different sites, which significantly slow down the dynamics [97]. In this Chapter, we show that the formation of dynamically-bound nearest-neighbor dimers leads, in the absence of disorder, to quasi-localization for surprisingly low densities and moderate dipole strengths. Moreover, superfluid self-bound lattice droplets form even for weak dipoles. Our results are directly relevant for current and future experiments on magnetic atoms and polar molecules.

The results of this Chapter have been published in Ref. [162].

3.1. Dynamically-bound dimers

We focus in this chapter on 1D polar lattice gases of hard core bosons described by the extended Hubbard model

$$H = -J\sum_{j}\left(\hat{a}^{\dagger}_{j+1}\hat{a}_{j} + \text{H. c.}\right) + \frac{V}{2}\sum_{i\neq j}\frac{1}{|i-j|^{3}}\hat{n}_{i}\hat{n}_{j}, \tag{3.1}$$

with J the hopping amplitude, V the interaction strength, $\hat{a}_j(\hat{a}^{\dagger}_j)$ the annihilation(creation) operator for particles at site j, and $\hat{n}_j = a^{\dagger}_j a_j$ the occupation on the site. Note that, in

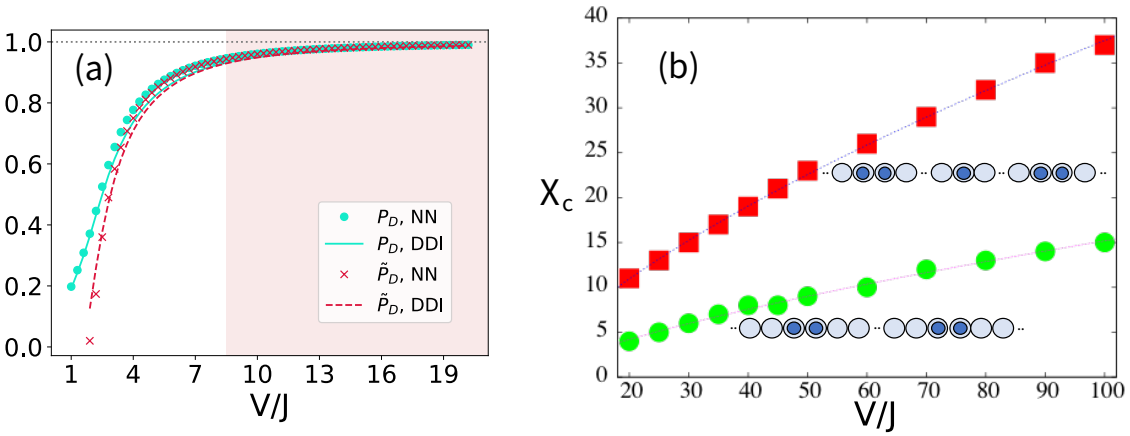

Figure 3.1: (a) Dimer stability characterized using P_D and $\tilde{P}_D$ (see the text), which provide very similar results. For $V/J \gtrsim 8$ both $P_D, \tilde{P}_D > 0.95$, indicating that an initially created nearest-neighbor dimer remains to a good approximation stationary. (b) Critical number of empty sites, X_c, between two dimers with (squares) and without (circles) a singlon in between them (see the inset). For an initial inter-dimer distance $X_0 < X_c$, the inter-dimer distance remains dynamically fixed (see the text), characterizing the formation of a dimer-dimer cluster. The dotted curves illustrate that in both cases, $X_c \propto (V/J)^{2/3}$.

order to focus on inter-site effects, we assume hard-core particles, i.e., $(a_j^\dagger)^2 = 0$, and hence $\hat{n}_j = 0$ or 1, such that on-site interactions (which would be given by Eq. (1.7)) can be excluded. This assumption can be realized by considering either large on-site interactions that prevent the gathering of more than one particle in a site, or by using spin-less fermions as the constituent particles of the lattice gas.

We will be particularly interested in the particle dynamics, and more specifically in how the formation of dynamically-bound dimers handicaps this particle motion.

3.1.1. Stability of dynamically-bound nearest-neighbor dimers

In order to assess the stability of nearest-neighbor dimers, we consider the two-body problem of formation of dynamically-bound dimers [97, 160, 161]. For two particles at sites j_1 and j_2, the center-of-mass and the relative distance are given by $R = (j_1+j_2)/2$ and $|j_1-j_2|$ respectively, thus the two-body state is denoted as $|R, r\rangle$. After applying the Fourier transform, $|K, r\rangle = \frac{1}{\sqrt{\Omega}} \sum_R e^{iKR} |R, r\rangle$, with K the center-of-mass quasi-momentum, the Hamiltonian for each K becomes of the form:

$$H_K = -2J \cos(K/2) \sum_{r\geq 1} (|K, r+1\rangle\langle K, r| + \text{H.c.}) + V \sum_{r\geq 1} \frac{1}{r^3} |K, r\rangle\langle K, r| \qquad (3.2)$$

After diagonalizing H_K, one obtains the eigenstates $|K,\alpha\rangle$ with eigenenergies ϵ_K^α. For a sufficiently large V the spectrum presents two different types of states (see Fig. 3.2), continuum scattering states and discrete bound states. The latter, irrespective of the sign of V, result in dynamically-bound pairs of particles. For $V > 0$, these states can be considered the inter-site equivalent of the on-site repulsively-bound pairs [65, 158], discussed in Sec. 2.5. For a sufficiently large V there is a bound-state, which, as discussed below, corresponds to a very good approximation to a nearest-neighbor dimer. Other types of pairs, e.g. next-to-nearest-neighbor dimers, may occur as well, but for the purposes of this chapter only the stability of nearest-neighbor dimers is relevant. Since H_K has maximum hopping amplitude at $K = 0$, one may consider $K = 0$ for a conservative estimation. For $V > 0$, the eigenstate that holds the two particles at the shortest average relative distance, is the most energetic one, $|K = 0, \alpha_{max}\rangle$. For a sufficiently large V, $|K, r = 1\rangle$ is a good approximation to a dimer, the overlapping,

$$\tilde{P}_D = |\langle \alpha_{max}|r = 1\rangle_{K=0}|^2, \tag{3.3}$$

may be hence employed as a measure of nearest-neighbor dimer stability. Figure 3.1 (a) shows that for $V/J \gtrsim 8$ the tightest bound-state is over 90% a nearest-neighbor dimer, and hence an initially created nearest-neighbor dimer remains to a very good approximation stationary, i.e., bound to nearest-neighbor.

As a final remark, we would like to mention that an alternative way to to quantify the stability of a nearest-neighbor dimer, is to consider the survival probability within the sub-space of all $|j, j+1\rangle$ states, rather than just in the original one $|j_0, j_0+1\rangle$. For an asymptotically long time:

$$P_D = \sum_{j,\alpha} |\langle \alpha|j_0, j_0+1\rangle|^2 |\langle \alpha|j, j+1\rangle|^2, \tag{3.4}$$

which provides a very similar information as $\tilde{P}_D$ (see Fig. 3.1(a)).

3.1.2. Dimers for purely nearest-neighbor interactions

Dynamically-bound dimers are particularly easy to evaluate for the case of purely nearest-neighbor interactions $V\sum_j \hat{n}_j\hat{n}_{j+1}$ using the results of Sec. 2.2.2. The two-body wavefunction, of Eq. (2.17) can be written as $\Psi(x_1, x_2) = e^{iRK/2}\,\psi(r,k)$, with

$$\psi(r,k) = e^{irk} - e^{i\theta(k)}e^{-irk} \tag{3.5}$$

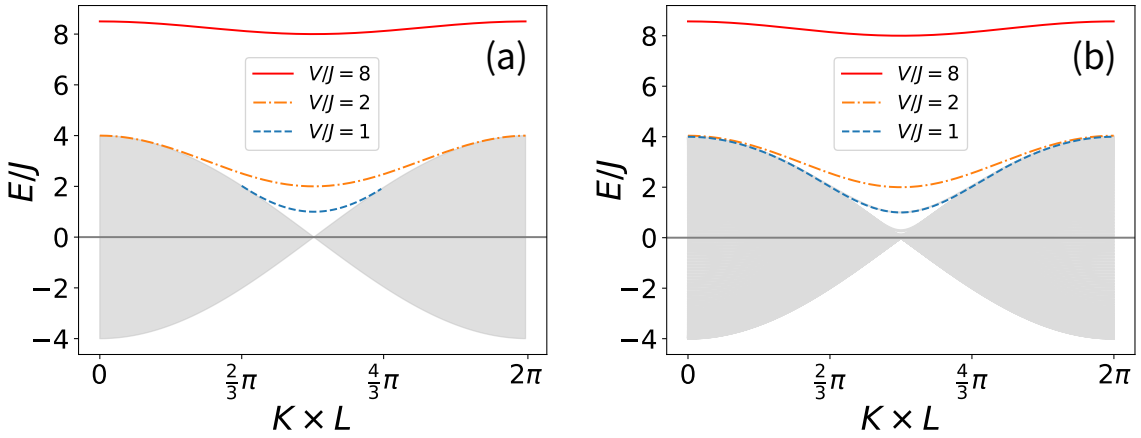

Figure 3.2: (a) Two-particle dispersion of the nearest-neighbor model, where the scattering continuum is given by Eq. (3.6), and the bound states by Eq. (3.10). (b) Two-particle dispersion of polar lattice gas, Eq. (3.1). It shows bound states very similar to those of the nearest-neighbor model.

with $K = k_1 + k_2$, $k = k_2 - k_1$, $R = x_1 + x_2$, and $r = x_2 - x_1 \geq 1$. The energy given by Eq. (2.18) is

$$E = \omega(k_1) + \omega(k_2) = -4J\cos\left(\frac{K}{2}\right)\cos\left(\frac{k}{2}\right), \tag{3.6}$$

whereas the phase shift given by Eq. (2.21) is

$$e^{i\theta(k)} = \frac{1 + \Delta e^{ik/2}}{1 + \Delta e^{-ik/2}}, \tag{3.7}$$

with $\Delta = \frac{V}{2J\cos(K/2)}$.

A standard method to identify a bound state is to perform analytical continuation to complex momenta, and then search for points where the scattering amplitude becomes infinite. The physical motivation is that in a bound state waves are tied around a center, that is, it exists by itself without the need of any incoming wave. This leaves the relative proportion between the outgoing wave and the incoming wave to be infinite [163]. To let k_1 and k_2 be complex, while the total momentum $k_1 + k_2 = K$ remains real, one takes $z = q + i\kappa$, then let $k_1 \to \frac{K}{2} + z$ and $k_2 \to \frac{K}{2} - z$, so the relative momentum $k = k_2 - k_1 = -2q - 2i\kappa$. Substituting these complex momenta into Eq. (3.6), and requiring the energy to be also real, one obtains $q = l\pi$, with l an arbitrary integer, and

$$E = \mp 4J\cos(K/2)\cosh(\kappa). \tag{3.8}$$

The upper(lower) sign is for even(odd) l. The complex k leaves the two-body wavefunction,

Eq. (3.5), in the form $\psi(r,k) = \pm e^{\kappa r} \mp e^{i\theta(k)} e^{-\kappa r}$. So once $e^{i\theta(k)} \to \infty$, $\psi \to e^{-\kappa r}$, and the wavefunction is bound, as expected. From Eq. (3.7) one obtains the condition for bound state

$$\begin{aligned} e^{i\theta(k=-2l\pi-2i\kappa)} &= \frac{1+(-1)^l \Delta e^{\kappa}}{1+(-1)^l \Delta e^{-\kappa}} \to \infty \\ \Rightarrow V &= \mp 2Je^{\kappa}\cos(K/2). \end{aligned} \tag{3.9}$$

This expression reveals that bound states can exist generally in the lattice irrespective whether the interaction is repulsive or attractive. Putting Eq. (3.9) into Eq. (3.8) gives the bound state energy

$$E = V + \frac{2J^2}{V} + \frac{2J^2}{V}\cos(K). \tag{3.10}$$

For $|V| \leq 2J$, the bound state energy overlaps for all K with the scattering continuum, given by Eq. (3.6). For $|V| > 4J$, the band of bound states splits for all K completely from the continuum. The dispersion for various V/J is shown in Fig. 3.2 (a).

3.1.3. Dimer model

Even if dimers remain bound, they may move in the lattice by a second-order process by two consecutive hops. When the right particle of the pair moves to the right the potential energy changes from V to $V/8$. The subsequent hop of the left particle to the right, restores the original energy. As derived in Appendix A, this results in a dimer hopping amplitude $J_D = \frac{J^2}{V-V/8}$. We consider at this point that the system consists only of nearest-neighbor dimers (this condition is relaxed below). This can be realized by superimposing a superlattice on top of the primary lattice [68], which dimerizes the lattice. Once the dimer gas is created, the superlattice is removed, and the dimers are allowed to move in the primary lattice. As shown below, this dynamics is largerly handicapped by the formation of dimer-dimer clusters.

Dimer-dimer clusterization can be evaluated by approximating the four-body dimer-dimer problem by a simplified two-body problem, using the Hamiltonian

$$H_D = J_D \sum_j \left(\hat{d}^{\dagger}_{j+1} \hat{d}_j + H.c. \right) + V \sum_j \sum_{x \geq 2} G(x) \hat{D}_j \hat{D}_{j+x}, \tag{3.11}$$

where $\hat{d}_l = \hat{a}_l \hat{a}_{l+1}$ that creates a dimer at sites l and $l+1$, $\hat{D}_l = \hat{d}^{\dagger}_l \hat{d}_l$, and the function

$$G(x) = \frac{2}{x^3} + \frac{1}{(x-1)^3} + \frac{1}{(x+1)^3}$$

characterizes the interaction between two dimers separated by $x-1$ sites.

Similarly to Eq. (3.2), for a center-of-mass momentum $K = 0$ of the dimer-dimer complex, the Hamiltonian is

$$H_{D,K=0} = -2J_D \sum_{x\geq 2} (|x\rangle\langle x+1| + \text{H. c.}) + V \sum_{x\geq 2} G(x)|x\rangle\langle x|, \tag{3.12}$$

where $|x\rangle$ denotes two dimers at $|j, j+1\rangle$ and $|j+x, j+x+1\rangle$. For an arbitrary initial state $|x_0\rangle$ (two dimers with $X_0 = x_0 - 2$ empty sites in between), time evolution govern by $H_{D,K=0}$ gives the average dimer-dimer distance $\langle X\rangle(t)$, and the variance $\Delta X(t) = \sqrt{\langle X^2\rangle - \langle X\rangle^2}$. For different values of V, a critical X_c for the stability of the dimer-dimer complex is defined, such that for $X_0 < X_c$ in the subsequent evolution up to $J_D t = 100$, $\Delta X < \sqrt{\langle X_0\rangle}$, that is, the inter-dimer distance remains well-defined and approximately equal to the original one. As expected from a simple inspection of H_D, $X_c \propto (V/J)^{2/3}$ (Fig. 3.1 (b)).

3.1.4. Dimer dynamics

Dimer clusters strongly slow down the dynamics, as illustrated (see Fig. 3.3 (a)) by the Shannon entropy

$$S_{shn}(t) = -\sum_f |\langle f|D_1, D_2\rangle_t|^2 \ln |\langle f|D_1, D_2\rangle_t|^2, \tag{3.13}$$

with $\{|f\rangle\}$ the Fock basis, $|D_1, D_2\rangle$ a selected two-dimer initial state, and $|D_1, D_2\rangle_t$ the time evolution of $|D_1, D_2\rangle$. For $J_D t \ll 1$, $S_{shn}(t)$ remains very low, since dimers move via second-order hopping. For $J_D t \gtrsim 1$, the dimer cluster quickly unravels for $X_0 > X_c$, reaching a maximal entropy $S_{shn}^{max} \simeq 2 \ln N_s$. For $X_0 < X_c$, a stable dimer cluster is formed. $S(t)$ increases much more slowly, and only for $J_D t \gg 1$ due to the center-of-mass motion of the dimer cluster, up to S_{shn}^{max} that is determined from the dimension of the dynamically available Hilbert space Ω_{sub}, i.e., $S_{shn}^{max} = \log(\Omega_{sub})$. For the case of two un-bond dimers, $\Omega_{sub} \sim L^2$, whereas for bound dimers at a rigid fixed distance, $\Omega_{sub} \sim L$.

The nature of the short-time plateaux of Fig. 3.3 (a) is different for $V/J = 12$ and for $V/J = 42$. For $V/J = 12$, the atoms within the dimers are not fully rigidly bound at nearest-neighbors, but rather have small probability to separate to next-nearest neighbors. This slight spreading explains the entropy growth for $t \sim 1/J$. This initial growth is followed by a plateau, because any further entropy growth demands the dimer motion,

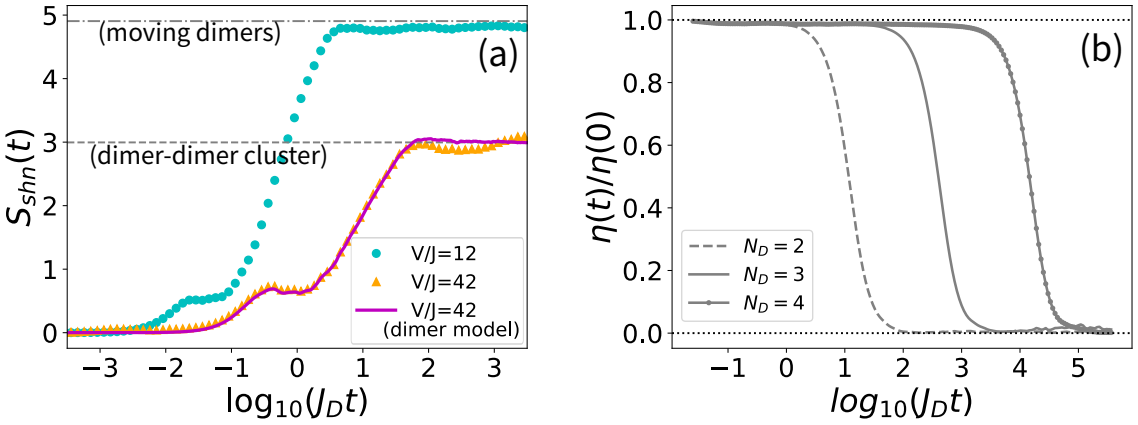

Figure 3.3: (a) Shannon entropy of a two-dimer system obtained by exact evolution of Eq. (3.1) and Eq. (3.11). The dimers are initially separated by $X_0 = 5$, whereas the overall lattice has 20 sites. (b) Inhomogeneity parameter (see text) evaluated using exact evolution of Eq. (3.11) with $V/J = 40$, $X_0 = 3$, and various number of dimers, $N_D = 2$ (dashed), 3 (solid), and 4 (solid dots) in $5(N_D + 1)$ sites, where $\rho \simeq 0.3$. We consider periodic boundary conditions in all cases.

which occurs at $t \sim 1/J_D \gg 1/J$. This entropy growth then proceeds unhindered since no dimer cluster forms. For $V/J = 42$ the dimers are rigidly formed by nearest-neighbor particles, and the dimer model successfully recovers quantitatively the dynamics of the full Hamiltonian (solid curve in Fig. 3.3 (a)). As a consequence, entropy growth at the $1/J$ time scale is prevented. The small entropy growth at $t \sim 1/J_D$ is due to the slightly undefined relative inter-dimer distance having a finite variance $\Delta X \ll X_0$. That growth of $S_{shn}(t)$ is followed by a plateau, since further entropy growth demands the motion of the whole dimer-dimer cluster, which occurs in a much longer time scale.

The emerging polar dimer cluster strongly slows down the dynamics, since motion may result only from the displacement of the center-of-mass of the whole dimer cluster. A cluster of more than two dimers further reduces the mobility of the center-of-mass. As more dimers are bound, the cluster hopping amplitude is in the order of $J_D^{N_D}/V^{N_D-1} \propto J^{2N_D}/V^{2N_D-1}$, with N_D, the number of dimers. This slow-down is shown in Fig. 3.3 (b), where, for $V/J = 40$, the inhomogeneity $\eta(t) = \sum_j (\langle \hat{n}_j \rangle - N/L)^2$ is obtained using the exact evolution of the dimer model, Eq. (3.11), for $N_D = 2$, 3, and 4. For each time t we average over a small time interval $t \pm \mathrm{d}t$ to smoothen fluctuations. Note that $\eta(t) \to 0$ indicates homogenization (and hence complete loss of information about the initial conditions). The time scale for homogeneization increases by more than one order of magnitude with every dimer added to the cluster. Dimers in polar lattice gases thus

have a much stronger effect than on-site bound pairs [164]. The latter merely leads to a slow-down due to the larger mass of the pair. In contrast, the hopping of nearest-neighbor dimers is out-competed by the tail $G(x)$ even at large distances, leading to dynamical localization via clustering even for dilute gases and moderate dipoles. Since dimers remain at a fixed distance for all initial separations $X < X_c$, multi-dimer localization can exist with general initial separation, an initial crystalline distribution is not essential for clusterization-induced localization.

3.2. Brownian motion

The presence of unpaired particles (singlons) significantly modified the dynamics of the system. Figure 3.4 (a) depicts S_{shn} for a singlon initially between two dimers separated by $X_0 = 7$. For small $V/J = 12$, the initial state quickly unravels at a time scales $t \sim 1/J$ instead of $t \sim 1/J_D$ as in Fig. 3.3 (a) for a pure dimers gas, and S_{shn} reaches $S_{shn}^{max} \simeq 3 \times \ln L$. At an intermediate regime of V/J, nearest-neighbor dimers are strongly bound, but singlons induced dimer mobility due to mechanism that resembles the well-known Brownian motion. Once a singlon approaches a dimer at one site of distance, dimer and singlon may resonantly swap positions:

$$|\cdots\circ\circ\bullet\bullet\circ\circ\bullet\circ\cdots\rangle \to |\cdots\circ\circ\bullet\bullet\circ\bullet\circ\circ\cdots\rangle$$
$$\to |\cdots\circ\circ\bullet\circ\bullet\bullet\circ\circ\cdots\rangle \to |\cdots\circ\bullet\circ\circ\bullet\bullet\circ\circ\cdots\rangle,$$

where $\circ$ ($\bullet$) denotes an empty (occupied) site (we will come back to this mechanism in the next chapter when discussing delocalization in nearest-neighbor models). These swaps result in dimer recoils, which induce a Brownian-like dimer motion for $t > 1/J$. Note that in Fig. 3.4 (a) we consider periodic boundary conditions, and hence the single singlon winds around the system mimicking the behavior of dimers in a singlon bath. The effect of Brownian-like motion can be observed for $V/J = 37$ for times $1/J_D \gtrsim t \gtrsim 1/J$. That is the time window when dimer hopping did not yet happen but siglon motion has led already to dimer mobility. At $t > 1/J_D$, the S_{shn} increases by the combination of dimer hopping and Brownian-like motion up to a maximal $S_{shn}^{max} \sim \ln L + \ln X_0$, which may be estimated by considering dimers bound with a fixed distance X_0 and a moving singlon in between.

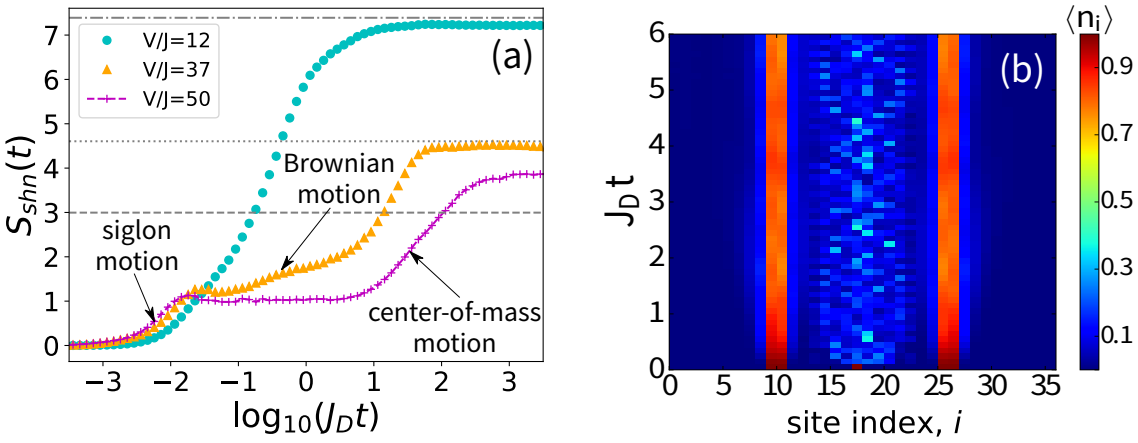

Figure 3.4: (a) Shannon entropy of two dimers with a singlon in between them. The initial inter-dimer separation is $X_0 = 7$. Other parameters are similar to those of Fig. 3.3 (a). (b) $\langle n_j(t) \rangle$ evaluated by t-DMRG for $V/J = 50$, $X_0 = 15$, and with open boundary conditions. The singlon quickly delocalizes in the inter-dimer space, but the dimers remain fixed for $t \gg 1/J_D$, revealing the formation of a singlon-glued dimer cluster.

3.3. Singlon gluing

Brownian motion is absent for large V, as seen for $V/J = 50$ in Fig. 3.4 (a), for which singlons and dimers cannot approach at one site of distance. This results in a dramatic singlon-induced enhancement of the inter-dimer binding. Due to the DDI, the singlon between two dimers experiences a box-like trapping potential, which induces discrete energy levels for the singlon. A change in the inter-dimer distance induced by dimer hopping results in an energy change of the singlon, which for a sufficiently small inter-dimer distance outcompetes the dimer hopping, resulting in the blocking of the dimer motion. As a results dimers block singlons and singlons block in turn dimers. This leads to singlon-gluing of the inter-dimer cluster, resulting in a significant enhancements of the critical inter-dimer distance for dimer-dimer clusterization. As a result, the presence of singlons results in a strong reduction of the critical lattice filling for clusterization-induced localization. Figure 3.4 (b) shows that two dimers at an initial distance of $X_0 = 15$ sites remain tightly bound due to the singlon-gluing, despite the tiny dimer-dimer interaction $V \times G(x) \sim 0.02J$. This mechanism resembles that discussed, for non-polar gases, in Refs. [94, 95] (recall Sec. 2.5), and also for polar gases in Ref. [97], in which the interplay between slow and fast particles (here dimers and singlons) was shown to result in quasi many-body localization. However the surprisingly strong role of the DDI tail, crucial here, was overlooked in Ref. [97].

A simplified model can be introduced to capture the singlon-gluing effect. Considering

a singlon placed between two stable dimers, $|D_l\rangle$ and $|D_{l+x}\rangle$. For simplicity, the Brownian-like motion is ignored, this approximation is valid for $V \gg J$. In absence of dimer motion, the potential experienced by the singlon within the effective box is

$$U(n) = V\left[f_{DS}(n,l) + f_{DS}(n,l+x)\right],$$

with $n \in [l+2, l+x-1]$ denoting the box regime, and

$$f_{DS}(n,l) = \frac{1}{|n-l|^3} + \frac{1}{|n-(l+1)|^3}$$

characterizing the effect of the dipolar tail. The states of the dimer-singlon-dimer (DSD) system are of the form

$$|\psi^{\alpha}_{l,x}\rangle = |D_l\rangle \otimes |\phi^{\alpha}_x\rangle \otimes |D_{l+x}\rangle.$$

Where $|D_l\rangle$ denotes a dimer placed at sites l and $l+1$, and the states $|\phi^{\alpha=1,\ldots,x-2}_x\rangle$ are the singlon eigenstates in the effective box potential, with a corresponding singlon energy ε^{α}_x. We perform the Fourier transform

$$|\psi^{\alpha}_{K,x}\rangle = \frac{1}{\Omega}\sum_l e^{iK(2l+x+1)/2}|\psi^{\alpha}_{l,x}\rangle,$$

with K the center-of-mass quasi-momentum of the dimer-dimer pair. As above in Eq. (3.2), the analysis is focused on $K=0$, and hence the estimation is once more conservative. Dimer hopping, J_D, couples $|\psi^{\alpha}_x\rangle$ with $|\psi^{\beta}_{x\pm1}\rangle$. The effective Hamiltonian for the system is hence given by:

$$H_{DSD} = \sum_{x,\alpha}\left(\varepsilon^{\alpha}_x + V\cdot G(x)\right)|\psi^{\alpha}_x\rangle\langle\psi^{\alpha}_x| - J_D\sum_{x,\alpha,\beta}\left[C^{\alpha,\beta}_x|\psi^{j+1}_{n'}\rangle\langle\psi^{j}_{n}| + \text{H.c.}\right], \tag{3.14}$$

where $G(x)$ is the dimer-dimer interaction discussed above (Eq. (3.11)), and the coupling between states of different inter-dimer distance is characterized by the overlappings

$$C^{\alpha,\beta}_x = \sum_{s=2}^{x-1}\phi^{\alpha}_x(s)\left[\phi^{\beta}_x(s+1) + \phi^{\beta}_x(s)\right],$$

with $\phi^{\alpha}_x(s)$ the amplitude of the state $|\phi^{\alpha}_x\rangle$ in site $l+s$.

Let the two dimers be initially separated by X_0 empty sites, with the singlon in the middle of them. H_{DSD} provides the time evolution for the dimer-singlon-dimer state. Similar to the dimer-dimer case, the critical initial separation X_c is defined such that for

$X_0 < X_c$, one has $\Delta L < \sqrt{L_0}$ for $J_D t = 100$. We obtain in this way the results of Fig. 3.1 (b), which show that that X_c, which remains proportional to $(V/J)^{2/3}$, is very significantly enhanced in the presence of an intermediate singlon.

Singlon-gluing crucially affects the dynamics of even dilute gases for moderate dipoles. A lattice gas with filling $\rho \ll 1$ is formed mainly by singlons, with a small dimer density $\rho_D \sim \rho^2$. Hence, for a sufficiently large V that precludes Brownian motion, singlon-gluing leads to dimer clustering for $\rho \gtrsim \rho_c \sim X_c^{-1/2}$. As in the dimer gas without singlons, larger clusters of more than two dimers prevent the center-of-mass motion that results in the long-time entropy growth of Fig. 3.3 (b). Hence even moderate DDI results for very low densities (for $V/J = 50$, $\rho_c \sim 0.2$) into dynamical localization via massive dimer clustering.

It is worth emphasizing that the estimation here is very conservative, since it considered neither nearest-neighbor bound states with more than two particles nor the formation of dimers beyond nearest neighbors, which for sufficiently large V/J may become bound and stable as well. Their presence will result in a stronger localization of the lattice gas. Note as well, that for lower ρ, the formation of dimer clusters, even if they do not bind all dimers in the system, already constrains very severely the dynamics. The required $|V|/J$ values are achievable with current state-of-the-art technology. For ^{164}Dy in an UV lattice with 180nm spacing and depth of 23 recoil energies, $|V|/J \sim 30$, with $J/\hbar \sim 93\text{s}^{-1}$. The dimer-hopping time is $1/J_D \simeq 280$ms. Dimer clustering may then be probed in few seconds, well within experimental lifetimes.

3.4. Self-bound polar lattice droplets

The dynamics of lattice gases may be dramatically impacted even by a much weaker dipolar interaction than that considered in the discussion above. As shown below, for a sufficiently dense initial polar lattice gas, ratios V/J already attainable in experiments may result in the formation of self-bound (and self-pinned) polar lattice droplets.

Let us consider N hard-core bosons in a lattice with L sites, initially with no inter-site interactions, $V = 0$. The latter can be accomplished by tuning the orientation of the dipoles into the magic angle $\theta = \arccos(1/\sqrt{3})$. We assume that the gas is initially trapped by a box potential within a region that occupies one half of the overall lattice, $L_{box} = L/2$. Note, however, that more general confinements, as e.g. harmonic traps do not significantly modify our conclusions. At $t = 0$, the box trap is released, and the angle θ is tuned to zero, such that the inter-site interaction, i.e. V, is switched on. We consider in the following

initial particle densities $0.4 \lesssim \rho_0 = \frac{N}{L_{box}} \leq 1$. We characterized the dynamical self-bound character of the lattice gases by means of the self-trapping parameter

$$M(V/J) = \frac{\bar{\rho}(V/J) - N/L}{\rho_0 - N/L}, \tag{3.15}$$

where

$$\bar{\rho}(V/J) = \frac{1}{LT} \int_0^T \sum_{j \in box} \langle \hat{n}_j(V/J, t) \rangle \mathrm{d}t$$

is the time averaged density within the originally box regime. The time scale T is determined by requiring $M \to 0$ for $V/J = 0$. Note that $M \to 0$ if the lattice gas is not self-bound, whereas $M \to 1$ if the original box-trapped gas coincides with the self-bound solution. We may estimate as a function of ρ_0 the critical value V_c/J such that the lattice droplet remains self-bound, which we fix by requiring (somehow arbitrarily) $M > 0.4$. The resulting "phase diagram" is depicted in Fig. 3.5 (a).

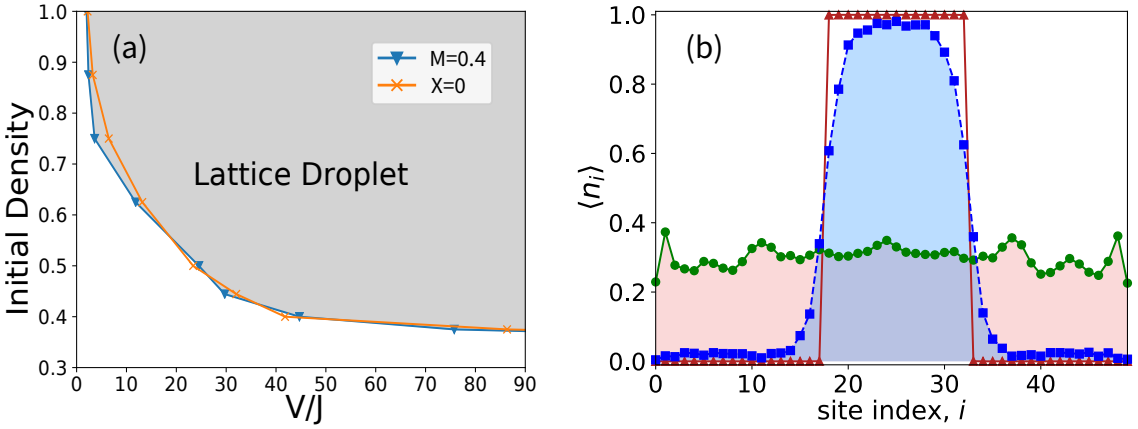

Figure 3.5: (a) Phase diagram of a lattice droplet, where the shaded region corresponds to the regime with self-bound droplets. The transition line is evaluated (see text) following the criterion $M = 0.4$ (triangles), and $X = 0$ (crosses). The data at $\rho_0 = 0.44$ and 0.4 are obtained with $L = 9$ and 10 respectively, and the rest is with $L = 8$. (b) Time evolution of the density distribution, obtained by t-DMRG simulation [165] of the system described by Eq. (3.1). A gas is initially confined with $\rho = 1$ (red triangles) and after release it is evolved for $Jt = 30$. A self-bound lattice droplet reveals itself for $V/J = 2.5$ (blue squares), whereas for $V/J = 1$ (green circles) the gas expands. We consider open boundary conditions in both cases.

An alternative analysis of the self-localization of the lattice droplet is provided by the eigenstate properties. For a sufficiently large V/J, the dynamically available Hilbert space is strongly reduced (see the discussion on Hilbert space fragmentation later on in the Thesis). In other words, a given eigenstate just projects on very few Fock states when

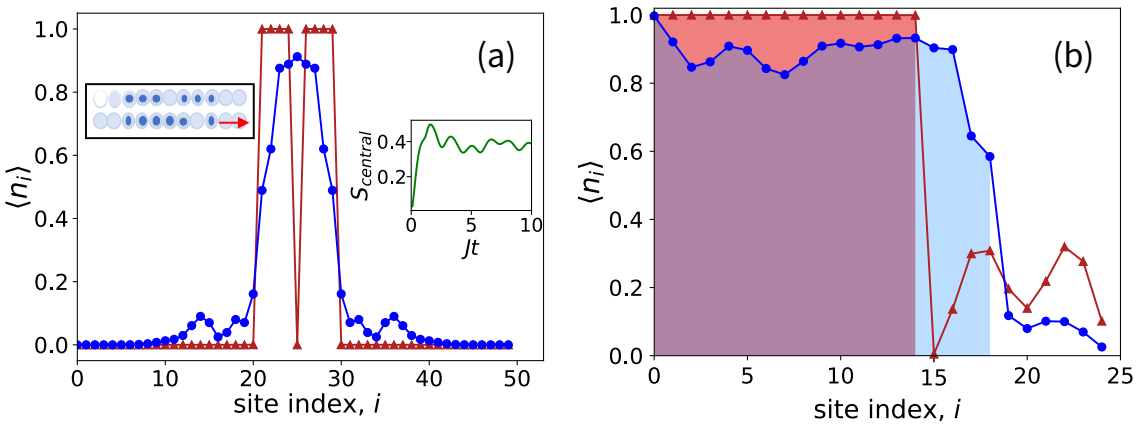

Figure 3.6: (a) Droplet with a holon initially at the center (red triangles) after $Jt = 6$ (blue circles), for $V/J = 30$. Partial holon evaporation results in particle ejection (left inset). This ejection is however inefficient, as shown by the particle-hole entropy averaged over the five central sites (right inset). (b) Initial droplet with $\rho = 1$ and two singlons outside (red triangles) after $Jt = 55$ (blue circles). The shadowed region is that of the droplet. Note the singlon aggregation at the droplet edge. The results are obtained by means of t-DMRG simulations of Eq. (3.1) with open boundary conditions.

$V \to \infty$, whereas for small $V \to 0$ the eigenstates are delocalized, they spread over the whole Fock space with approximately equal amplitude $\sim 1/\sqrt{\Omega}$, with Ω the Hilbert-space dimension.

To determine whether a given eigenstate is "closer" to a narrow distribution of few Fock-state components, or to a spread distribution of all Fock states, one can calculate the deviations

$$\Delta_\alpha^0 = \sqrt{\frac{1}{\Omega}\sum_f \left(|\langle f|\alpha\rangle| - \frac{1}{\sqrt{\Omega}}\right)^2},$$
$$\Delta_\alpha^1 = \sqrt{\frac{1}{\Omega}\sum_f \left(|\langle f|\alpha\rangle| - \delta_{f,f_\alpha^{max}}\right)^2},$$

where $|\alpha\rangle$ is the given eigenstate, f runs over all Fock states, and f_α^{max} is the Fock-state that has the largest amplitude on $|\alpha\rangle$, i.e., $\langle\alpha|f_\alpha^{max}\rangle = \max\{|\langle\alpha|f_1\rangle|, |\langle\alpha|f_2\rangle|, |\langle\alpha|f_3\rangle| \cdots\}$. For the initial ground state gas in the box $|G_{box}\rangle = \sum_f c_f|f\rangle = \sum_{f,\alpha} c_f\langle\alpha|f\rangle|\alpha\rangle$, one may define

$$X = \sum_{f,\alpha} c_f^2 |\langle\alpha|f\rangle|^2(\Delta_\alpha^0 - \Delta_\alpha^1). \tag{3.16}$$

The transition between self-bound and non-self-bound lattice droplets is marked by $X = 0$. As shown in Fig. 3.5 (a), the result of this analysis is in very good agreement with the

the transition obtained from the previous analysis of the self-trapping parameter M.

In contrast to non-polar experiments [64, 159], where stable or partially-stable on-site bound pairs still allowed for an overall (slowed-down) expansion, in the polar case there is a critical $V_c(\rho)$ such that the cloud remains self-bound (Fig. 3.5 (a)). These self-bound lattice droplets present a finite final average $\rho' < 1$ (Fig. 3.5 (b)), in other words, holons (empty sites) remain mobile but confined within a droplet. As a result, lattice droplets remain superfluid. For $\rho = 1$, droplets occur already for $V/J \simeq 2.5$. For current ^{166}Er experiments [47], with a lattice spacing of 266nm and a typical lattice depth of 20 recoil energies, $V/J \simeq 2.7$, with a hopping time $1/J = 6.5$ms. Self-bound lattice droplets are hence already within reach of current on-going experiments.

For large-enough V, holons remain confined in the droplet due to the potential exerted by the droplet boundaries via the dipolar tail. For $V/J \lesssim 8$ (Fig. 3.6 (a)), this mechanism is insufficient, since only nearest-neighbor terms are relevant. A holon, initially inside a droplet with $\rho = 1$, expands by resonant hops up to the edges. At that point, the last particle may escape without breaking any nearest-neighbor bond (left inset of Fig. 3.6 (a)). This holon evaporation becomes drastically inefficient for growing droplet sizes, since the holon quickly spreads uniformly within the droplet (right inset of Fig. 3.6(a)). Therefore, holons remain confined within the droplet. The converse also occurs: a singlon may stick to the droplet edge, pushing a holon inside (Fig. 3.6(b)). Mobile holons inside the droplet may be revealed using quantum gas microscopy.

3.5. Conclusions

Polar gases in 1D lattices present a severely constrained dynamics. Dynamically-bound dimers dramatically enhance the role of the dipolar tail, leading to dynamical localization in absence of disorder via dimer clustering even for low densities and moderate dipole moments. Moreover, polar gases may form, even for weak dipoles, self-bound superfluid lattice droplets, and will leave inherent difficulties in particle-hole entropy removal in polar lattice gases. Results in this chapter are directly relevant for current lanthanide experiments and future experiments with polar molecules, and may be easily extrapolated to other power-law interactions, $V/|i-j|^s$.

Generalization to higher dimensions is also directly available. Whereas singlon-gluing just occurs in 1D, since it requires singlon confinement between dimers, clusterization due to dimer-dimer DDI and self-bound lattice droplets occur also in higher-dimensions. For square lattices, X_c is only slightly modified compared to 1D. The critical lattice

filling for dimer localization via clustering scales however as $\rho_c \sim 1/X_c$, and hence for moderate $V/J \sim 30$, $\rho_c \lesssim 0.1$. Furthermore, in contrast to 1D, when removing the overall confinement, but keeping the lattice on, singlons evaporate leaving an immobile dimer cluster behind despite the extremely dilute dimer density $\rho_D \sim \rho_c^2$. This must be compared to clusters of non-polar repulsive bond pairs resulting from quantum distillation [164] which occur at a unit filling of pairs. We should finally mention that dimer motion in other 2D lattice geometries, or in square lattice under soft-core conditions, presents additional intriguing properties that will be discussed separately in Chapter 6.

Chapter 4

Hilbert-space fragmentation and localization in one-dimensional nearest-neighbor models

As discussed in Chapter 2, ergodicity may be broken in the presence of quenched disorder even in the presence of interactions, leading to the phenomenon of many-body localization. In this chapter, we discuss many-body localization in the strongly-interacting nearest-neighbor model, leaning heavily on Refs. [166] and Ref. [167]. This discussion sets the proper frame for the study of localization in polar lattice gases discussed in the next chapter.

An important issue of interest for this chapter, and especially for the next one, concerns the currently very active question of whether phenomenology similar to that of many-body localization may appear in the absence of disorder (recall Sec. 2.5). Disorder-free localization occurs naturally due to dynamical constraints [92, 93]. These constraints, which result in a finite number of conservation laws, induce the fragmentation of the Hilbert space into disconnected subspaces that severely limits the dynamics [167, 168, 169, 170, 171, 172, 173]. Hilbert-space fragmentation is also closely connected to the phenomenon of quantum scars [174].

Ultra-cold gases in optical lattices or reconfigurable tweezer arrays provide a well-controlled scenario for the study of many-body dynamics, including many-body localization [68, 69], and quantum scars [175]. Recent experiments on tilted Fermi-Hubbard chains [105] and in a trapped-ion quantum simulator [107] have provided evidence of non-ergodic behavior in absence of disorder, unveiling the potential of ultra-cold gases for the

study of disorder-free many-body localization and Hilbert-space fragmentation. It is hence particularly relevant to find other promising ultra-cold scenarios for the study of fragmentation due to interaction-induced constraints. As shown in the next chapter, polar lattice gases are a natural candidate.

As discussed in this chapter, models with only nearest-neighbor interactions may present Hilbert-space fragmentation, but they do not present in general disorder-free localization, due to the possibility of resonant motion even for infinitely large interactions. In contrast, as shown in the next chapter, such a resonant motion is not possible in polar lattice gases.

4.1. The nearest-neighbor model

In this chapter we focus on the nearest-neighbor extended Hubbard model for hard-core bosons, which, as already mentioned in previous chapters, is equivalent (via a Holstein-Primakoff transformation) to the XXZ spin model (Eq. 2.12). Imposing random on-site energies, the Hamiltonian of the model acquires the form:

$$H = -J \sum_j \left(\hat{a}^\dagger_{j+1} \hat{a}_j + H.c. \right) + V \sum_j \hat{n}_{j+1} \hat{n}_j + W \sum_j h_j \hat{n}_j, \tag{4.1}$$

where W denotes the disorder strength, h_j are real random numbers uniformly distributed in the domain $[-1, 1]$, and as in previous chapters V denotes the inter-site nearest-neighbor interaction, and J the hopping rate. We pay particular attention below to the strongly-interacting regime, $V \gg J$.

4.2. Interaction-induced localization

In this section we briefly review the results of Ref. [166], where the localization properties and dynamics of the nearest-neighbor model were first discussed in detail as a function of the disorder W and the nearest-neighbor interactions V. In that work, the localization properties were determined by considering the level-spacing statistics (Sec. 2.3) of the whole spectrum, performing an infinite temperature analysis. The phase boundary may be determined performing finite-size scaling, looking for a fixed point independent of the system size. The determination of the actual phase boundary is, however, typically compromised (as discussed in Ref. [166]) due to the very limited available system sizes, and the consequent uncertainty associated to the extrapolation procedure into the

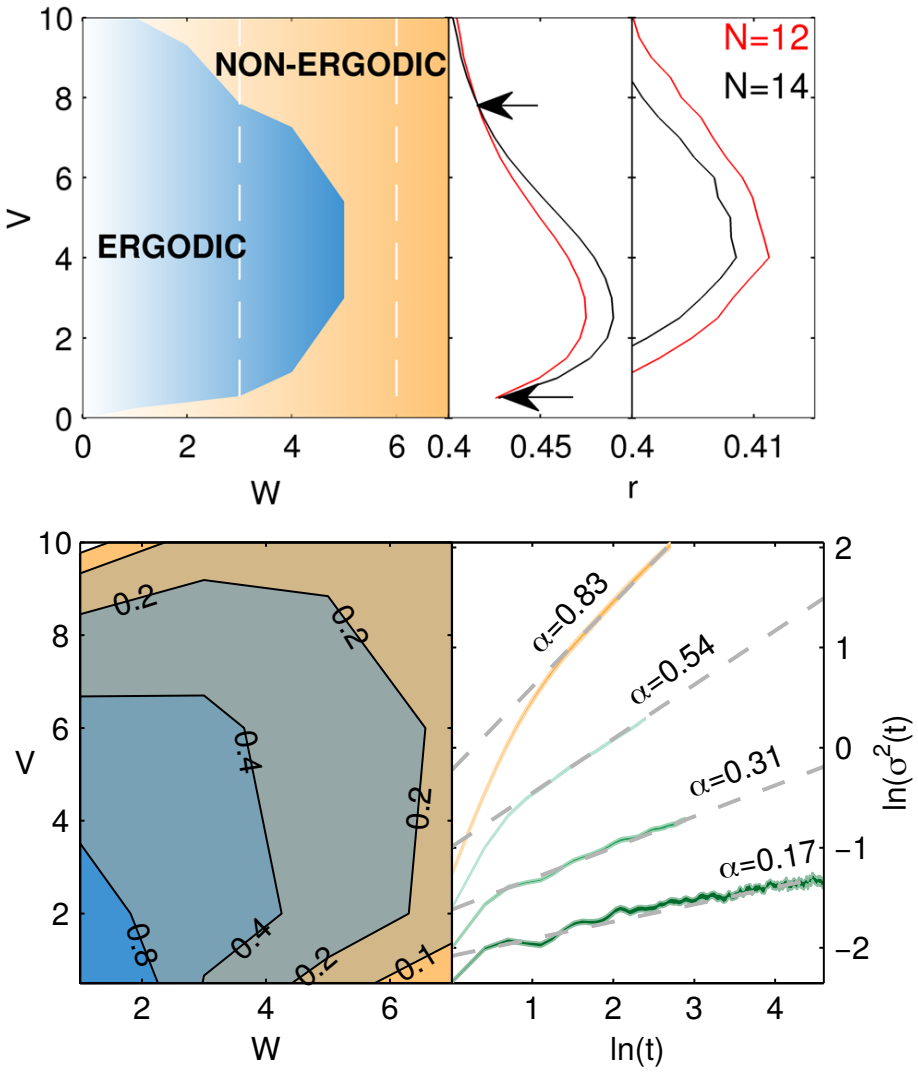

Figure 4.1: (Top left) Approximate dynamical phase diagram of the disordered nearest-neighbor model obtained at infinite temperature as a function of the disorder strength W and the intersite interaction V (here $J = 1$). The phase diagram was evaluated using the level statistics (see Sec. 2.3). (Top right) Determination of the phase diagram based on the mean two-level-ratio (Eq. (2.26)) of two system sizes, $L = 12$ and $L = 14$. The phase boundary is determined from the crossing of the curves. (Bottom left) Contour plot of the exponent α (see text). (Bottom right) Determination of $\alpha(t)$ from the density-density correlation (given by the slope of the dashed lines). The curves are calculated for $V = 2$ and $W = 1.2, 3, 5, 7$ (from top to bottom). L is 24 for the top and 14 for the rest. Figures from Ref. [166].

thermodynamic limit.

Figure 4.1 (upper panel) shows the resulting phase diagram obtained in Ref. [166]. Note the re-entrant character of the MBL phase. This re-entrance was overlooked in previous studies, which were interested either in a single constant interaction cut through

the diagram [142, 143] or in the weakly-interacting regime [176], even though a suggestion that re-entrance could occur in MBL systems was put forward in Ref. [177]. The re-entrant behavior indicates that sufficiently strong interactions can enhance rather than destroy localization.

In Ref. [166] the authors also studied the dynamics across the phase diagram. For this purpose they evaluated after exciting the system at one boundary (using open boundary conditions) the time-dependent density-density correlation at infinite temperature, $C_{ij}(t) = \frac{1}{Z}\mathrm{Tr}[\delta\hat{n}_i(t)\delta\hat{n}_j(0)]$, where $\delta\hat{n}_i = \hat{n}_i - 1/2$, and Z is the dimension of the overall Hilbert space. The spreading of correlations is characterized by

$$\sigma^2(t) = \sum_{n=0}^{L-1} n^2 \left[C_{n0}(t) - C_{n0}(0)\right], \tag{4.2}$$

which acts analogously the mean square displacement of a diffusing particle. The nature of the transport was determined from the dynamical exponent,

$$\alpha(t) = \frac{d\ln\sigma^2(t)}{d\ln t}. \tag{4.3}$$

Note that $\alpha(t\to\infty) = 2$ for ballistic transport and $\alpha(t\to\infty) = 1$ for diffusive transport.

Figure 4.1 (lower panel) shows the asymptotic value of α for different points in the (W, V) plane. For the many-body localization transition scenario, the ergodic phase is advocated to be diffusive, i.e., $\alpha = 1$, while the non-ergodic phase is insulating and should correspond to $\alpha = 0$ [88]. However, the dynamical phase diagram of Fig. 4.1 (lower panel) has a vanishingly small part with α close to one. This region corresponds to the weak localization regime, where the non-interacting localization length is larger than the size of the simulated system. It seems that transport is sub-diffusive throughout the entire phase diagram, and α varies continuously across the ergodic-nonergodic transition. One should note, however, that the methodology is limited by the rather small system sizes and the finite accessible times, and hence there is a lack of a reliable asymptotic $\alpha(t\to\infty)$. Interestingly, the contours of equal α exhibit a similar re-entrant behavior as that of the phase diagram obtained from the level statistics. By studying larger systems using t-DMRG, the re-entrant behavior is found to be not influenced by the system size, and it is thus expected to survive to the thermodynamic limit.

4.3. Hilbert-space fragmentation

The re-entrant shape of the dynamical phase diagram of Fig. 4.1 (top left panel) could leave the wrong impression that for large V many-body localization extends all the way to zero disorder, in other words, disorder-free localization is possible in the nearest-neighbor model. This is however not the case, as we discuss in detail in this section and in the next ones, where we build heavily on previous literature, and in particular on Ref. [167]. We first consider the case of clean lattices, i.e., $W = 0$. For $V/J \gg 1$, energy conservation demands the conservation of the number of nearest-neighbor links. The Hilbert space then fragments into unconnected blocks of states. In the following, we study this fragmentation in detail.

Considering open boundary conditions, the eigenstates of the Hamiltonian of Eq. (4.1) present a defined parity due to the reflection symmetry. We obtain the eigenenergies by exact diagonalization in the even or odd parity sector (both sectors provide equal results). The density of states (DOS) around a given energy E_α is given by

$$\mathrm{DOS}(\epsilon_\alpha) = \frac{\sum_\beta e^{-\frac{1}{2}\left(\frac{\epsilon_\beta - \epsilon_\alpha}{\sigma}\right)^2}}{\sum_\beta e^{-\frac{1}{2}\left(\frac{\beta/\Omega - \epsilon_\alpha}{\sigma}\right)^2}}, \tag{4.4}$$

where $\epsilon_\alpha = (E_\alpha - E_{min})/(E_{max} - E_{min})$ is the normalized energy, with E_{max} (E_{min}) the maximal (minimal) energy, and $\sigma = \Delta E/(E_{max} - E_{min})$ is a small value running from $10/\Omega$ to $100/\Omega$, with Ω the dimension of Hilbert space. Figure 4.2 (a) shows, for small V, that the DOS is a smooth function of the energy eigenvalues. In contrast, Fig. 4.2 (b) shows that for a sufficiently large V the DOS splits into N separate fragments.

The number of nearest-neighbor links is given by the operator

$$\hat{l} = \sum_{j=1}^{L-1} \hat{n}_j \hat{n}_{j+1}, \tag{4.5}$$

whereas the number of singlons is provided by

$$\begin{aligned} \hat{N}_s = &\sum_{j=2}^{L-1} \underbrace{(1-\hat{n}_{j-1})\,\hat{n}_j\,(1-\hat{n}_{j+1})}_{\circ\bullet\circ} + \sum_{j=2}^{L-1} \underbrace{\hat{n}_{j-1}\,(1-\hat{n}_j)\,\hat{n}_{j+1}}_{\bullet\circ\bullet} \\ &+ \underbrace{\hat{n}_1\,(1-\hat{n}_2)\,(1-\hat{n}_3)}_{|\bullet\circ\circ} + \underbrace{\hat{n}_L\,(1-\hat{n}_{L-1})\,(1-\hat{n}_{L-2})}_{\circ\circ\bullet|}. \end{aligned} \tag{4.6}$$

The first term of Eq. (4.6) describes ordinary un-bound singlons. The second term is

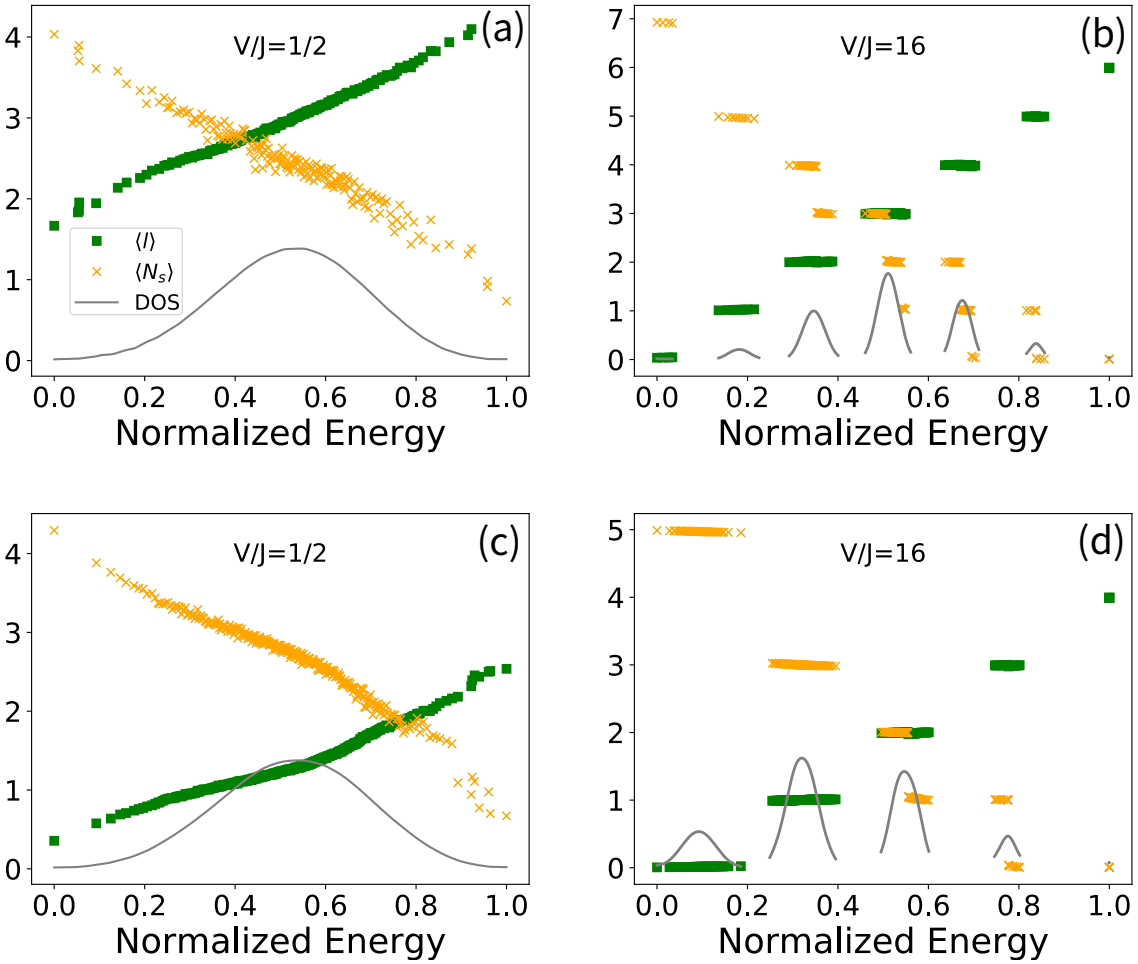

Figure 4.2: (a) Density of states (DOS) (grey solid curves) for the eigenspectrum of Hamiltonian Eq. (4.1) with $W = 0$, $N/L = 7/14$, and a small $V/J = 0.5$. The data is obtained from the odd parity states. In the figure we depict as well $\langle \hat{l} \rangle$ (green squares), and $\langle \hat{N}_s \rangle$ (orange crosses). (b) Same as (a) but with a larger $V/J = 16$. (c) Same as (a) but for $N/L = 5/15$, here the data is obtained from the even parity states. (d) Same as (c) but with $V/J = 16$.

related to the fact that a singlon can freely pass through a domain of particle chain by injecting a single hole into the it (see Fig. 4.5 (a) below in this chapter), and hence a singlon is either an un-bound particle or an un-bound hole. Double counting among the first and the second term should be prevented. The last two terms exist for open boundary conditions. Figures 4.2 (a) and (c) show that when the DOS displays a smooth function, the values of $\langle \hat{l} \rangle$ and $\langle \hat{N}_s \rangle$ also spread continuously in the middle of the spectrum. In contrast, as presented in Figs. 4.2 (b) and (d), when the DOS is fragmented by large-enough interactions, $\langle \hat{l} \rangle$ acquires only integer values $0 < l < N - 1$. Moreover, within a fragment with a given l, there are separated sub-fragments characterized by a fixed

integer number of singlons $N_s^{min} \leq \langle N_s \rangle \leq N_s^{max}$, with $N_s^{max} = N - l - \text{ceil}\,(l/N)$, and $N_s^{min} = \max\{0, N - 2l\}$. Note that in order to better visualize the Hilbert space fragmentation, we rearrange the eigenstates $|\alpha\rangle$ according to a growing value of $x_\alpha \equiv (N+1)(N-1-\langle \hat{l} \rangle_\alpha) + \langle \hat{N}_s \rangle_\alpha$.

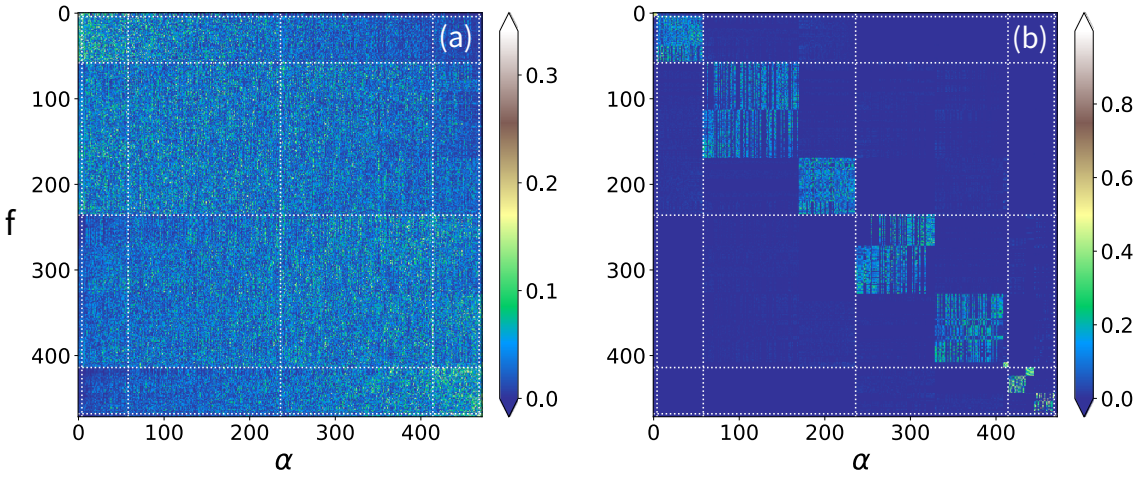

Figure 4.3: Plot of the amplitude $|\psi_\alpha(f)|$ of the eigenstates $|\alpha\rangle$. in the Fock basis $|f\rangle$. The results correspond to the eigenstates of Hamiltonian (4.1) with $W = 0$, $V/J = 1/2$ (a), and $V/J = 16$ (b). The data refers to the even-parity states with filling factor $N/L = 6/12$. Different filling and parity do not change the box-diagonal nature of the structure when V/J is sufficiently large.

The fragmentation becomes immediately apparent in Fig. 4.3. For a given eigenstate $|\psi_\alpha\rangle = \sum_f \psi_\alpha(f)|f\rangle$, with $|f\rangle$ the Fock-state basis, we depict $|\psi_\alpha(f)|$. Arranging the eigenstates in the way mentioned above, one can immediately observe the emergence of a box-diagonal structure for large-enough V/J, and how this fragmentation is absent when V/J is small. This block-like structure has important consequences for the dynamics, it means that a given initial Fock state can only connect with a limited number of other Fock states, for $V/J \gg 1$, this is true at infinite time, since it is a property of eigenstates. Particle motion is hence severely constrained by the conservation of both $\langle \hat{l} \rangle$ and $\langle \hat{N}_s \rangle$. As shown in later sections, resonant spatial delocalization remains however in general possible in the nearest-neighbor model. As discussed in the next chapter, the situation is markedly different in polar lattice gases.

4.4. Eigenstate entanglement entropy

In this section we discuss the eigenstate entanglement entropy, which provides a good quantitative characterization of the Hilbert-space fragmentation resulting from large-enough nearest-neighbor interactions. Splitting the system into two sub-systems A and B, we introduce the reduced density matrix ρ^A of sub-system A. In the Schmidt basis $|A_a\rangle \otimes |B_b\rangle \equiv |a,b\rangle$,

$$\begin{aligned} \rho^A &= \mathrm{Tr}_B |\Psi\rangle\langle\Psi| \\ &= \sum_{a,a'} \sum_b \langle a,b|\Psi\rangle\langle\Psi|a',b\rangle \cdot |a\rangle\langle a'|. \end{aligned} \tag{4.7}$$

We may then define the von Neumann entropy (entanglement entropy) as

$$S_{vN} = -\sum_a \varrho_a \ln \varrho_a \tag{4.8}$$

with $\{\varrho_a\}$ being the eigenvalues of ρ^A. Since $\sum_b \langle a,b|\Psi\rangle\langle\Psi|a',b\rangle$ in Eq. (4.7) is only non-zero when the sub-basis $|a\rangle$ and $|a'\rangle$ have the same number of particles, in the Fock basis representation, ρ^A can be written as the sum of blocks with a defined particle number,

$$\rho^A = \rho^A_{n=0} \oplus \rho^A_{n=1} \oplus \cdots \oplus \rho^A_{n=N}. \tag{4.9}$$

Note that these blocks are inherent to any reduced density matrix of any number-conserving model, and have nothing to do with the interaction-induced Hilbert-space fragmentation discussed in this chapter. Equation (4.8) can then be written as

$$S_{vN} = -\sum_{n=0}^{N} \sum_a \varrho^n_a \ln \varrho^n_a. \tag{4.10}$$

Defining $p_n = \sum_a \varrho^n_a$, and $\lambda^n_a = \varrho^n_a / p_n$, such that $\varrho^n_a = p_n \lambda^n_a$ and $\sum_a \lambda^n_a = 1$, Eq. (4.10) becomes

$$S_{vN} = \underbrace{-\sum_{n=0}^{N} p_n \ln p_n}_{S_n} \underbrace{-\sum_{n=0}^{N} p_n \sum_a \lambda^n_a \ln \lambda^n_a}_{S_c}. \tag{4.11}$$

The first term S_n is the *number entropy* resulting from the superposition of states with different particle numbers in A, and is exactly correlated with B due to the conserved total particle number. As a consequence of the conservation of the total particle number, S_n is non-zero in the presence of any finite tunneling between sub-systems A and B. The

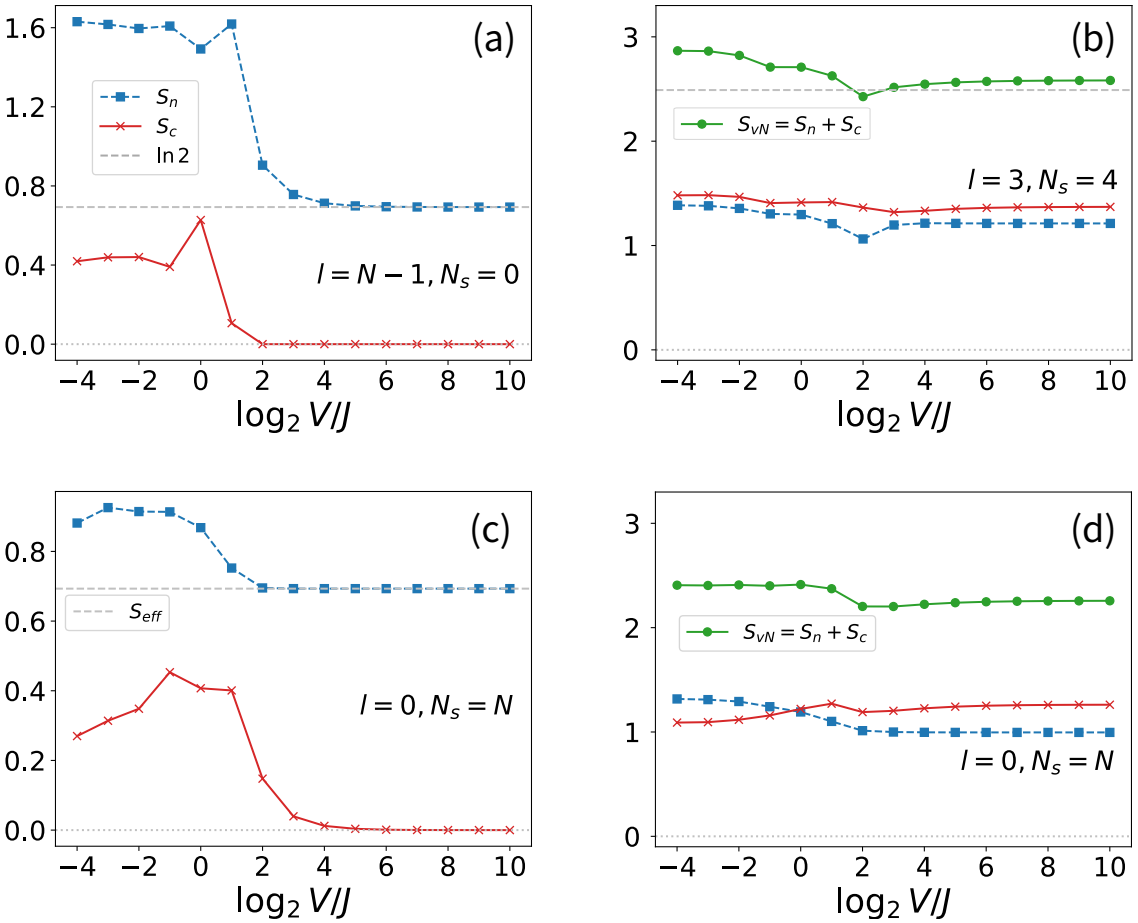

Figure 4.4: (a) Number entropy, S_n, and configurational entropy, S_c, as a function of V for Eq. (4.1) with $W = 0$ and $N/L = 7/14$. The data are averaged over selected eigenstates that have $\langle \hat{l} \rangle \to N-1$ and $\langle \hat{N}_s \rangle \to 0$ when $V \to \infty$. (b) Similar to (a) but with $N/L = 8/16$ and the eigenstates are selected by $\langle \hat{l} \rangle \to 3$, $\langle \hat{N}_s \rangle \to 3$. (c) Similar to (a) but the eigenstates are selected by $\langle \hat{l} \rangle \to 0$, $\langle \hat{N}_s \rangle \to N$. (d) Similar to (c) but with $N/L = 6/18$.

second term S_c is the *configurational entropy* resulting from the superposition of states with different configurations of n particles in sub-system A. This entropy results from correlations between different configurations in sub-systems A and B.

In our numerics, we take A (B) to be the left (right) half of the lattice. The values of S_n and S_c are calculated and averaged in a block, characterized by those eigenstates in which $\langle \hat{l} \rangle$ approaches to a given l, and $\langle \hat{N}_s \rangle$ to a given N_s when $V/J \to \infty$.

Figure 4.4 (a) shows the averaged S_n and S_c for states with $l = N-1$ and $N_s = 0$. When V/J increases, the eigenstate approaches a stable N-string distribution (a chain in which all particles occupied consecutive sites), where the configuration becomes fixed, and thus $S_c \to 0$. Note that for open-boundary conditions, the reflection symmetry lets any

eigenstate spreads at least over two symmetric Fock states. As a result, S_n approaches $\ln 2$ for sufficiently large V/J.

The case with $l = 3$ and $N_s = 3$ is depicted in Fig. 4.4 (b). Due to the larger number of possible states, the configurational entropy is significantly larger, with $S_c > S_n$. The von Neumann entropy ($S_n + S_c$) saturates at a value ~ 2.5. An estimation obtained considering the eigenstates of a toy model consisting of N_s well separated particles in $L-2$ sites gives a slightly lower value (dashed line).

Figure 4.4 (c) and (d) show the case of $l = 0$ and $N_s = N$. For large $V/J \gg 1$, these eigenstates approach states where no particle has nearest neighbors, i.e., a singlon gas. For a half-filled system (Fig. 4.4 (c)), $S_c \to 0$ since the configuration reduces to a fixed density wave state, i.e., $|\cdots \bullet \circ \bullet \circ \cdots\rangle$. However, for open boundary conditions, dynamics results from the motion of a holon dimer (two neighboring empty sites), which acts as an effective particle that may move from right to left, even for $V/J \to \infty$, following a series of resonant hops:

$$|\bullet \circ \bullet \circ \cdots \bullet \circ \bullet \circ\rangle \to |\bullet \circ \bullet \circ \cdots \bullet \circ \circ \bullet\rangle \to \cdots$$
$$\cdots \to |\bullet \circ \circ \bullet \cdots \circ \bullet \circ \bullet\rangle \to |\circ \bullet \circ \bullet \cdots \circ \bullet \circ \bullet\rangle.$$

Since such an effective particle is either in the left or the right half of the system, the above-mentioned motion only contributes to the number entropy. The corresponding eigenstates are the Bloch states $|\alpha_{\text{eff}}\rangle$ of the effective particle. By constructing $\rho^A_{\text{eff}} = \text{Tr}_B |\alpha_{\text{eff}}\rangle\langle\alpha_{\text{eff}}|$, one obtains the entanglement entropy S_{eff}, such that when V/J increases S_n approaches S_{eff}, as depicted in Fig. 4.4 (c). The situation changes at a lower filling, as depicted for a 1/3 filling in Fig. 4.4 (d). The larger number of empty sites significantly increases the allowed configurations and breaks the effective particle picture. Correlations among the larger number of many-body states increases both S_n and S_c. Interestingly, while the overall entanglement entropy decreases, the S_c slightly increases and exceeds S_n for $V/J \to \infty$.

In general, Figs. 4.4 show that the eigenstate entanglement entropy saturates when V/J increases due to the emerging conservation of both l and N_s.

4.5. Many-body localization in the strong coupling limit

As previously mentioned, in the nearest-neighbor model, Hilbert space fragmentation does not lead to disorder-free many-body localization for general states. In order to clarify

this crucial point, we employ the discussion of Ref. [167], which analyzed fragmentation and localization in the nearest-neighbor model in the presence of on-site disorder.

4.5.1. Infinitely large interaction

As in Ref. [167], we focus at this point on the limit $V/J \to \infty$. As previously discussed, see Fig. 4.2, in the strongly-interacting regime the density of states splits into bands composed by states with an equal number of nearest-neighbor links (Eq. (4.5)). Projecting the Hamiltonian (4.1) into each one of these bands we obtain the following effective Hamiltonian to first order in perturbation theory,

$$H_\infty = -J \sum_j \mathrm{P}_j \left(\hat{a}_{j+1}^\dagger \hat{a}_j + H.c. \right) \mathrm{P}_j + W \sum_j h_j \hat{n}_j, \tag{4.12}$$

with the local projector $\mathrm{P}_j = \mathbb{I} - (\hat{n}_{j+2} - \hat{n}_{j-1})^2$, and $\mathrm{P}_j^2 = \mathrm{P}_j$. The number of nearest-neighbor links, $N_{\bullet\bullet}$, is conserved, i.e., $[H_\infty, N_{\bullet\bullet}] = 0$, by construction.

The conservation of $N_{\bullet\bullet}$ strongly constraints the dynamics, since a particle at site j can hop only when $\hat{n}_{j+2} = \hat{n}_{j-1}$. Hence, whereas singlons are free to move, a string of consecutive neighboring particles remains in principle stuck due to the conservation of the number of nearest-neighbor links. However, as illustrated in Fig. 4.5 (upper left), if a singlon approaches a string, it can assist the resonant hop of a string particle, triggering the swap of the positions of the singlon and the string by means of a series of resonant hops. After the swap, the string effectively shifts as a whole by two sites in the opposite direction to the movement of the singlon. This process, which is fully resonant even for $V/J \to \infty$, is basically identical to the Brownian-like motion discussed in Ch. 3.

4.5.2. The theory of movers

We review at this point an useful model introduced in Ref. [178], which permits some crucial insights in the dynamics of the nearest-neighbor model with strong interactions. Considering periodic boundary conditions, H_∞ can be mapped to a spin-1/2 model on the bonds. Two consecutive filled (empty) sites may be identified with a spin up and spin down on the middle bond, i.e.,

$$|\bullet\bullet\rangle \mapsto |\uparrow\rangle$$
$$|\circ\circ\rangle \mapsto |\downarrow\rangle,$$

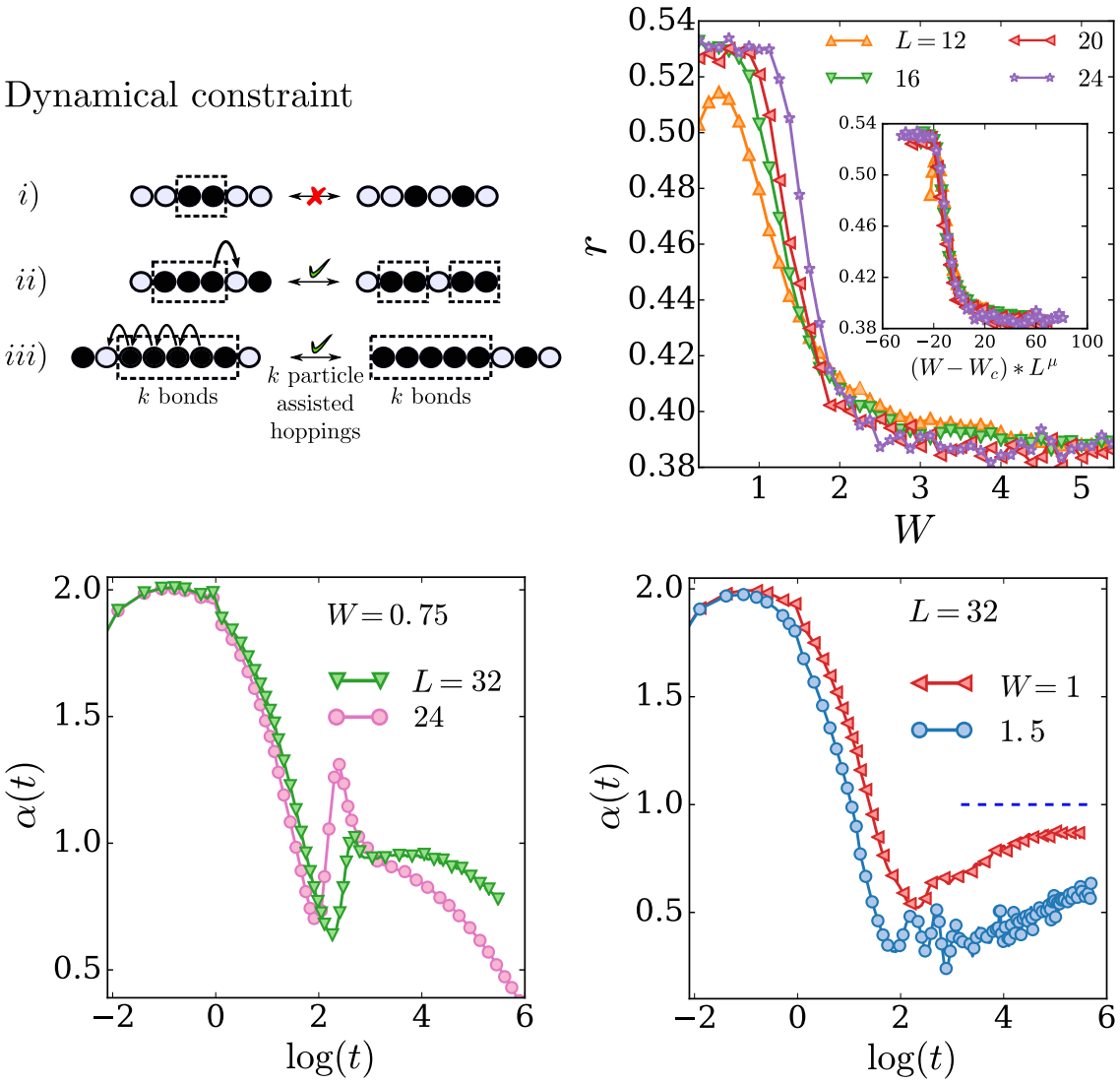

Figure 4.5: (Top left) Dynamical constraint and idea of mover. For large V/J, a string of consecutive neighboring particles cannot split on its own as the number of bonds is conserved. The motion of the string is however possible if a second particle assists the hop, such that $N_{\bullet\bullet}$ stays constant. Particles at the edge of a domain can "pass through" via the very same Brownian-like mechanism discussed in Ch. 3. (Top right) The mean two-level-ratio, r, as a function of W for several system sizes $L \in \{12, 16, 20, 24\}$. The inset shows the finite size scaling, depicting r as a function of the re-scaled variable $(W - W_c)L^\mu$ with $W_c = 2$ and $\mu = 1$. Note that $J = 1/2$ using the convention of Ref. [167], and thus the critical disorder is $Wc/J = 4$ in our convention. (Lower left) Dynamical exponent $\alpha(t)$ at $W = 0.75$, with the enlarging plateau close to the diffusion, $\alpha(t) = 1$, when the system size increases. (Lower right) $\alpha(t)$ for $W = 1$, 1.5 for a fixed system size $L = 32$. In these cases α does not form a plateau at large time; instead it increases and might approach $\alpha = 1$ (dashed line) in the thermodynamic limit. Figures from Ref. [167].

and a mobile particle is mapped to a empty bond, following Ref. [167] we call it a "mover",

$$|\circ\bullet\rangle \mapsto |\mathbf{0}\rangle.$$

The number of movers, $N_{\mathbf{0}}$, the number of spin up and down, $N_{\uparrow}$ and $N_{\downarrow}$, and the number of spin flips (i.e., of "domain walls"), $N_{\uparrow\downarrow}$, are all constants of motion. Furthermore, for half-filled lattices, i.e., $N = L/2$, the number of spins up is always equal to the number of spins down, and hence $N_{\uparrow} + N_{\downarrow} = 2N_{\uparrow} = N$.

The Fock state

$$|\bullet\bullet\circ\circ\bullet\bullet\circ\circ\bullet\bullet\circ\circ\rangle$$

is mapped to the Néel state in the spin configuration

$$|\uparrow\downarrow\uparrow\downarrow\uparrow\downarrow\rangle,$$

which is frozen and characterized by the absence of movers. Indeed, movers are the only delocalized degrees of freedom moving around the effective spin configuration. For example, the Fock state

$$|\bullet\bullet\circ\circ\bullet\bullet\bullet\circ\circ\bullet\circ\circ\rangle$$

is mapped to

$$|\uparrow\downarrow\uparrow\uparrow\downarrow\ \mathbf{0}\ \downarrow\rangle.$$

The dynamics is given by the mover passing through the spin configuration,

$$|\uparrow\downarrow\uparrow\uparrow\downarrow\ \mathbf{0}\ \downarrow\rangle \rightarrow |\uparrow\downarrow\uparrow\uparrow\ \mathbf{0}\ \downarrow\downarrow\rangle.$$

The configuration remains fixed during the dynamics of the movers up to cyclic rotations and thus the number of flips in the spin configuration is a constant of motion. Finally, note that an additional rule is introduced to guarantee the conservation of the number of movers [167]. Once a mover approaches from the left a domain wall constituted by frozen particles, e.g.,

$$|\cdots\circ\bullet\circ\circ\bullet\bullet\circ\circ\cdots\rangle \rightarrow |\cdots\circ\circ\bullet\circ\bullet\bullet\circ\circ\cdots\rangle,$$

a new mover is generated by definition

$$|\cdots\mathbf{0}\downarrow\uparrow\cdots\rangle \rightarrow |\cdots\downarrow\mathbf{00}\uparrow\cdots\rangle.$$

This should be re-normalized as a single mover state $|\cdots\downarrow\mathbf{0}\uparrow\cdots\rangle$.

The idea of mover is crucial, since it permits to easily grasp how resonant motion is possible in the nearest-neighbor model even if V/J tends to infinity, hence precluding disorder-free many-body localization for general states even in the strongly interacting

regime. Note that we insist about the idea of general states with the presence of movers, since specific states, like

$$|\bullet\bullet\circ\circ\bullet\bullet\circ\circ\bullet\bullet\circ\circ\rangle,$$

will localize in the nearest-neighbor model when $V/J \to \infty$.

4.5.3. Finite critical disorder for many-body localization

Reference [167] evaluated by means of the level statistics the MBL properties of H_∞, focusing for a half-filled lattice on the Hilbert-space fragment with $N_{\bullet\bullet} = L/4$ and $N_{\mathbf{0}} = N_{\bullet\bullet} - 1$, which is the block with the largest amount of movers in the largest band for lattices at half-filling. By a finite-size analysis of the two-level ratio (see Sec. 2.3), they determined for those states a finite critical disorder for MBL, $W_c/J \sim 4$, see Fig. 4.5 (upper right). Note that the hopping amplitude considered in that reference as unit is $J/2$, thus with our convention a factor of 2 should be multiplied to the result in the figure of that paper.

For the nearest-neighbor model, and due to the mover idea mentioned above, the finite critical disorder becomes eventually independent of V for a sufficiently large V/J. As $V \to \infty$ the spin configuration (many-particle domains) is strictly maintained, while movers may pass through the configuration. Therefore for an arbitrary initial state, once the density of movers is finite, mover motion leads to resonant delocalization for an arbitrarily large V. Precisely, a mover shifts clusters of any length by two sites every time a singlon passes by (see Fig. 4.5 (upper left)). Since the selected fragment mentioned above is the most mobile one in the largest band, a finite critical disorder can be consider to be a typical property for general cases with finite density of movers. However, there are special states, which are particularly prone to localization. Initial states with no movers are of course intrinsically frozen, with or without disorder, when $V/J \to \infty$. Moreover, those with a single mover are characterized by Anderson localization (in spite of the somewhat correlated effective disorder), and hence the critical W goes to zero for those states [167].

4.5.4. Dynamical exponent

The dynamical exponent, Eq. (4.3), was also calculated in Ref. [167] within the same fragment. To examine the diffusion nature of the ergodic phase, small disorders ($W < W_c$) were considered. Figure 4.5 (lower left) shows $\alpha(t)$ for a disorder $W = 0.75$ and various system sizes L. At short times, α reaches 2, meaning that the dynamics is ballistic due

to universal quantum fluctuations. At intermediate times, α develops a plateau close to the diffusive value 1. The plateau enlarges with increasing system size. This may indicate that in the thermodynamic limit the system is probably diffusive. Figure 4.5 (lower right) shows $\alpha(t)$ for $L = 32$ and various W, again, after the ballistic propagation at short times, $\alpha(t)$ is always bounded by the diffusive value 1, but as time increases, it tends to converge to diffusion. The authors further concluded that the sub-diffusive dynamics found in Ref. [166] might be only a transient behavior.

4.6. Many-body localization in the nearest neighbor model

To study many-body localization for a wide range of V, the full Hamiltonian, Eq. (4.1), should be considered instead of the effective one of Eq. (4.12). Although level statistics is commonly employed, the results are Poissonian (integrable) in both fully delocalized ($W \to 0$) and fully localized ($W \gg J$) regimes. Moreover, the statistics is largely handicapped due to the Hilbert space fragmentation. Note that in the presence of disorder, $W > 0$, localization results in a disorder-induced fragmentation on top of the Hilbert-space blocks of the clean ($W = 0$) nearest-neighbor model. Therefore, we employ in the following the inverse participation ratio to characterize this disorder-induced fragmentation, and hence localization. This analysis will permit us a better comparison with the interaction-induced shattering discussed in the next chapter for the case of a polar lattice gas.

From exact diagonalization we obtain the many-body eigenstates $|\alpha\rangle = \sum_f \langle f|\alpha\rangle |f\rangle$. However, in order to relate more directly with experiments, in which specific Fock states can be realized using quantum microscope techniques, we rather express the Fock states in the basis of eigenstates $|f\rangle = \sum_\alpha \langle \alpha|f\rangle |\alpha\rangle$, and calculate the survival probability at a given time

$$P_f(t) = \sum_{\alpha,\beta} |\langle \alpha|f\rangle|^2 |\langle \beta|f\rangle|^2 \times e^{i(\omega_\alpha - \omega_\beta)t}, \tag{4.13}$$

where $|\alpha\rangle$ and $|\beta\rangle$ are eigenstates. For asymptotically long times, the survival probability approaches $P_f(t \to \infty) = \mathrm{IPR}_f$, with

$$\mathrm{IPR}_f \equiv \sum_\alpha |\langle f|\alpha\rangle|^4, \tag{4.14}$$

the inverse participation ratio of the Fock state $|f\rangle$ in the eigenstate basis. We will employ below IPR_f as our observable for the study of fragmentation and localization.

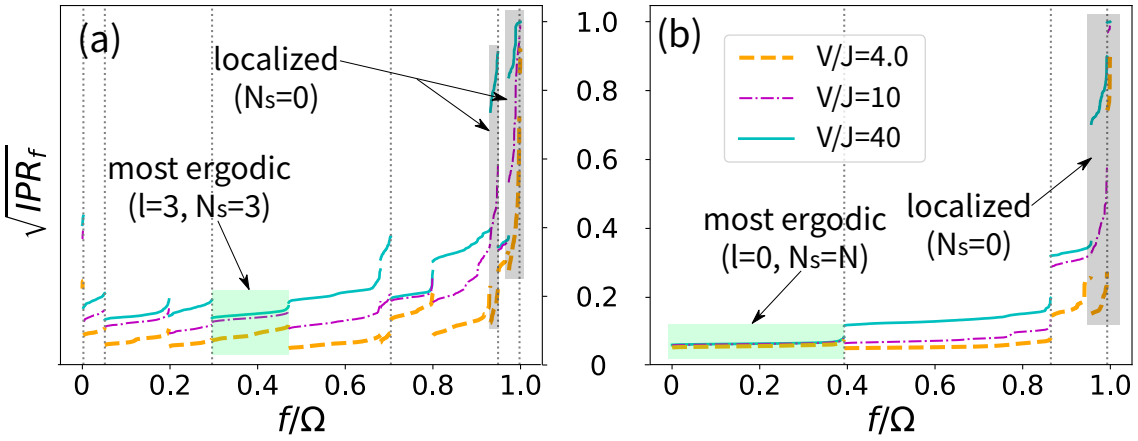

Figure 4.6: (a) $\sqrt{\mathrm{IPR}_f}$ obtained from Eq. (4.1), with $N/L = 7/14$, and $W/J = 0.25$. The Fock states $|f\rangle$ are ordered according to l and N_s. For large V/J, the fragments with $N_s = 0$ and with the lowest-IPR_f are depicted using gray and green shades, respectively. (b) Same as (a) but with $N/L = 4/16$. Open boundary conditions are taken in all cases.

In Fig. 4.6 we depict IPR_f for all Fock states for $N/L = 7/14$ and $N/L = 4/16$ for a weak disorder $W/J = 0.25$. We see clearly that the different fragments are characterized by a relatively narrow window of values of IPR_f. In the absence of singlons, $N_s = 0$, a large-enough V significantly increases the IPR_f due to the very poor mobility of strings of consecutive neighboring particles. In contrast, the dynamics in fragments with $N_s \neq 0$ results for sufficiently large V/J from the mover idea discussed in Sec. 4.5.2. The mobility, and eventual delocalization-to-localization transition, in those fragments only depends on the singlon density and the disorder strength.

In order to analyze the disorder-induced localization, we compare for a given Fock state $|f\rangle$ the inverse participation ratio IPR_f with the effective Hilbert space dimension, Λ_f, relevant for $|f\rangle$ in the clean nearest-neighbor model. Strong localization is characterized by $\mathrm{IPR}_f \sim \mathcal{O}(1)$, while a delocalized state presents $\mathrm{IPR}_f \sim \mathcal{O}(\Lambda_f^{-1})$. For large-enough $V/J > 10$, the clean nearest-neighbor model fragments into separate Hilbert-space blocks with fixed l and N_s, and Λ_f is then given by the fragment size. For $4 \lesssim V/J \lesssim 10$, fragments with fixed number of nearest-neighbor links, l, start to develop, but the sub-structures of N_s are not yet fully formed, we hence choose Λ_f as the size of the blocks with a given l. For $V/J \lesssim 4$, no fragmentation occurs in the clean model, and hence we choose Λ_f as the dimension of the whole Hilbert space. We analyze the disorder-induced (and in the next chapter interaction-induced) fragmentation of the blocks of the clean

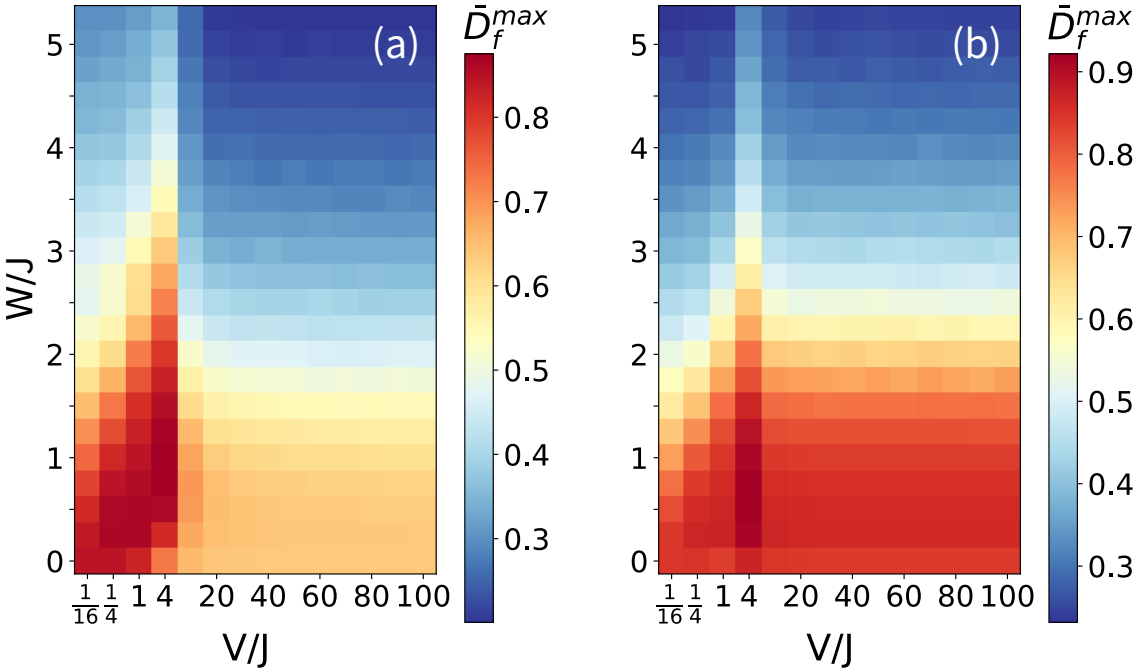

Figure 4.7: Localization in the nearest-neighbor model. $\bar{D}_f^{max}$ as a function of V/J and W/J for $N/L = 8/16$ (a), and $N/L = 5/20$ (b). Blue regions are parameter regimes where MBL is expected. Note both the re-entrant shape at low V/J, and the presence of a finite critical W_c for MBL even for $V \to \infty$. The results are obtained after averaging over 1000 disorder samples. Open boundary conditions are taken in all cases.

nearest-neighbor model by introducing the fractal dimension [179, 180],

$$D_f = -\ln(\mathrm{IPR}_f)/\ln(\Lambda_f), \tag{4.15}$$

such that $D_f \to 0$ implies localization and $D_f \to \mathcal{O}(1)$ delocalization.

Localization as a function of disorder vary from block to block (and even within the same block [167]). For a given V one determines for each fragment the average $\bar{D}_f$, and finds the fragment with the largest fractal dimension $\bar{D}_f^{max}$ (green areas in Fig 4.6). For low filling ($\rho < 1/2$), $\bar{D}_f^{max}$ naturally corresponds to the fragment with $l = 0$. Note that when $\bar{D}_f^{max} \sim 0$ the whole spectrum localizes. Figure 4.7 shows $\bar{D}_f^{max}$ for a half-filled and a quarter-filled nearest-neighbor model. Note that the abrupt change at $V/J \simeq 10$ for $\rho = 1/2$ is due to the reduction of the size Λ_f of the fragment with maximal $\bar{D}_f$. For $\rho = 1/4$ this does not happen because the fragment of maximal $\bar{D}_f$ is always the $l = 0$ fragment that does not change its size. For $V \to 0$, the system undergoes Anderson localization at vanishingly small disorder [137, 181].

For growing V/J, the region of delocalized states grows up to a maximum and then

decreases due to the reduced cluster mobility, resulting in a re-entrant shape, in good agreement with the results of Ref. [166], discussed in Sec. 4.2. However, disorder-induced fragmentation of the nearesr-neighbor blocks does require a finite disorder strength even at $V = \infty$, due to the in-block resonant motion discussed in Sec. 4.5.2. Our results are in good agreement with the study based on level statistics [167], more details on the localization transition are provided in Appendix B.

4.7. Conclusions

In this chapter we have discussed the case of disordered hard-core extended Hubbard models with only nearest-neighbor interactions. In the nearest-neighbor model, for large-enough interactions the conservation of the number of nearest-neighbor links and singlons (movers) results in Hilbert-space fragmentation, which we have studied by monitoring the amplitudes of the eigenstates in the basis of Fock states. However, Hilbert-space fragmentation does not lead to disorder-free localization or even quasi-localization for general eigenstates. General eigenstates with a finite density of singlons are characterized by resonant delocalization even for infinitely large interactions.

We have presented results based on the analysis of the inverse participation ratio of Fock states, which allow us to study the localization-induced fragmentation of the Hilbert-space blocks of the clean nearest-neighbor model. The results are in good agreement with previous results based on spectral properties. In particular, these results confirm that for the nearest-neighbor model there is always a critical disorder for localization, even for infinitely large V/J. The situation is radically different in polar lattice gases, as discussed in the next chapter.

Chapter 5

Hilbert-space shattering and disorder-free localization in polar lattice gases

This Chapter is devoted to the study of Hilbert-space fragmentation and localization in polar lattice gases. We discuss in detail the particularly relevant role played by the $1/r^3$ tail of the dipole-dipole interactions, which for growing dipole strengths induces not only the conservation of the number of nearest-neighbor links (as shown in the previous chapter) but also additional dynamical constraints.

Our study of the inverse participation ratio of Fock states as a function of disorder and dipole strength, shows that for half-filled lattices it suffices one further emerging conservation law, that of the occupied next-to-nearest neighbor bonds, to induce the shattering of the Hilbert-space blocks of the nearest-neighbor model. Crucially, in contrast to the nearest-neighbor model, this strong fragmentation leads to a significant slow-down of the lattice dynamics, and eventually to disorder-free quasi-localization. The latter occurs because in contrast to the nearest-neighbor model, where motion within a typical Hilbert-space fragment (with a finite density of movers, see Sec. 4.5.2) is resonant, in polar lattice gases the in-block motion is typically non-resonant. This leads to a dramatically slower, quasi-localized, dynamics, since eventual delocalization in a given Hilbert-space block can just occur in high-order in perturbation theory, as a result of virtual excursions between different Hilbert-space blocks.

We discuss at the end of this chapter the quasi-localization and the eventual delocalization, showing that the latter occurs in a time scale that grows exponentially with the ratio V/J and with the system size. Furthermore, we show that an vanishingly small disorder is able to annihilate the high-order processes, and the eventual delocalization as

well. The results discussed in this chapter show that disorder-free localization results for a critical dipole strength within reach of future experiments in polar lattice gases.

The results of this Chapter (together with a part of the results of the previous chapter) have been reported in Ref. [182].

5.1. Polar lattice gases

We consider in the following hard-core dipolar bosons in one-dimensional optical lattices, whose physics is governed by the disordered extended Bose-Hubbard model model:

$$H = -J\sum_j \left(\hat{a}^\dagger_{j+1}\hat{a}_j + H.c.\right) + \frac{V}{2}\sum_{i\neq j}\frac{1}{|i-j|^3}\hat{n}_i\hat{n}_j + W\sum_j h_j\hat{n}_j, \tag{5.1}$$

where we follow the same notation as in previous chapters. Whereas for small V/J this model may be approximated by the nearest-neighbor model discussed in Ch. 4, the $1/r^3$ tail of the dipolar interaction cannot be neglected when V/J grows, and indeed, as shown below, the dipolar tail radically changes qualitatively, and not only quantitatively, the dynamical properties of polar lattice gases. We have seen already in Ch. 3 that the dipolar tail may have surprisingly strong effects even for dilute gases due to the clusterization of nearest-neighbor dimers and the formation of self-bound lattice droplets. Here we go beyond that analysis and discuss more general states in the frame based on the Hilbert-space fragmentation, we study in detail the interplay between disorder and dipolar interactions, and show that fragmentation in polar lattice gases is linked to a strong slow-down of the dynamics and eventually to disorder-free localization.

5.2. Hilbert-space shattering

In this section we study the further fragmentation of the blocks of the clean nearest-neighbor model. In contrast to the previous chapter, where further fragmentation of those blocks resulted only from disorder, in a polar gas the tail $1/r^3$ induces an additional fragmentation, and indeed the shattering, of the nearest-neighbor blocks even in the absence of disorder.

5.2.1. Clean polar lattice gases

We start with the interaction-induced Hilbert-space fragmentation in absence of disorder when V/J increases, the analysis here is similar as that introduced in Sec. 4.3.

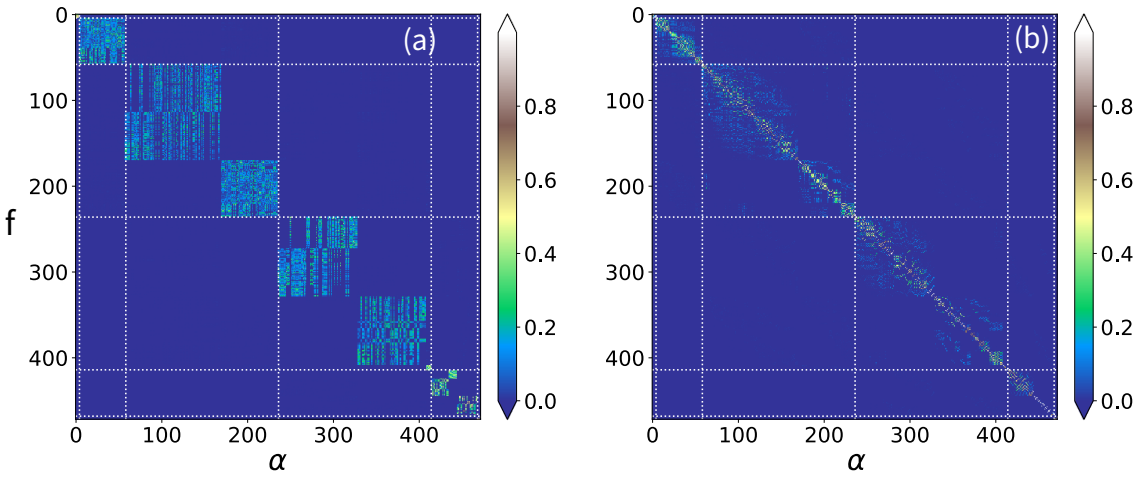

Figure 5.1: (a) Hilbert-space fragmentation in the nearest-neighbor model. Plot of the amplitude $|\psi_\alpha^f|$ of the eigenstates $|\psi_\alpha\rangle$ in the Fock basis $|f\rangle$. The results correspond to the eigenstates of the nearest-neighbor Hamiltonian, Eq. (4.1), with $W = 0$, $V/J = 50$, and $N/L = 6/12$. The data correspond to the even-parity states. (b) Hilbert-space shattering for the polar-lattice Hamiltonian, Eq. (5.1), with the same parameters.

Figure 5.1 shows the amplitudes $|\psi_f(\alpha)|$ of the Fock states $|f\rangle$ in the basis of many-body eigenstates $|\alpha\rangle$ for $N = 6$, $L = 12$, $W = 0$, and $V/J = 50$ for the nearest-neighbor model (a) and the polar lattice gas (b). The eigenstates spread over a very small number of Fock states, or alternatively, the number of Fock states connected (even at infinite time) with a given Fock state is much smaller than that in the nearest-neighbor model. In the figure we have arranged the eigenstates following first a growing order in x_α (see Sec. 4.3). Then within each fragment the states are further ordered following the interaction terms,

$$Q_{DDI} = \sum_{i \neq j} \frac{\langle \hat{n}_i \hat{n}_j \rangle}{|i-j|^3}. \tag{5.2}$$

The comparison between Figs. 5.1(a) and (b) clearly reveals that the tail of the dipole-dipole interaction shatters the block structure of the nearest-neighbor model, leading to a quasi-diagonal structure. Figure 5.1 was obtained using even-parity eigenstates, but similar results are obtained for odd-parity states (and different filling factors as well).

Hilbert-space shattering results directly from additional emergent conservation laws induced by the dipolar tail. Whereas in the nearest-neighbor model a growing V/J just reenforces the conservation of nearest-neighbor links, $l = \sum_j \langle n_j n_{j+1} \rangle$ (see Eq. (4.5)), in polar gases it leads to additional constraints, starting with the conservation of the number of next-to-nearest-neighbor links, $l_2 = \sum_j \langle n_j n_{j+2} \rangle$. For $V \to \infty$ it is intuitive that the

conservation of the number of bonds at any distance leads to frozen dynamics even for $W = 0$ for any initial condition (there are however exceptions, as discussed in Sec. 5.4.4). More interesting, however, is that the dipolar interactions induce disorder-free quasi-localization for values of V/J well within experimental reach. As shown in Figs. 5.1(b) the blocks of the clean nearest-neighbor model are clearly shattered for a half-filled polar gas with $V/J = 50$. Note that for $V/J = 50$, interactions beyond next-to-nearest neighbor are smaller than the bandwidth, $4t$, and hence, for half-filling the shattering of the nearest-neighbor blocks results from the mere additional emerging conservation of l_2.

Similar to the case of disordered nearest-neighbor model, we may quantify the shattering of the nearest-neighbor blocks by means of the evaluation of the fractal dimension D_f for the different Fock states, obtained again by comparing IPR_f with the size of the block evaluated for the clean nearest-neighbor model. In Fig. 5.2, we depict for a clean polar lattice gas, for different system sizes, the average $\bar{\bar{D}}_f$ evaluated over all Fock basis, which provides a good quantitative estimation of the overall shattering of the nearest-neighbor blocks. The results show that clean polar lattice gases with $V/J \gtrsim 20$ are characterized by a strong shattering of the blocks of the clean nearest-neighbor model.

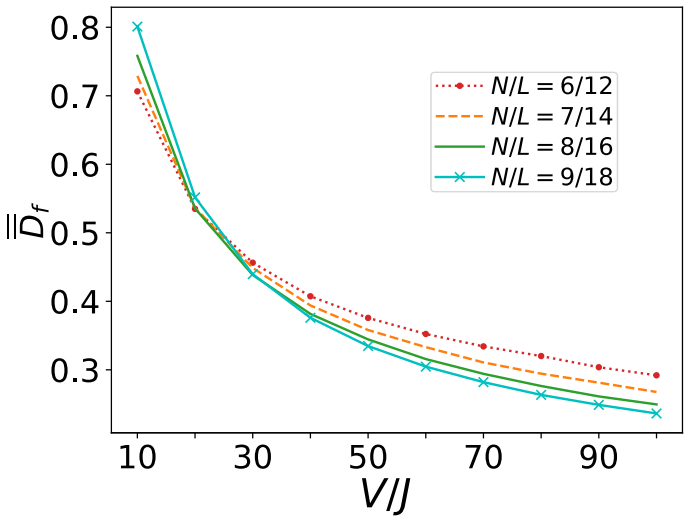

Figure 5.2: Averaged fractal dimension $\bar{\bar{D}}_f$ (see text) as a function of V/J for a half-filled clean polar lattice gas of different system sizes. For $V/J > 20$, $\bar{\bar{D}}_f$ decreases with growing L indicating a more pronounced shattering.

5.2.2. Disordered polar lattice gases

In the presence of disorder, fragmentation of the blocks of the clean nearest-neighbor model results from the combination of the effects of disorder and of the $1/r^3$ tail. As in the previous chapter, we study the Hilbert-space shattering by means of the averaged fractal dimension, obtaining also in this case the maximal averaged $\bar{D}_f^{max}$, which we plot in Fig. 5.3 for a half-filled and a quarter-filled lattice. The results are markedly different compared to the nearest-neighbor model (Fig. 4.7). For large interactions, e.g.,$V/J > 20$ at half-filling, shattering (and, as discussed below, localization) penetrates all the way to vanishingly small disorder.

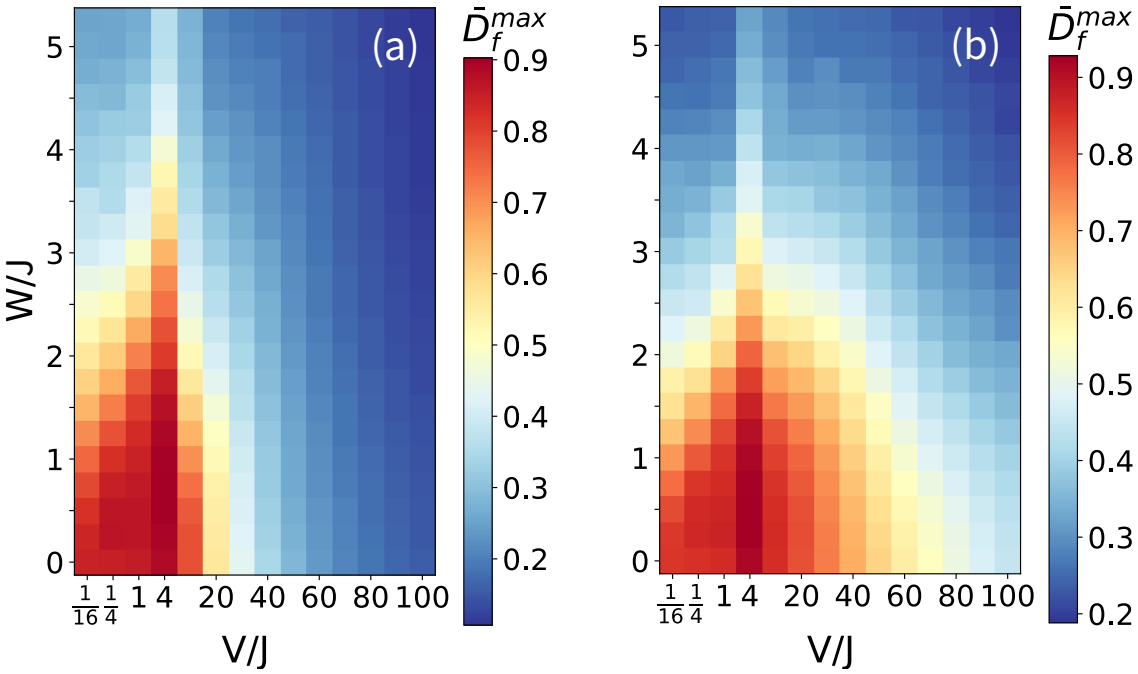

Figure 5.3: Localization in the polar lattice gas. The figures depict, as a function of the disorder W and the dipole strength V, $\bar{D}_f^{max}$ for a polar lattice gas with filling $N/L = 8/16$ (a), and $N/L = 5/20$ (b). Blue regions indicate where strong shattering of the blocks of the clean nearest-neighbor model occurs, and also where localization is expected (see text). Open boundary conditions are taken for all cases.

The crucial difference between the nearest-neighbor model and the polar lattice gas at weak disorder is well illustrated by Fig. 5.4, where we analyze for a very small disorder, $W/J = 0.025$, and different values of V/J the proportion of Fock states with a fractal dimension $D_f < 0.3$. From the results of Fig. 5.2, we see that $\bar{\bar{D}}_f \simeq 0.5$ at the crossing of the curves (for $V/J \simeq 25$), and hence states with $D_f < 0.3$ can be safely considered as

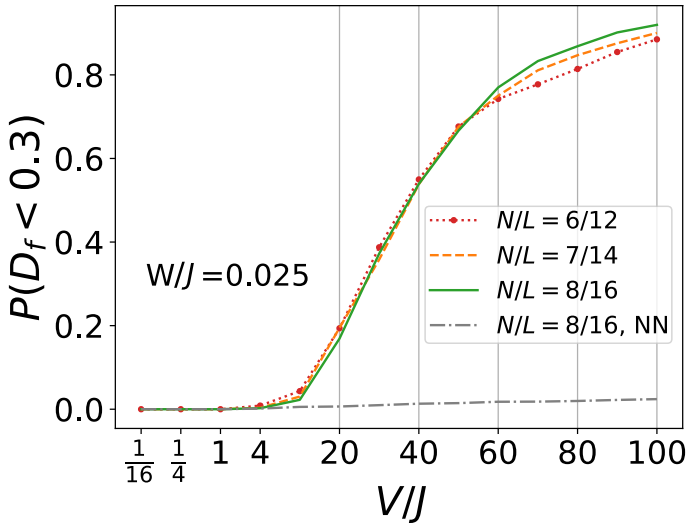

Figure 5.4: Proportion of states with $D_f < 0.3$ for $W/J = 0.025$ (averaged over 1000 realizations) and half-filling, for the nearest-neighbor model with $N = 8$, $L = 16$ and a polar gas with different system sizes.

belonging to strongly fragmented nearest-neighbor blocks. For the nearest-neighbor model, such a small disorder does not lead to any significant further fragmentation, showing that weak disorder does not result in localization even when $V/J \to \infty$. In contrast the dipole-induced shattering of the blocks of the clean nearest-neighbor model is already very strong for $V/J > 20$. As discussed below, shattering is directly linked for general states to a strong slow-down of the dynamics and an eventual localization for a vanishingly small disorder. Therefore, the results of the figure can be also understood as an estimation of the proportion of localized states in the Hilbert space.

Note as well, that the dipole-induced shattering (and hence disorder-free localization) is displaced for quarter-filling to larger V/J compared to the half-filled case. This is not surprising, since in a more dilute lattice interactions between further distant neighbors are needed to induced localization. We should however recall from Ch. 3 that for low densities motion is handicapped by distant particles, since the dipolar tail involving clusters may outcompete the higher-order hopping rate J^m/V^{m-1} of a m-particle cluster. Although, due to the small systems we consider, we cannot provide a detailed analysis of the fractal dimension of low ρ, the results of Ch. 3 on the dynamics of nearest-neighbor dimers suggest that disorder-free localization may be attainable for $V/J \sim 50$ even for $\rho \sim 0.2$.

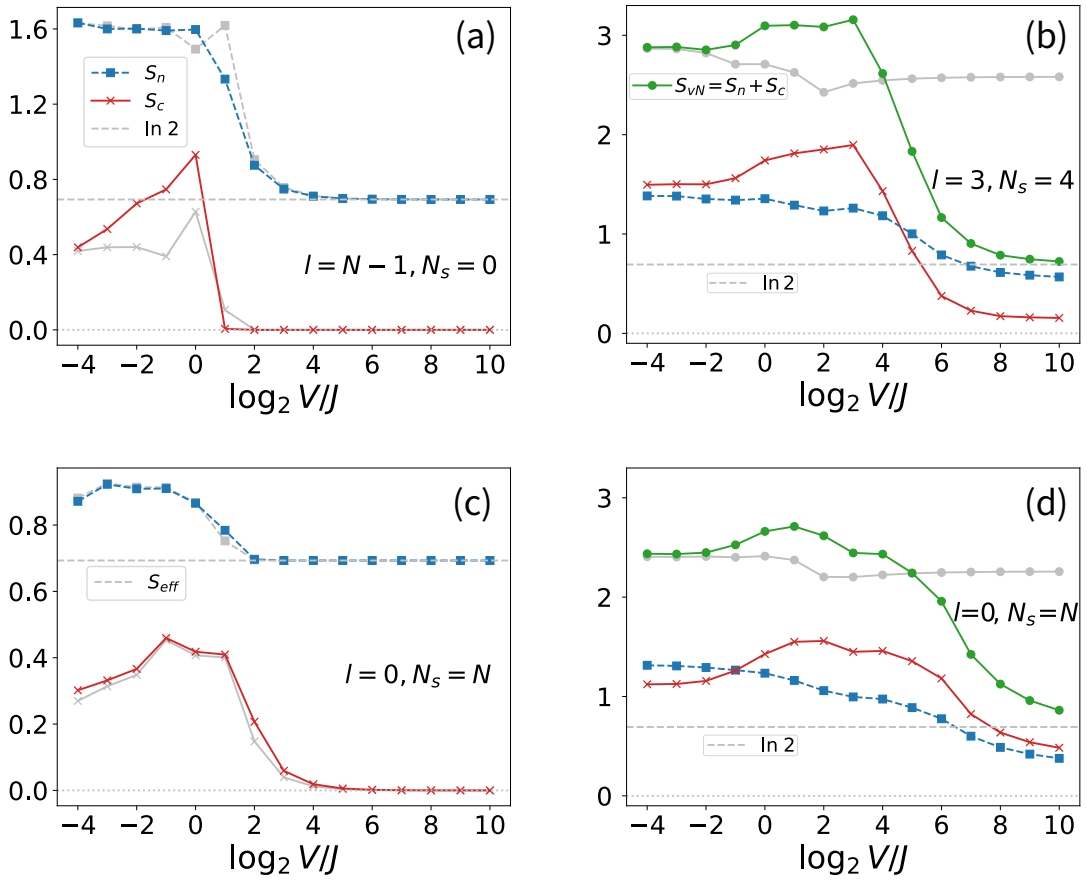

Figure 5.5: Entanglement entropies obtained using the polar lattice gas, Eq. (5.1) (color), and the nearest-neighbor model, Eq. (4.1) (gray). (a) Number entropy S_n and configurational entropy S_c as a function of V for $W = 0$ and $N/L = 7/14$. The data are averaged over selected eigenstates that have $\langle \hat{l} \rangle \to N - 1$ and $\langle \hat{N}_s \rangle \to 0$ when $V/J \to \infty$ (see the main text). (b) Similar to (a) but with $N/L = 8/16$ and the eigenstates are selected by $\langle \hat{l} \rangle \to 3$, $\langle \hat{N}_s \rangle \to 3$. (c) Similar to (a) but the eigenstates are selected by $\langle \hat{l} \rangle \to 0$, $\langle \hat{N}_s \rangle \to N$. (d) Similar to (c) but with $N/L = 6/18$.

5.3. Eigenstate entanglement entropy

The eigenstate entanglement entropy (recall Sec. 4.4) provides also in this case a good quantitative proof of the decrease of particle mobility induced by the additional constraints provided by the dipolar tail. In Figs. 5.5 we compare the entanglement entropies of the nearest-neighbor model, Eq. (4.1), and of the polar lattice gas, Eq. (5.1), for $W = 0$. For weak dipolar interactions, not unexpectedly, the results for the polar gas are basically identical to those of the nearest-neighbor model for every state. This remains so even for large V/J for blocks without singlons (Fig. 5.5 (a)).

The situation changes radically in the presence of singlons. Figure 5.5 (b) shows

the case of states with $l = 3$, and $N_s = 4$. For a sufficiently large $V/J \gtrsim 16$, interactions beyond nearest-neighbors suppress particle configurations available in the nearest-neighbor model, and as a result the configurational entropy S_c decays rapidly, whereas the number entropy S_n reduces correspondingly, and the total entanglement entropy $S_{vN} = S_n + S_c$ reaches ln 2 due to the reflection symmetry of lattices with open boundary conditions (recall Sec. 4.4).

Figure 5.5 (c) shows for half-filling the case of a singlon gas, that is, the case without nearest-neighbor links, whereas the case at third-filling is shown in Fig. 5.5 (d). At half-filling the singlon-gas can be described for sufficiently large V/J by an effective model with a moving holon-dimer, as discussed in Sec. 4.4. The motion of the holon-dimer is resonant and independent of the dipolar tail in the bulk (although it is affected at the boundaries, as discussed in Sec. 5.4.4). As a result the number and configurational entropies are basically the same as in the nearest-neighbor model even for large V/J. For a lower filling, the moving holon-dimer picture breaks down, and the entanglement entropy S_{vN} varies similarly as in Fig. 5.5 (b).

5.4. The dynamics

5.4.1. Non-resonant processes

Whereas nearest-neighbor models are characterized by resonant motion within a Hilbert-space fragment, the emerging conservation of l_2 (and further links) in a polar gas largely prevents resonant dynamics.

As sketched in Fig. 5.6, in the nearest-neighbor model, states in the same block have same conserved values and they can evolve to each other resonantly via the mover motion, but inter-block transitions are forbidden due to the dynamical constraints. In a polar lattice gas, when the Hilbert space shatters, the resonant motions of movers are precluded efficiently by the shattering effects. The typical transition between two states that have same conserved values is not resonant anymore. It will be non-resonant processes that involves intermediate states from different blocks.

In the perturbation point of view:

$$H = \underbrace{-J \sum_j \left(\hat{a}^\dagger_{j+1} \hat{a}_j + \text{H.c.} \right)}_{H_{hop}} + \underbrace{\frac{V}{2} \sum_{i \neq j} |i-j|^{-3} \hat{n}_i \hat{n}_j}_{H_0} .$$

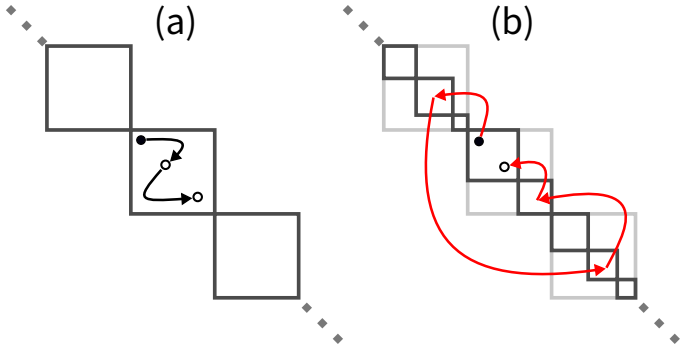

Figure 5.6: Sketch of the difference in the dynamics of the nearest-neighbor model and in the polar lattice gas. (a) In the nearest-neighbor model, the breaking of the Hilbert-space into fragments (boxes) is characterized by the general possibility of resonant motion within a fragment. (b) In a polar lattice gas, the nearest-neighbor blocks shatter into small fragments (dark boxes). In addition, there is no general mechanism for resonant motion within the small fragments, which occurs in general via virtual excursions to other blocks in high-order in perturbation theory in $J/V \ll 1$.

When in $V \gg J$, a responsible non-resonant processes contacting two Fock states that have the same conserved values (number of links at any length, number of movers, domain walls, etc.) will typically involve an amount of single-hopping steps in the order of $\mathcal{O}(N)$. Such a process is in higher-order, and the corresponding transition rates are eventually exponentially small $\sim J/V^{\mathcal{O}(N)}$.

As a result, compared to the nearest-neighbor model, particle dynamics in the polar gas is typically and significantly slowed down for sufficiently large V/J. In the following we discuss the dynamics in the presence of these non-resonant processes.

5.4.2. Long-lived memory of initial conditions

The slow-down dynamics is well illustrated by the evolution of the initial state

$$|\psi(t=0)\rangle = |\circ\circ\bullet\circ\bullet\circ\bullet\bullet\bullet\circ\bullet\circ\bullet\circ\bullet\circ\rangle$$

(other initial states provide in general similar results). We employ exact time evolution of Eq. (5.1) and periodic boundary conditions to remove boundary effects. This initial half-filled state delocalizes in the nearest-neighbor model due to resonant hops, which break the central trimer into two dimers:

$$|\circ\circ\bullet\circ\bullet\circ\bullet\bullet\circ\bullet\bullet\circ\bullet\circ\bullet\circ\rangle$$

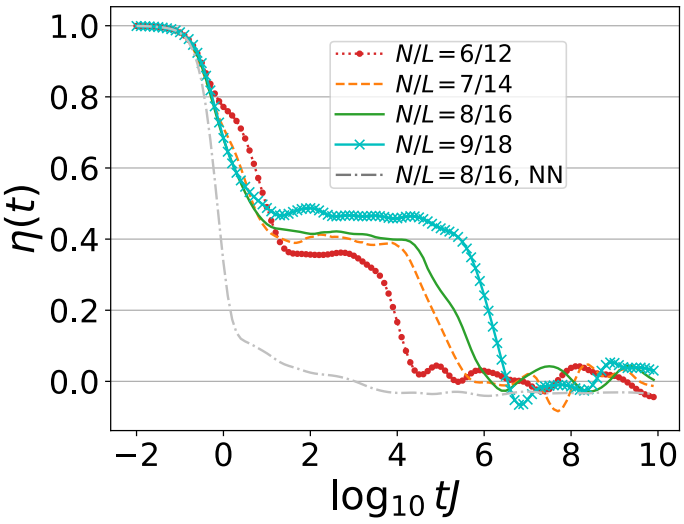

Figure 5.7: Time evolution of the homogeneity $\eta(t)$ for $V/J = 50$ and periodic boundary conditions, for the nearest-neighbor model (with $N/L = 8/16$) and a polar lattice gas (with different system sizes) The initial half-filled state is discussed in the text. In order to compare different system sizes we add or remove pairs $\bullet\circ$ at the right of the state.

and then delocalize each dimer , e.g.,

$$|\circ\circ\bullet\circ\bullet\bullet\circ\bullet\circ\bullet\bullet\circ\bullet\circ\bullet\circ\rangle.$$

All these processes remain resonant in the nearest-neighbor model even for $V = \infty$. In contrast, a sufficiently large dipolar interaction, renders the breaking of the initial trimer non-resonant, since it does not preserve l_2. Moreover, the formation of beyond-nearest-neighbor clusters further hinders the particle dynamics.

Analogous to MBL experiments based on the evolution of density waves [68, 105], and similar to recent trap ion experiments [107], we define the homogeneity parameter as

$$\eta(t) = \frac{N_0(t)/L_0 - N/L}{1 - N/L},$$

where $N_0(t) = \sum_{j\in\{j_0\}}\langle n_j(t)\rangle$ is the number of particles in the set $\{j_0\}$ of L_0 initially occupied sites, and L_0 is nothing but the total particle number N. Homogenization of the on-site populations results in $\eta(t) \to 0$. We depict in Fig. 5.7 $\eta(t)$ for $V/J = 50$. Homogenization is quickly reached for the nearest-neighbor model at $t \sim 1/J$ (tiny residual values are due to finite size), whereas for a polar gas, η plateaus at a large value, indicating a long-lived memory of initial conditions. We have checked that the plateau is already evident for $V/J > 20$.

5.4.3. Long-time evolution and disorder-free localization

A longer-time evolution reveals eventual delocalization due to weak couplings between Fock states belonging to the same small block of the shattered Hilbert space. This coupling results from the non-resonant processes involving intermediate states in other blocks (Sec. 5.4.1). For large-enough V/J, many such virtual excursions are necessary, and hence the coupling between Fock states becomes exponentially small in J/V. This quasi-localization within the shattered block B (of size Ω_f), to which $|\psi(t=0)\rangle$ belongs is well visualized by monitoring

$$|\psi(t)\rangle = \sum_{f\in B} \langle f|\psi(t)\rangle|\ f\rangle,$$

and determining the participation ratio

$$\mathrm{PR}(t) = \left(\sum_{f\in B} |\langle f|\psi(t)\rangle|^4\right)^{-1}.$$

In Fig. 5.8 we depict $\kappa(t) = \mathrm{PR}(t)/\mathrm{PR}(\infty)$ showing that the long-lived memory of initial conditions observed in $\eta(t)$ results from the fact that only a limited fraction of the Hilbert-space block is effectively reached during the plateau time. Note that the Fock states belonging to B are those which are eventually connected to the initial states, we numerically determine them by ordering the Fock states $|f\rangle$ with a decreasing value of $|\langle f|\psi(\tau\to\infty)\rangle|^2$, where $|\psi(\tau\to\infty)\rangle$ is the asymptotic time-evolved state, and then summing them until reaching $\sum_{f\in B}|\langle f|\psi(\tau\to\infty)\rangle|^2 = 0.95$.

The two-stage dynamics is evident in the evolution of the entanglement entropy, S_{vN}, calculated from a partition of the system to one half (Fig. 5.9). In contrast to standard MBL, the lack of local integrals of motion results in the absence of logarithmic growth of S_{vN}, which plateaus during the localization, and only grows due to the eventual delocalization at finite V/J. The time of the on-set of the second stage scales exponentially with V/J, being observable for $N=8$ and $L=16$ for $V/J\simeq 30$ but prohibitively long for typical experiments for $V/J > 50$.

Moreover, our analysis of different system sizes (see Fig. 5.7) shows that the delocalization time also scales exponentially with the system size, since even more intricate virtual excursions are needed to connect different Fock states in the block. Note also that the high-order excursions responsible for the eventual delocalization are cancelled even by an infinitesimal small disorder (of the order of the inverse size of the whole Hilbert space), as shown in Fig. 5.10, whereas the same tiny disorder has a negligible effect for

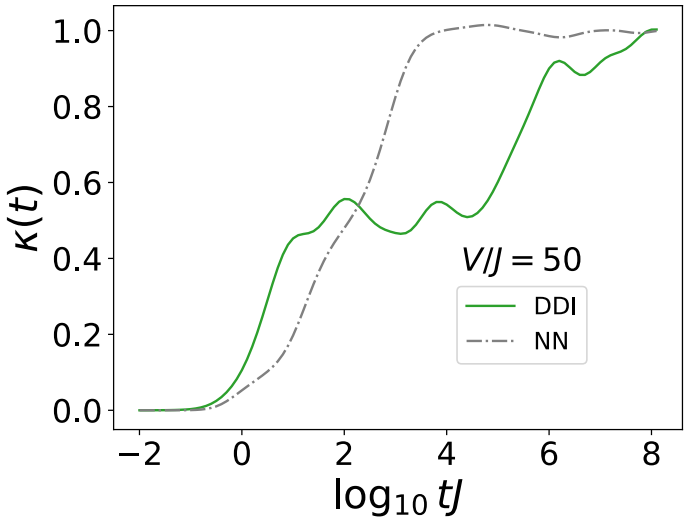

Figure 5.8: $\kappa(t)$ (see text) for the nearest-neighbor model (dotted-dashed grey) and the polar gas (solid green), with $N/L = 8/16$.

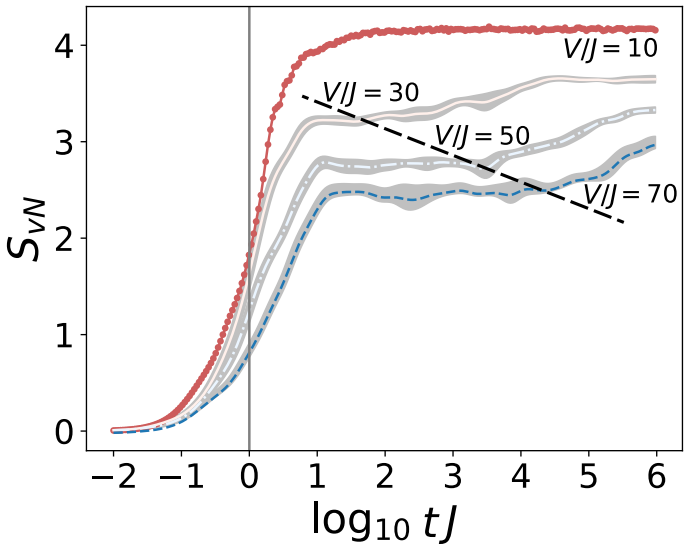

Figure 5.9: Entanglement entropy S_{vN} evaluated for a partition of half of a clean polar lattice system, for $N/L = 8/16$ and different ratios V/J.

the nearest-neighbor model.

5.4.4. Peculiar initial states and boundary effects

Finally, similar to other systems with kinetic constraints, particle dynamics strongly depends on the particular initial condition. Although the lack of a general resonant motion mechanism will slow down and (quasi-)localize typical states, some particular states may remain delocalized even for very large V/J. This is the case of a density wave with a single

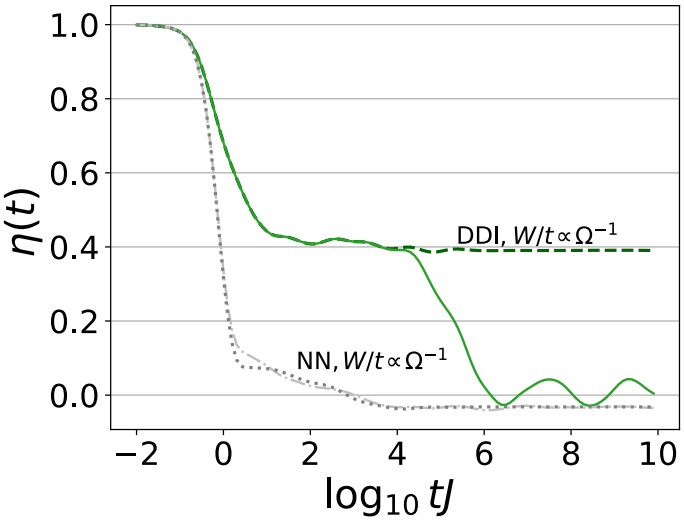

Figure 5.10: Same as Fig. 5.7 for $N/L = 8/16$, comparing the clean case with that with a very small disorder $W/J = 1/\Omega \sim 2 \times 10^{-4}$ (averaged over 1000 realizations), with Ω the size of the Hilbert space.

domain wall,

$$|\ldots\bullet\circ\bullet\circ\bullet\circ\bullet\circ\circ\bullet\circ\bullet\circ\bullet\circ\bullet\ldots\rangle.$$

With periodic boundary conditions, the wall moves resonantly while preserving the interaction energy to all neighbors, delocalization thus occurs for arbitrary V.

The situation in the presence of boundaries (open boundary conditions) is significantly different. Let us consider the specific case of the state

$$|\psi_0\rangle = |\circ\bullet\circ\bullet\circ\bullet\circ\circ\bullet\circ\bullet\circ\bullet\circ\rangle.$$

Note that a single particle hop can displace the domain wall $\circ\circ$ by two sites.

In the nearest-neighbor model, for sufficiently large V/J, the state $|\psi_0\rangle$ belongs to a Hilbert space fragment, which in this case is formed by 7 degenerate Fock states that differ only by the position of the domain wall. In the polar lattice gas, for simplicity of the argument we consider at the moment just the interactions up to next-to-nearest-neighbors. All 7 states of the nearest-neighbor block have the same overall next-to-nearest-neighbor energy $V/2$, except the two states with the domain wall at the boundaries, e.g.,

$$|\circ\circ\bullet\circ\bullet\circ\bullet\circ\bullet\circ\bullet\circ\rangle,$$

which have an energy $V/2+V/8$. As a result, if V/J is sufficiently large, those states cannot

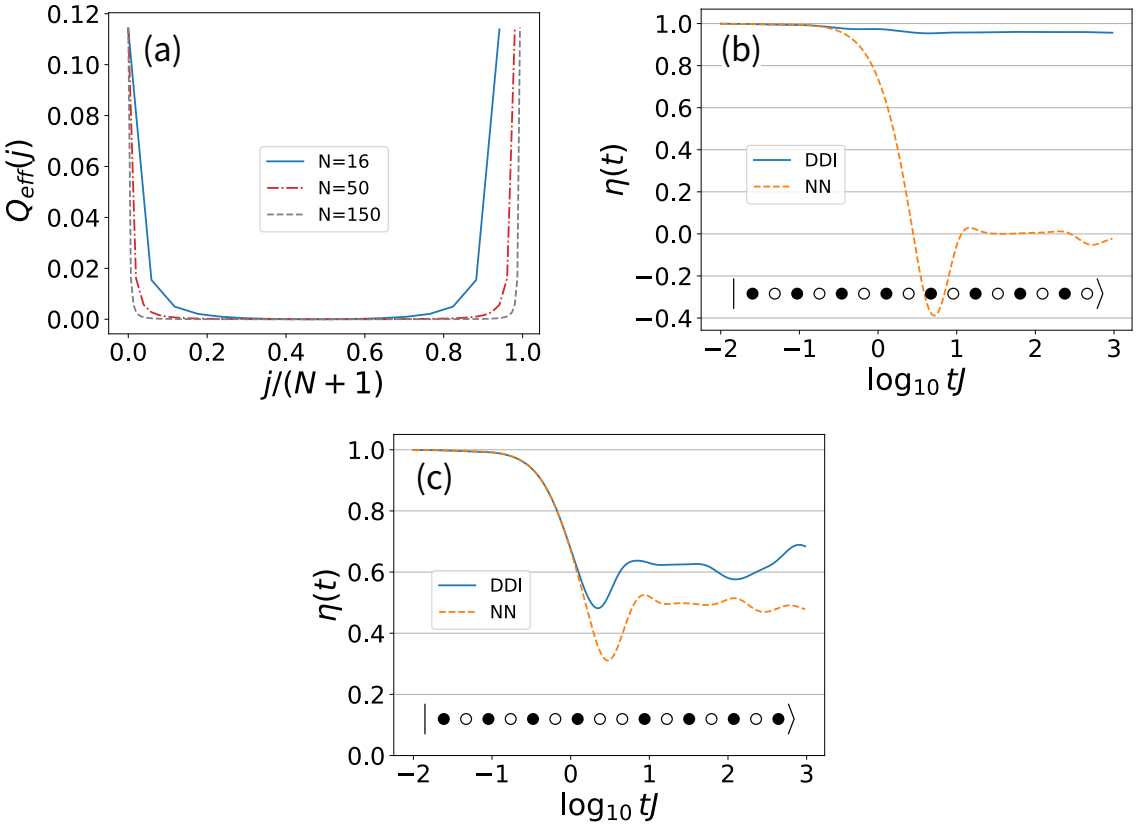

Figure 5.11: (a) Effective potential Q_{eff} experienced by the domain wall (holon dimer) in a density wave (see text) for different system sizes. (b) Comparison of $\eta(t)$ for a nearest-neighbor model and a polar lattice gas for an initial density-wave state (inset), for $V/J = 40$, $W = 0$, and $N/L = 8/16$. Note that in the nearest-neighbor model, the system delocalizes, whereas the polar gas is characterized by a strong localization. (c) Same as (b) but for an initial domain wall at the middle (inset).

be reached starting from $|\psi_0\rangle$. A similar reasoning shows that further sites approaching the boundaries are blocked in the polar gas when V/J grows due to interactions beyond next-to-nearest-neighbor.

Indeed the boundary induces an effective confinement for the domain wall, preventing it to reach a distance $\sim (V/J)^{1/3}$ from the lattice edges. Figure 5.11 (a) shows the effective potential Q_{eff} induced by the boundaries on the domain wall for different system sizes. The energy at the edges increases rapidly. As a result, if we consider as the initial condition the density-wave state (Fig. 5.11 (b)), then the dynamics remains basically frozen in the polar lattice gas, whereas in the nearest-neighbor model the system gets quickly homogeneous. In contrast, if the domain wall is initiated at the middle of the lattice (Fig. 5.11 (c)), it moves until approaching the edges, where it is repelled by the effective potential. In the nearest-neighbor model, the homogenenization $\eta(t)$ approaches 0.5 rather than 0, this is because if the domain wall moves to the right (left), the left (right)

singlons are blocked.

The boundary effects induced by the dipolar tail hence result in yet another mechanism for interaction-induced localization in experiments, which may be especially relevant for small lattices.

5.5. Conclusions

Emerging dynamical constraints induced by the dipolar $1/r^3$ tail lead to Hilbert-space shattering, which at half-filling occurs for $V/J \gtrsim 20$. These constraints disrupt the resonant transport characteristic of nearest-neighbor models, resulting in a dramatic slow-down of the particle dynamics and eventual disorder-free localization. Although we have focused on the dynamics once shattering develops, a significant slow-down is expected for smaller V/J that not yet shattered nearest-neighbor blocks. Thefefore, in general, our results indicate that the tail effects can be utilized for studying many-body localization with suppressed disorder (Appendix C). It brings to light new information on the intensive debate [138, 139, 140, 141]: whether the many-body localization can exists, with finite critical disorder, at the thermodynamic limit.

Our results also show that the study of the interplay between disorder- and interaction-induced localization is well within reach of future experiments on polar lattice gases. For magnetic atoms, recent experiments have achieved $V/J \simeq 3$ [47], but the use of Feshbach molecules of lanthanide atoms [183] and/or subwavelength [184, 185] or UV lattices may significantly boost the V/J ratio. As already mentioned in Sec. 3.3, ratios of $|V|/t \simeq 30$ or even larger should be readily attainable in experiments in the next future. Polar molecules offer exciting possibilities for large V/J even without the need of a special lattice, due to their much stronger dipolar interaction, orders of magnitude larger than that of magnetic atoms [186]. Note that, although the focus in this chapter was on one-dimensional systems, emerging kinetic constraints should also lead to strong disorder-free localization in two dimensions. Indeed, as we discuss in the next chapter, two-dimensional lattices present further additional localization mechanisms absent in one dimension. Moreover, the results have a more general applicability, being potentially relevant for other disorder-free systems with more general long-range interactions, in particular trapped ions [107], where intriguing localization properties may result from the interplay between power-law exchange and Ising terms.

Chapter 6

Dynamics in two-dimensional polar lattice gases

Up to this point in the Thesis, we have focused on the dynamics in one-dimensional lattices. In this chapter, we discuss the motion of polar particles in two-dimensional lattices, concentrating in particular on the motion of inter-site dimers and clusters. The physics of inter-site dimers and generally clusters in two-dimensional lattices is strikingly different than that of on-site clusters in the absence of inter-site interactions. In one-dimensional systems, both on-site repulsively-bound pairs and hard-core nearest-neighbor dimers move in second order in the same lattice as that of singlons [18, 65, 97, 158, 160, 161, 162]. For on-site repulsively-bound pairs this remains true in any dimension. In stark contrast, tightly-bound nearest-neighbor dimers in two-dimensional lattices move in an effective lattice, whose geometry is generally different than that of the original one. Interestingly, dimers may acquire in this way topological properties [187].

In this Chapter, we discuss in detail the two-dimensional dynamics of polar lattice gases, showing that the realization of effective dimer lattices results in a peculiar quantum dynamics, characterized by multiple time scales. Although the effect is general to all two-dimensional geometries, it is particularly interesting in triangular and diamond lattices with hard-core bosons, or square lattices for soft-core bosons. In those lattices, although nearest-neighbor dimers move resonantly, dimer quasi-localization occurs due to the effective dimer lattices, which has either a kagome or a Lieb geometry, and hence presents a flat band [189]. Furthermore we discuss the motion of trimer clusters, showing that in polar gases, remarkably, trimers in triangular lattices move resonantly, and indeed faster than quasi-flat-band dimers. Our analysis is completed by a discussion of the decay of larger

clusters, as well as of dimer-singlon and dimer-dimer collisions, showing that sufficiently dilute two-dimensional polar lattice gases are expected to present partial quasi-localization in absence of disorder due to the formation of pinned clusters. Although we focus on polar gases, a similar intriguing quantum walk dynamics of dimers and clusters may be observed in other extended Hubbard models, as well as in magnon bound states in 2D XXZ chains.

The results of this Chapter have been published in Ref. [188].

6.1. Two-dimensional model

We consider a polar gas of hard-core bosons in a two-dimensional optical lattice, with the dipoles orthogonal to the lattice plane. The system is well described by the Hamiltonian

$$H = -\sum_{\mathbf{j},\mathbf{v}} J_{\mathbf{v}} \left(\hat{a}^\dagger_{\mathbf{j}+\mathbf{v}} \hat{a}_{\mathbf{j}} + \text{H.c.} \right) + \frac{V}{2} \sum_{\mathbf{i}\neq\mathbf{j}} \frac{\hat{n}_{\mathbf{i}} \hat{n}_{\mathbf{j}}}{|\mathbf{i}-\mathbf{j}|^3}, \tag{6.1}$$

where, as in previous chapters, V characterizes the dipole-dipole interaction to nearest neighbors, $\hat{a}_{\mathbf{j}}$ is the bosonic operator at site $\mathbf{j}$, and we impose the hard-core constraint $(\hat{a}^\dagger_{\mathbf{j}})^2 = 0$. The hopping rate from a site $\mathbf{j}$ to the nearest neighbors $\mathbf{j}+\mathbf{v}$ is denoted by $J_{\mathbf{v}}$. Although the ground-state landscape of polar lattice gases in two-dimensional geometries is very rich [58], in this chapter we will concentrate on the surprising dynamics given by the interplay between lattice geometry and long-range interactions.

6.2. Dimers in triangular lattices

The specific case of a triangular lattice (Fig. 6.1 (a)), discussed throughly in the next sections, is characterized by the primitive vectors $\mathbf{a}_0 = \mathbf{e}_x$ and $\mathbf{a}_1 = \frac{1}{2}\mathbf{e}_x + \frac{\sqrt{3}}{2}\mathbf{e}_y$. Hence the site $\mathbf{j} = (j_0, j_1)$ is placed at the position $\mathbf{r}_{\mathbf{j}} = j_0\mathbf{a}_0 + j_1\mathbf{a}_1$. The possible nearest-neighbors are placed at $\mathbf{j}+\mathbf{v}$ with $\mathbf{v} \in \{\mathbf{v}_0 = \mathbf{a}_0 = (1,0), \mathbf{v}_1 = \mathbf{a}_1 = (0,1), \mathbf{v}_2 = \mathbf{a}_0 - \mathbf{a}_1 = (1,-1)\}$. The reciprocal lattice is determined by the vectors $\mathbf{b}_0 = 2\pi\mathbf{e}_x - \frac{2\pi}{\sqrt{3}}\mathbf{e}_y$ and $\mathbf{b}_1 = \frac{4\pi}{\sqrt{3}}\mathbf{e}_y$. The first Brillouin zone is depicted in Fig. 6.1 (a), with the high symmetry points $\Gamma = (0,0)$, $K = (\frac{2\pi}{\sqrt{3}}, 2\pi)$, and $M = (0, \frac{2\pi}{\sqrt{3}})$. We assume $J_{\mathbf{v}} = J$ for all nearest-neighbors $\mathbf{v}$, and defer the discussion on different $J_{\mathbf{v}}$ to Sec. 6.3.

6.2.1. Dynamically-bound dimers

Despite not being thermodynamically stable for $V > 0$, nearest-neighbor dimers, with energy $\simeq V$, remain dynamically stable, for strong-enough V/J. The analysis of the

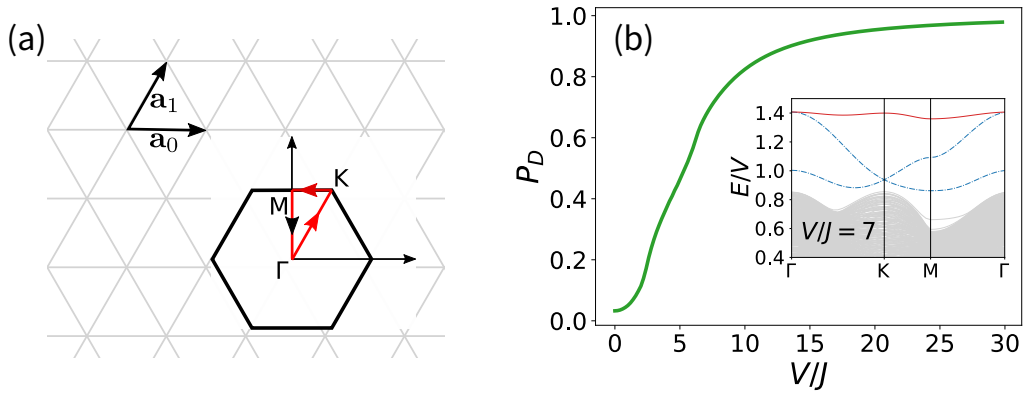

Figure 6.1: (a) Triangular lattice and its first Brillouin zone (inset). (b) Survival probability (6.4) of a dimer in a triangular lattice. The results were obtained by exact time evolution of H_D for two particles initially placed at nearest neighbors. In the inset we depict the two-particle eigenstates for $V/J = 7$. Note that the three bound dimer states are already fully separated from the continuum of scattering states. The dispersion is depicted following the path connecting the symmetry points in the Brillouin zone.

formation of 2D dynamically-bound dimers follows a similar theory as that in 1D, discussed in Chapter 3. Two-particle states are parameterized by the center of mass position, $\mathbf{R} = (\mathbf{r}_A + \mathbf{r}_B)/2$ and relative coordinate, $\mathbf{r} = \mathbf{r}_A - \mathbf{r}_B$. The Hamiltonian acquires the form

$$\begin{aligned} H = & - J_{\mathbf{v}} \sum_{\mathbf{R},\mathbf{r},\mathbf{v}} \Big[\Big(|\mathbf{R} + \frac{\mathbf{v}}{2}, \mathbf{r} + \mathbf{v}\rangle + |\mathbf{R} + \frac{\mathbf{v}}{2}, \mathbf{r} - \mathbf{v}\rangle \Big) \langle \mathbf{R}, \mathbf{r}| \\ & + \Big(|\mathbf{R} - \frac{\mathbf{v}}{2}, \mathbf{r} + \mathbf{v}\rangle + |\mathbf{R} - \frac{\mathbf{v}}{2}, \mathbf{r} - \mathbf{v}\rangle \Big) \langle \mathbf{R}, \mathbf{r}| \Big] \\ & + \sum_{\mathbf{R},\mathbf{r}} \frac{V}{r^3} |\mathbf{R}, \mathbf{r}\rangle\langle \mathbf{R}, \mathbf{r}|, \end{aligned} \tag{6.2}$$

where $r = \sqrt{r_0^2 + r_1^2 + r_0 r_1}$ is the distance between particles placed with a relative vector $\mathbf{r} = r_0 \mathbf{a}_0 + r_1 \mathbf{a}_1$. Applying the Fourier transform to the center of mass, $|\mathbf{R}, \mathbf{r}\rangle = \frac{1}{\sqrt{\Omega}} \sum_{\mathbf{R}} e^{i\mathbf{K}\cdot\mathbf{R}} |\mathbf{r}\rangle_{\mathbf{K}}$, then for a given quasi-momentum $\mathbf{K}$, we obtain the Hamiltonian

$$H_{\mathbf{K}} = -J_{\mathbf{K},\mathbf{v}} \sum_{\mathbf{r},\mathbf{v}} \left(|\mathbf{r} + \mathbf{v}\rangle\langle \mathbf{r}| + |\mathbf{r} - \mathbf{v}\rangle\langle \mathbf{r}| \right)_{\mathbf{K}} + \sum_{\mathbf{r}} \frac{V}{r^3} \left(|\mathbf{r}\rangle\langle \mathbf{r}| \right)_{\mathbf{K}}, \tag{6.3}$$

with $J_{\mathbf{K},\mathbf{v}} = 2J_{\mathbf{v}} \cos\left(\frac{\mathbf{K}\cdot\mathbf{v}}{2}\right)$.

When evaluating Eq. (6.3), we should avoid double counting $\mathbf{r}$ and $-\mathbf{r}$. We hence impose $\mathbf{r} = (r_0, r_1)$, such that $r_0 \leq 0$, and for $r_0 = 0$, $r_1 > 0$. This requires particular care at $r_0 = 0$. In particular, we impose that the hop in the $-\mathbf{v_0}$ direction couples $(1, r_1 \leq 0)$ with $(0, -r_1)$, and the hop in the $-\mathbf{v_2}$ direction couples $(1, r_1 < -1)$ with $(0, -(1 + r_1))$.

For the square lattice, discussed below in this chapter, the procedure is identical, except for the absence of the $J_{\mathbf{v_2}}$ hop, and that for the relative vector $\mathbf{r} = (j_x, j_y)$, $r = \sqrt{j_x^2 + j_y^2}$.

We diagonalize (6.3) for each $\mathbf{K}$, which provides the two-particle eigenstates $E_\alpha(\mathbf{K})$, which we depict in figures below following the trajectory Γ-K-M in the Brillouin zone (inset of Fig. 6.1 (a)). Bound dimers are characterized by sharp lines in the plot of energy eigenvalues $E_\alpha(\mathbf{K})$, whereas scattering states of two unbound particles lead to an energy continuum. In a triangular lattice, for $V/J = 7$ (see the inset of Fig. 6.1 (b)) the bound dimer states are already clearly separated from the scattering states. Note the formation of three different bound states, which we will discuss in detail in the next section. We calculate the survival probability of dimer in 2D by means of

$$P_D = \frac{1}{\Omega_{\mathbf{K}}} \sum_{\mathbf{K},\mathbf{r},\alpha} |\langle \alpha | r = 1 \rangle_{\mathbf{K}}|^2 |\langle \alpha | \mathbf{r} = \mathbf{a}_0 \rangle_{\mathbf{K}}|^2, \tag{6.4}$$

where $\Omega_{\mathbf{K}}$ is the number of quasi-momenta in the first Brillouin zone. Figure 6.1 (b) shows that for $V/J \gtrsim 10$, nearest-neighbor dimers remain tightly bound.

6.2.2. Dynamics of dimers in triangular lattices

Whereas in 1D lattices, or in any other 2D lattice, a dimer moves in second order with a hopping $\propto J^2/V$, dimer motion in triangular lattices is resonant, with hopping J, since a particle in the dimer can move to a neighboring site while keeping a constant distance from its partner. One could hence expect that dimers move fast, in a V-independent time scale when V/J is sufficiently large. This expectation turns out to be incorrect.

Figure 6.2 (a) depicts, for various V/J, the time-evolved probability P_{34} of finding a particle between a distance of 3 and 4 lattice units from the initial center-of-mass of the dimer (shaded region in the inset). Figure 6.2 (b) shows for $V/J = 20$ the time dependence of the distance between the center-of-mass of the two-particle system and its initial position. Whereas for $V = 0$ the particles expand ballistically with a velocity $\propto J$, when V/J grows, two markedly different expansion velocities become apparent, a fast one proportional to J, and a slow one proportional to J^2/V. These two time scales are apparent even down to $V/J = 5$ (see Fig. 6.2 (a)), at which dimers are still largely unbound (see Fig. 6.1 (b)).

Our results are obtained by exact evolution of Eq. (6.1), we consider a 13×13 site, along $\mathbf{a}_0$ and $\mathbf{a}_1$, imposing absorbing boundary conditions. The latter is necessary for observing expansion in long time scales, without the distorting effect due to the reflection

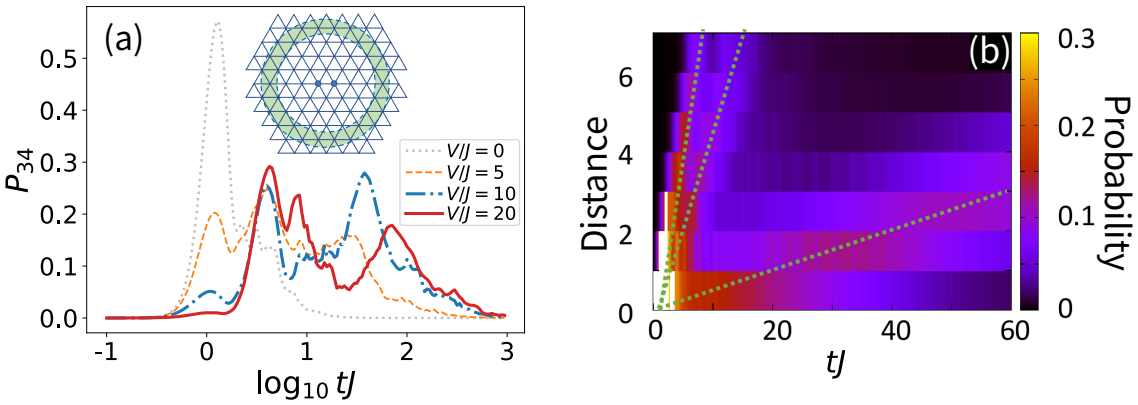

Figure 6.2: (a) Two-particle evolution in a triangular lattice for various V/J. Probability P_{34} to find the center of mass of the two particles at a distance between 3 and 4 lattice units from the initial center-of-mass position. The existence of two marked wavefronts result in two separated peaks in P_{34} when the wavefront crosses the region $3 < r < 4$. The peak at $Jt = 1$ observable for $V/J = 0$ and $V/J = 5$ corresponds to the individual singlon expansion. (b) Probability for $V/J = 20$ of finding the center-of-mass at a given distance in lattice units from its initial position. Dotted lines are a guide to the eye.

of matter waves at the lattice boundaries.

The peculiar dimer dynamics stems from the actual dimer dispersion shown in Fig. 6.3 (a), for $V/J = 10$, where for a given center of mass quasi-momentum $\mathbf{K}$, we depict the spectrum associated to the relative coordinate between the particles. Similar to 1D dimers (see Fig. 3.2), above the continuum of scattering states, we observe bound states characterized by a localized relative coordinate, and hence by sharp lines as a function of $\mathbf{K}$. These bound states, with energy $\simeq V$, correspond to dynamically stable dimers, which for large V/J are tightly bound at nearest neighbor. Whereas 1D dimers present a single band, dimers in triangular lattices appear in three different bands.

To understand this, we may associate to each dimer an effective lattice site placed at the center of mass of the two particles lies. The motion of one of the particles to neighboring sites results in dimer hopping, with rate J, into one of four neighboring links (Fig. 6.3 (b)). Crucially, this resonant dimer motion does not take place in a triangular lattice, but in a kagome lattice with halved inter-site distance (Fig. 6.3 (c)). As it is well known [189], kagome lattices present three bands, including an upper flat band. The emerging kagome geometry hence results in the three dimer bands observed in Fig. 6.3 (a).

The presence of the upper flat band in the dimer spectrum results in the anomalously slow dynamics observed in Fig. 6.2 (a). An initially localized dimer, projects into all three dimer bands with approximately equal probability. The dimer projection into the flat band (which we denote as flat-band dimer) does not move in first order at large V/J. However,

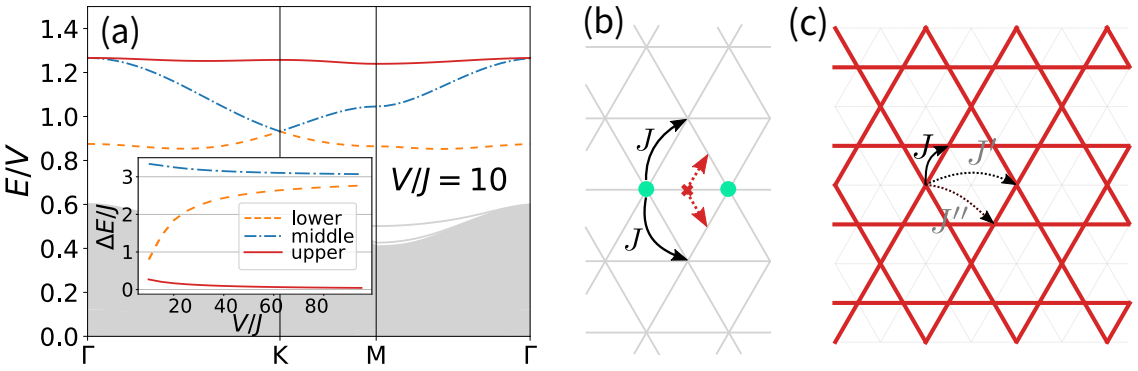

Figure 6.3: (a) Two-particle eigenenergies in a triangular lattice for $V/J = 10$ as a function of the center-of-mass quasimomentum within the Brillouin zone (see Fig. 6.1 (a)), the inset shows the bandwidth of the dimer bands as a function of V/J. (b) A particle in a tightly-bound dimer can hop resonantly to a neighboring site while keeping a fixed distance to its partner, resulting in the motion of the center of mass. (c) In a triangular lattice (thin, gray) the center of mass of a dimer moves in a kagome lattice (thick, red) for large V/J. The center of mass moves resonantly, with J, into its nearest-neighbors, and in second order to its next-nearest neighbors, with hopings J' and J'' (see text)

second-order processes involving the virtual breaking of the dimer result in hoppings into next-to-nearest-neighbor sites in the effective dimer kagome lattice, with hopping rates $J' = \frac{8}{7}\frac{J^2}{V}$ and $J'' = \frac{3\sqrt{3}}{3\sqrt{3}-1}\frac{J^2}{V}$ (Fig. 6.3 (c)). These processes induce a non-zero curvature of the flat band, resulting in the slow propagation of flat-band dimers.

For intermediate V/J values, although the dimers are already tightly bound, second and higher-order processes significantly distort also the other two bands compared to the exact kagome case. The inset of Fig. 6.3 (a) depicts the bandwidth for the lower, middle, and upper dimer bands. Note that, as mentioned above, the upper band is very narrow even at low V/J, and whereas in the kagome lattice the two lower bands have equal width, for lower V/J, the lowest band is significantly narrower. Convergence to the kagome dispersion is only reached at very large $V/J \gtrsim 100$. This may lead to a third expansion velocity for $15 \lesssim V/J \lesssim 30$, which is observable in Fig. 6.2 (a) and in Fig. 6.2 (b). Interestingly, this also means that increasing V/J the average velocity of non-flat-band dimers increases up to a V-independent value for large V/J (with an effective hopping rate $\simeq J/5$).

6.3. Modified triangular lattices

The important role played by the effective flat band becomes evident when considering unequal hopping rates, $J_{\mathbf{v}_0} = J_{\mathbf{v}_1} = J$, but $J_{\mathbf{v}_2} = J_H < J$ (see Fig. 6.4 (a)). For

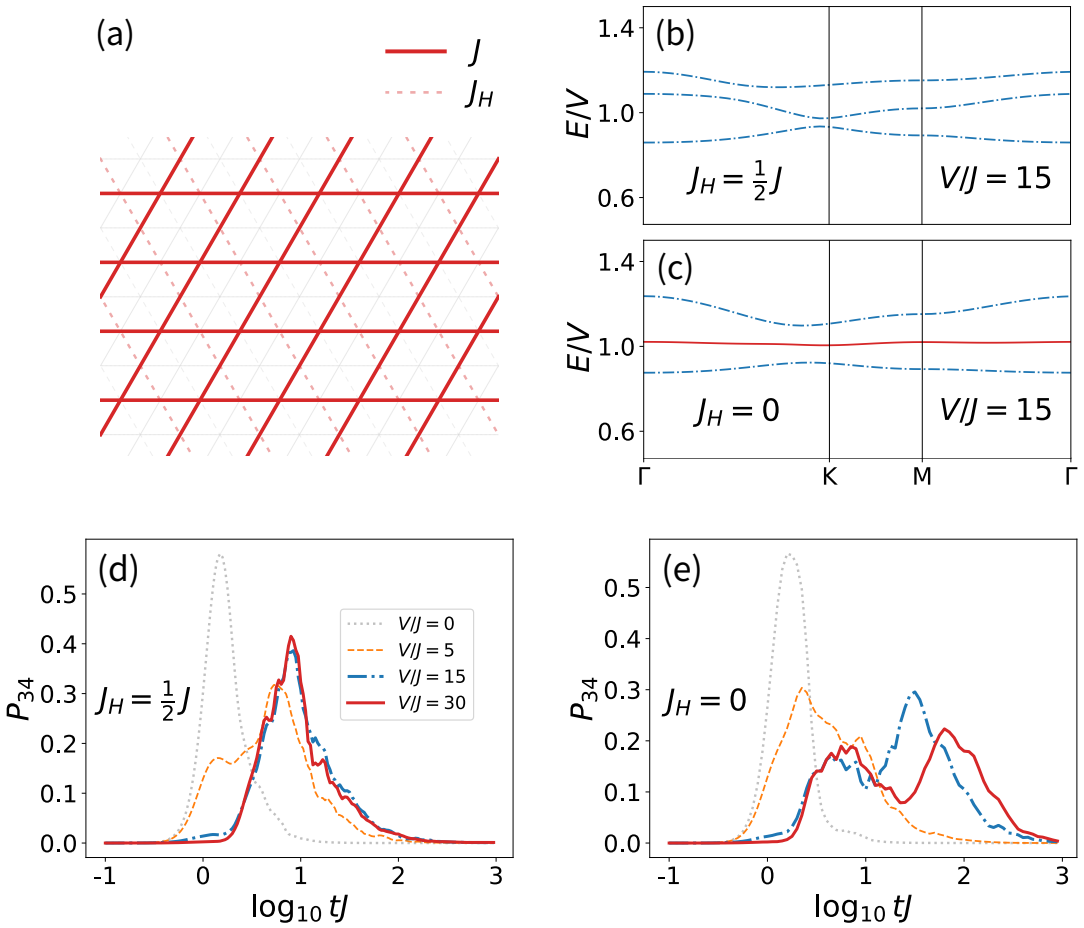

Figure 6.4: (a) Modified triangular lattices with reduced hopping $J_H < J$ along the $\mathbf{a}_0 - \mathbf{a}_1$ direction. The effective dimer lattice is a kagome lattice for $J_H = \pm J$ and a Lieb lattice for $J_H = 0$. (b) Two-particle dispersion for $V/J = 15$ and $J_H = 0.5J$. (c) Similar to (b) but with $J_H = 0$; note the quasi flat middle band as expected for a Lieb lattice. (d) P_{34} for various V/J and $J_H = 0.5J$. (e) Similar to (d) but with $J_H = 0$

$J_H \to 0.5J$, there is no flat band and all three bands have similar bandwidth (Fig. 6.4 (b)). As a result, though the single particle hopping is reduced, the dimer dynamics presents a single timescale $t \sim 1/J$ (see Fig. 6.4 (d)). In contrast, for $J_H = 0$, the lattice acquires a diamond geometry, and the dimer experiences an effective Lieb lattice, which is also well-known to be characterized by a flat middle band [189] (see Fig. 6.4 (c)). Thence, similar to $J_H = J$, a fast and a slow dimer dynamics are again clearly resolved (see Fig. 6.4 (e)). Results are again obtained by exact evolution of Eq. (6.1) with absorbing boundary condition, and initially two particles at nearest neighbor.

6.4. Trimers and strings in triangular lattices

In stark contrast to gases without inter-site interactions, or hard-core gases with inter-site interactions in any other lattice, inter-site-interacting gases in triangular lattices allow

for the resonant motion of a linear string of more than two particles, in which at most two sites are occupied in the same elementary triangle of the lattice. The simplest case is the dynamics of a trimer (a three-particle string), which captures general dynamical properties of a longer string. A closed trimer, that is, with its three particles forming an elementary triangle, can in contrast only move at most in second order.

Tightly-bound linear trimer states can be represented by $|\mathbf{r}_m, n_c\rangle$ with $\mathbf{r}_m$ denoting the position of the central particle, and $n_c \in [0, 8]$ denoting the configuration of the other two particles. The possible nine configurations of linear trimers are depicted in Fig. 6.5 (a). The effective Hamiltonian for a linear trimer is then of the form $H_T = H_{T,0} + H_{T,\mathbf{r}_m} + H_{T,\text{int}}$, where

$$H_{T,0} = -J \sum_{\mathbf{r}_m} \begin{bmatrix} (|\mathbf{r}_m, 3\rangle + |\mathbf{r}_m, 4\rangle + |\mathbf{r}_m, 5\rangle + |\mathbf{r}_m, 6\rangle) \langle \mathbf{r}_m, 0| \\ (|\mathbf{r}_m, 4\rangle + |\mathbf{r}_m, 6\rangle + |\mathbf{r}_m, 7\rangle + |\mathbf{r}_m, 8\rangle) \langle \mathbf{r}_m, 1| + \text{H.c.} \\ (|\mathbf{r}_m, 3\rangle + |\mathbf{r}_m, 5\rangle + |\mathbf{r}_m, 7\rangle + |\mathbf{r}_m, 8\rangle) \langle \mathbf{r}_m, 2| \end{bmatrix} \tag{6.5}$$

is the hoping of the side particles without changing the position of the central one,

$$H_{T,\mathbf{r}_m} = -J \sum_{\mathbf{r}_m} (|\mathbf{r}_m + \mathbf{v}_0, 7\rangle\langle \mathbf{r}_m, 8| + |\mathbf{r}_m + \mathbf{v}_1, 5\rangle\langle \mathbf{r}_m, 3| + |\mathbf{r}_m + \mathbf{v}_2, 4\rangle\langle \mathbf{r}_m, 6| + \text{H.c.}) \tag{6.6}$$

is the hoping of the central particle in the triangular lattice, and

$$H_{T,\text{int}} = V \left(\frac{1}{8} - \frac{1}{3\sqrt{3}} \right) \sum_{\mathbf{r}_m} (|\mathbf{r}_m, 0\rangle\langle \mathbf{r}_m, 0| + |\mathbf{r}_m, 1\rangle\langle \mathbf{r}_m, 1| + |\mathbf{r}_m, 2\rangle\langle \mathbf{r}_m, 2|) \tag{6.7}$$

is the interaction energy difference, given by next-to-nearest neighbor dipole-dipole interactions, between states $|\mathbf{r}_m, 0\rangle$, $|\mathbf{r}_m, 1\rangle$, and $|\mathbf{r}_m, 2\rangle$, and the rest. Applying Fourier transform, $|\mathbf{r}_m, n_c\rangle = \frac{1}{\sqrt{\Omega}} \sum_{\mathbf{r}_m} e^{i\mathbf{K}_m \cdot \mathbf{r}_m} |\mathbf{K}_m, n_c\rangle$, then for a given quasi-momentum $\mathbf{K}_m$:

$$\begin{aligned} H_{T,\mathbf{K}_m} = &- J \begin{bmatrix} (|3\rangle + |4\rangle + |5\rangle + |6\rangle) \langle 0| \\ (|4\rangle + |6\rangle + |7\rangle + |8\rangle) \langle 1| + \text{H.c.} \\ (|3\rangle + |5\rangle + |7\rangle + |8\rangle) \langle 2| \end{bmatrix} \\ &- J \left(e^{i\mathbf{K}_m \cdot \mathbf{a}_0} |7\rangle\langle 8| + e^{i\mathbf{K}_m \cdot \mathbf{a}_1} |5\rangle\langle 3| + e^{i\mathbf{K}_m \cdot (\mathbf{a}_0 - \mathbf{a}_1)} |4\rangle\langle 6| \right) \\ &+ V \left(\frac{1}{8} - \frac{1}{3\sqrt{3}} \right) (|0\rangle\langle 0| + |1\rangle\langle 1| + |2\rangle\langle 2|) \,. \end{aligned} \tag{6.8}$$

Diagonalizing $H_{T,\mathbf{K}_m}$ for $\mathbf{K}_m$ along the symmetry points in the first Brillouin zone provides the dispersion shown in Fig. 6.5 (b), characterized by nine energy bands associated

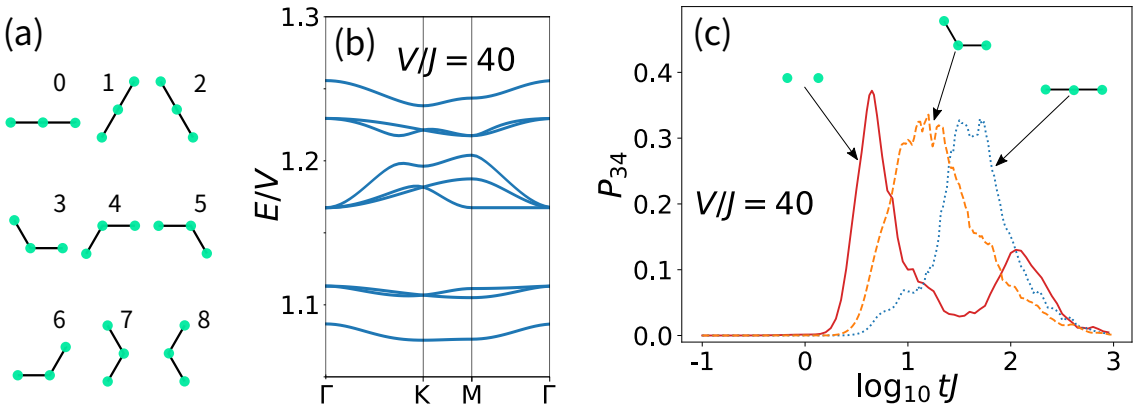

Figure 6.5: (a) All configurations for an open trimer in a triangular lattice. (b) Energy bands for tightly bound open trimers for $V/J = 40$. (c) P_{34} for $V/J = 40$, for an initial dimer and two different initial trimers (see the insets).

to the tight-binding trimer dynamics. None of the bands is flat, implying that an open trimer expands resonantly with a broad velocity distribution but without the bimodal expansion characteristic of dimers, see Fig. 6.5 (c), where we depict the result of the trimer evolution evaluated using the effective Hamiltonian H_T. Note that, remarkably, trimers move in first order faster that flat-band dimers for large-enough V/J.

6.5. Longer strings

A larger open string can resonantly decay into highly mobile singlons and clusters with closed trimers (see Fig. 6.6 for an example). Hence, dilute random distributions spontaneously decay into (i) resonant movers, including singlons, non-flat-band dimers, and open trimers, and (ii) non-resonant clusters that move at most in second order, including flat-band dimers and strings that contain at least one closed trimer. We would like to note at this point that vacancies in lattice gases close to unit filling (i.e., a dilute holon gas) should behave similarly. Note however that Eq. (6.1) does not fulfill particle-hole symmetry. In particular, holons are reflected at the lattice boundaries, since the different coordination number of edge sites imposes an energy penalty V to bulk holons when approaching the edges.

6.6. Many-body dynamics

The presence of more than one cluster may alter the dynamics. Similar to 1D lattices, singlons and dimers at one site of distance may swap positions, inducing a Brownian-like dimer motion (Fig. 6.7 (a)) that may affect flat-band dimers. Additionally, two dimers

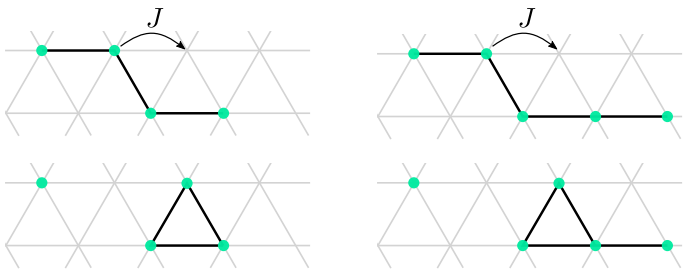

Figure 6.6: Spontaneous decay of an open 4-string (left column) and an open 5-string (right column). Singlon emission creates a cluster with a closed trimer (a triangle) that can only move, at most, in second order.

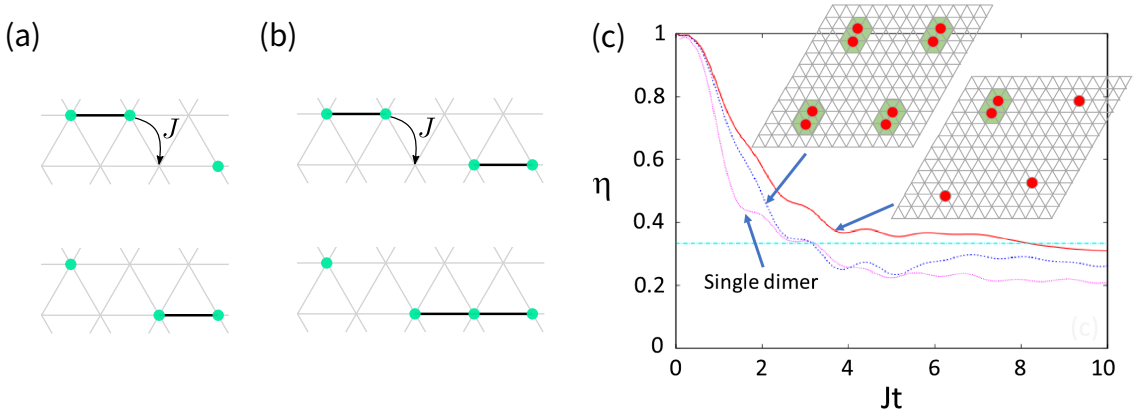

Figure 6.7: (a) Singlon-dimer swaping at nearest neighbors. (b) Dimer-dimer interactions may resonantly form a singlon and an open trimer. (c) Inhomogeneity η for $V/J = 30$ and various initial states (insets). The light-blue dashed line indicates the expected value $\eta = 1/3$ for immobile flat-band dimers.

may resonantly exchange a particle, leaving an open trimer and a singlon (Fig. 6.7 (b)). In polar gases, these processes are prevented for large enough V due to the blockade induced by the $1/r^3$ tail beyond nearest neighbors. If the clusters are not initially at one site of distance, the expansion of resonant movers is significantly restricted when encountering non-resonant clusters, rendering an inefficient many-body propagation. For sparse fillings and large V, the main mechanism of eventual flat-band dimer propagation remains the second-order broadening of the flat band ($\propto J^2/V$).

Figure 6.7 (c) shows our results. We evaluate for a single dimer, one dimer and three singlons, and four dimers (insets of Fig. 6.7(c)) the homogeneity $\eta = (P_s(t) - P_h)/(P_s(0) - P_h)$, where $P_s(t)$ is the average particle number at the initial dimer positions and their nearest-neighboring sites (green regions in the insets of Fig. 6.7 (c)), and P_h is the expected value of P_s if the dimers and singlons were homogeneously distributed. Considering the hard-core constraint and blockade effects, P_h is evaluated excluding the occupied sites, and half of the number of nearest-neighbors of each singlon/dimer. This results in the estimation $P_h = A\frac{N}{L^2-4N_s-6N_D}$, with N_s, the number of singlons, N_D, the number of

dimers, $N = N_s + 2N_D$, the total number of particles, and $A = 10N_D$ is the number of sites in a green region in the insets in Fig. 6.7 (c). Since each dimer projects $\sim 1/3$ to the flat band, for localized flat-band dimers, $P_s(t)$ is expected to be $\frac{2}{3}P_h + \frac{1}{3}2N_D$ with corresponding $\eta = 1/3$, whereas in case of homogenization, $\eta \to 0$. The results are evaluated in a 13×13 triangular lattice with open boundary conditions, for the single dimer the time evolution is obtained exactly by Eq. (6.1), for the other cases it is evaluated by means of TDVP calculations [190], with a bond dimension up to 250.

Due to the resonant movers, η decays within $t \lesssim 4/J$ to $\eta \simeq 1/3$ in all cases, as expected for flat-band-dimer quasi-localization. For a single dimer, η plateaus, and only decays towards homogeneity ($\eta \to 0$) in a much longer time scale $t \gtrsim V/J^2$. The presence of other dimers enhances the localization of flat-band dimers due to the $1/r^3$ tail of the dipole-dipole interaction (we are prevented to see this effect since our TDVP calculations are limited to $t \lesssim 20/J$). Since flat-band dimers move with a second-order hopping rate $\propto J^2/V$. Similar to the case of 1D dimers discussed in Chapter 3, long-range dimer-dimer interactions are expected to lead to the clustering of flat-band dimers, and hence to their localization, if the mean distance between them is smaller than a critical value $\propto (V/J)^{2/3}$.

6.7. Dimer dynamics in square lattices

The peculiar dimer dynamics resulting from an effective dimer lattice constitutes a general feature for any 2D lattices. This may be illustrated by a second relevant example, a square lattice, in which the lattice primitive vectors are identical to the nearest-neighbor vectors, i.e., $\mathbf{a}_0 = \mathbf{v}_0 = \mathbf{e}_x$ and $\mathbf{a}_1 = \mathbf{v}_1 = \mathbf{e}_y$. The hopping in Eq. (6.1) becomes: $-J\sum_{\mathbf{j},\mathbf{v}}\left(\hat{a}^\dagger_{\mathbf{j}+\mathbf{v}}\hat{a}_{\mathbf{j}} + H.c.\right)$, with $\mathbf{v} = \mathbf{e}_x$ or $\mathbf{e}_y$.

6.7.1. Hard-core bosons

For hard-core bosons, dimers cannot move resonantly in a square lattice, but hopping may happen in second order, and result in two different hopping rates: $J' = \frac{4\sqrt{2}}{2\sqrt{2}-1}\frac{J^2}{V}$ and $J'' = \frac{8J^2}{7V}$. The effective decorated square lattice experienced by the center of mass of a dimer in square lattices is shown in Fig 6.8 (a). The effective lattice presents a four-site unit cell (see the inset of Fig 6.8 (a)), and is therefore characterized by four dimer bands. Exact solutions of the four bands are given in App. D. In Fig 6.8 (c) we depict the two-particle spectrum as a function of the center of mass momentum $\mathbf{K}$. The two upper bands correspond to the dimer states. Note that contrary to the triangular lattice, the Brillouin

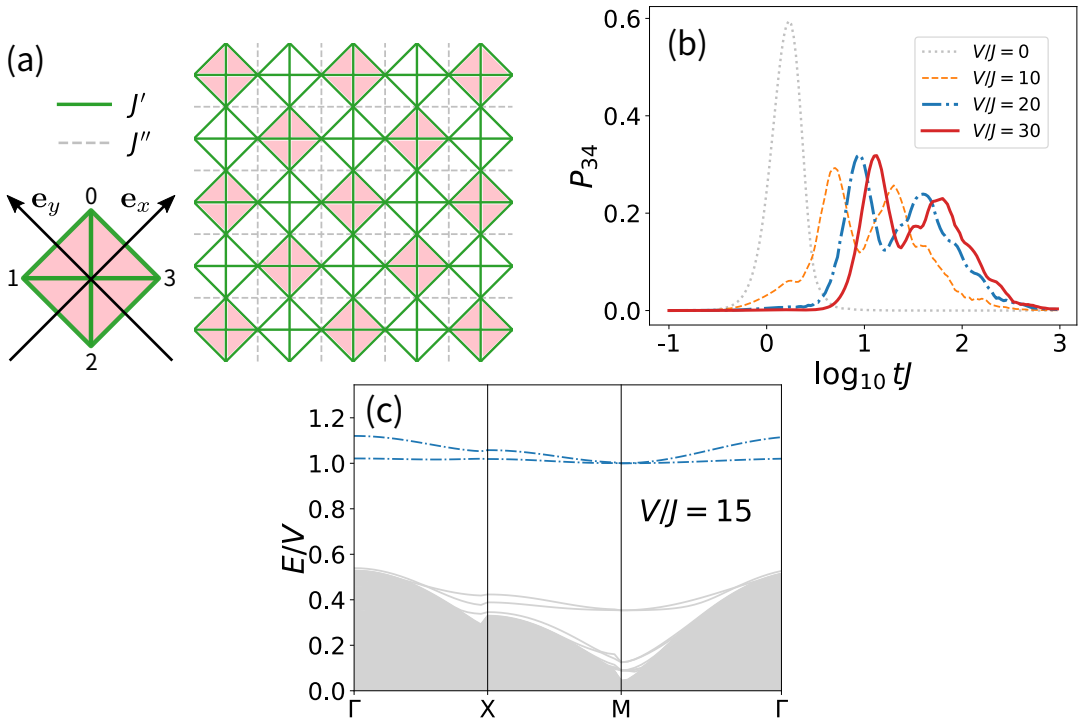

Figure 6.8: (a) For the case of hard-core bosons in a square lattice dimers move in an effective decorated square lattices with four-state unit cells. The second-order hoppings (see text) are denoted by J' (green solid), and J'' (gray dashed). (b) P_{34} for various V. The dimer expansion shows two distinct time-scales, both increasing linearly with V/J. (c) Two particle spectrum for hard-core bosons in a square lattice. Note the appearance of two bound states.

zone of the square lattice and that of the dimer lattice are not the same; as a result the four dimer bands map into the two bands observed in the two-particle spectrum. Note that one of the bands is much narrower than the other, resulting in two markedly different time scales (Fig. 6.8 (b)), although, in contrast to the triangular lattice case, both of them are proportional to V/J^2.

6.7.2. Soft-core bosons

Interestingly, dimers may move resonantly in a square lattice in the soft-core case, i.e., allowing double occupancies, if the on-site interactions $\frac{U}{2}\sum_{\mathbf{j}}\hat{n}_{\mathbf{j}}(\hat{n}_{\mathbf{j}}-1)$, fulfill $U=V$ (this condition may be achieved by means of Feshbach resonances). In that case, a a soft-core dimer moves resonantly with Bose-enhanced hopping $\sqrt{2}\,J$ in an effective Lieb lattice (Fig. 6.9 (a)) formed by doubly-occupied sites (green squares) and the links joining nearest-neighboring sites (red crosses). For $U=V$ the dimer may resonantly hop between these effective sites. The effective Lieb geometry results again in flat-band dimers, and hence in two markedly different time scales (Fig. 6.9 (b)), one fast and V independent for a

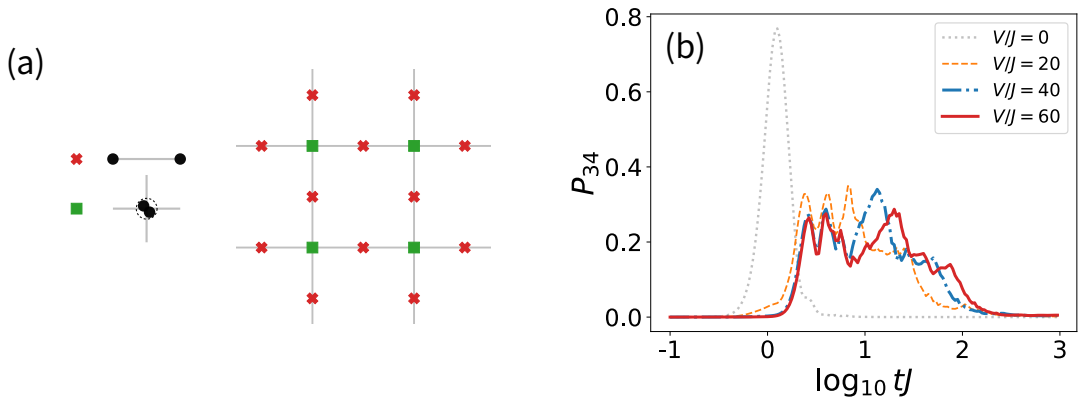

Figure 6.9: (a) For a soft-core Bose-Hubbard model with $U = V$, the dimers experience an effective Lieb lattice formed by doubly occupied sites and nearest-neighbor dimers. The bound state can resonantly move in an effective Lieb lattice by Bose-enhanced hopping, $\sqrt{2}\,J$. (b) P_{34} for soft-core case with various V. The dimer expansion shows two time scales, a fast V-independent one, and a slow one that increases linearly with V.

large-enough V, and one slow proportional to J^2/V given by second- and higher-order processes.

Finally, note that an anomalous dimer dynamics is expected in other 2D lattices. For instance, in honeycomb lattices a dimer also experience kagome structure. But in contrast to the case in triangular lattices, a dimer in honeycomb lattices move only in second order, thus flat-band dimers remain strongly localized, being able to move only in fourth order.

6.8. Conclusions

Two-dimensional polar lattice gases present an intriguing dynamics due to the interplay between energy conservation and inter-site interactions. Dynamically-bound dimers perform a quantum walk in an effective lattice different than that of individual particles, resulting in an expansion characterized by more than one timescale. This intriguing dynamics is particularly remarkable in triangular and diamond lattices, or square lattices for soft-core bosons (or spinless fermions) due to the resonant dimer motion and the emerging quasi-flat band localization. Hence whereas individual particles and trimers expand resonantly, dimer dynamics is largely handicapped by quantum interference. As for other scenarios discussed in this Thesis, we would like to stress that the requires values of V/J to observe this dynamics are well within reach of experiments. Finally, we should mention that although the dipolar tail is relevant in polar gases as throughly discussed in this Thesis, the anomalous dimer dynamics in two-dimensional lattices discussed in this Chapter just requires strong nearest-neighbor interactions. The results are thus valid for any 2D extended Hubbard model, as well as for magnon bound states in 2D XXZ spin models.

Chapter 7

Conclusions and perspectives

In this Thesis, we have explored the intriguing dynamics of polar particles in optical lattices. We have shown that the combination of energy conservation, finite band-width, and dipole-dipole interactions results in novel qualitative features that are absent in the case of non-polar systems. In particular, the formation of dynamically-bound dimers and clusters, which occurs for a sufficiently large dipolar interaction ($V/J \gtrsim 10$) results in a significantly handicapped dynamics due to the role played by the dipolar $1/r^3$ tail, that results in the formation of dimer clusters, which may eventually lead to the cluttering of the whole polar lattice gas, as we discussed in Chapter 3 for the case of one-dimensional lattices. Furthermore, as shown in Chapter 6, dynamically-bound dimers in two-dimensional lattices experience a different lattice than individual particles. As a result, polar lattice gases in two-dimensional lattices present, especially in some particular geometries, an additional interaction-induced localization mechanism. The latter results because the dimer lattice is characterized by the appearance of a flat band, resulting in a very long-lived memory of initial conditions.

Indeed polar lattice gases open exciting perspectives for the study of interaction-induced localization and Hilbert-space fragmentation. In this sense, the role of the dipolar tail is crucial in polar gases. For nearest-neighbor models (Chapter 4) large-enough interactions result in the conservation of the number of occupied nearest-neighbor links, resulting in Hilbert-space fragmentation. However, resonant particle motion remains generally possible within each fragment, hence precluding disorder-free spatial localization. In contrast, for polar lattice gases (Chapter 5) the tail of the dipolar tail induces for growing interactions additional emerging conservation laws. We have shown that the mere additional conservation of the number of occupied next-to-nearest-neighbor links is enough to shatter the Hilbert space. Moreover, the dipolar tail precludes a general mechanism

for resonant motion within a given Hilbert-space fragment. The involved motion hence occurs typically in high-order in perturbation theory, due to virtual excursions to other Hilbert-space blocks. As a result, the dynamics of polar lattice gases is dramatically slowed-down compared to the case of nearest-neighbor interactions, leading eventually to the disorder-free localization.

We stress that the physics discussed in this Thesis is well within reach of experiments. The formation of lattice droplets discussed in Chapter 3 just demands $V/J > 2.5$, which has been already achieved in erbium experiments in Innsbruck [47]. As discussed in Chapters 3 and 6 dynamically-bound dimers demands both in 1D and 2D lattices $V/J \gtrsim 10$, whereas the observation of Hilbert-space shattering (Chapter 5) demands $V/J \gtrsim 20$. As discussed in the Thesis, these values can be readily attainable in lanthanide experiments in UV lattices, and in experiments with polar molecules. Our results should hence be directly relevant for polar lattice gas experiments in the very next future.

We should, however, mention that we expect a significant slow-down of the particle dynamics even for rather low values of V/J, well below the values demanded for Hilbert-space shattering. This is because even if the nearest-neighbor fragments are not shattered, motion within a fragment may be already handicapped (although not completely blocked) by the dipolar tail. An open question for future research hence involves the study of that interaction-induced slow-down as a function of V/J, which should provide crucial information for experiments.

Finally, we should also emphasize that our results may be extrapolated to other power-law interactions, or to more general long-range interactions, particularly in what concerns experiments with trapped ions [107]. An additional future research direction hence concerns the study of slow dynamics, disorder-free localization and Hilbert-space fragmentation for more general power-laws.

Appendices

Appendix A

Dimers in one-dimensional polar lattice gases

In this Appendix we derive the effective Hamiltonian for the motion of a tightly-bound dimer in a one-dimensional polar lattice gas. Let us introduce the projection operator to the nearest-neighbor-dimer subspace $\mathrm{P} = \sum_l |l, l+1\rangle\langle l, l+1|$, and the operator $\mathrm{Q} = \sum_{j,k\geq 2} |j, j+k\rangle\langle j, j+k|$ to the orthogonal subspace.

Usiing the Hamiltonian H of Eq. (3.1), we write the Schrödinger equation for the two-particle eigenstates, $H|\psi\rangle = E|\psi\rangle$. Projecting with P and Q, and using $P + Q = \mathbb{I}$, we have

$$PHP|\psi\rangle + PHQ|\psi\rangle = EP|\psi\rangle, \tag{A.1}$$

$$QHP|\psi\rangle + QHQ|\psi\rangle = EQ|\psi\rangle. \tag{A.2}$$

We are interested in deriving an effective Hamiltonian for states within the subspace of nearest-neighbor particles, i.e., for $|\phi\rangle = P|\psi\rangle$. From the second equation we obtain

$$Q|\psi\rangle = (E - QH)^{-1}QHP|\psi\rangle, \tag{A.3}$$

and hence from the first equation:

$$\underbrace{\left(PHP + PHQ\frac{1}{E - QHQ}QHP\right)}_{H_{\mathrm{dimer}}}|\phi\rangle = E|\phi\rangle. \tag{A.4}$$

Note the fact that $P^2 = P$ and $Q^2 = Q$, we hence obtain an effective Hamiltonian H_{dimer} for the description of tightly-bound nearest-neighbor dimers. The states within

the manifold of nearest neighbors are of the form $|j, j+1\rangle$, then:

$$\begin{aligned} PHP|j,j+1\rangle &= V|j,j+1\rangle, \\ QHP|j,j+1\rangle &= -J(|j-1,j+1\rangle + |j,j+2\rangle). \end{aligned}$$

Hence

$$H_{\text{dimer}}|j,j+1\rangle = \left(V + \frac{2J^2}{E-V/8}\right)|j,j+1\rangle + \frac{J^2}{E-V/8}\left(|j-1,j\rangle + |j,j+2\rangle\right).$$

For $V/J \gg 1$, we can approximated $E \simeq V$ in the denominator $(E-QHQ)^{-1}$, moreover, we may neglect the self-energy term $\left(V + \frac{2J^2}{E-V/8}\right)$, and obtain the effctive Hamiltonian for single-dimer motion:

$$H_D = J_D \sum_j \left(\hat{d}^\dagger_{j+1}\hat{d}_j + H.c.\right), \tag{A.5}$$

with $\hat{d}_j = \hat{a}_j\hat{a}_{j+1}$ and $J_D \equiv \frac{J^2}{V-V/8}$.

Appendix B

Critical disorder for the nearest-neighbor model

In this Appendix we apply the analysis of fractal dimensions to evaluate the critical disorder of MBL in the nearest-neighbor model. However, a standard finite-size scaling method for a critical value W_c based on the $\bar{D}_f^{max}$ results is problematic for a fragmented Hilbert space. Selected fragments of different size may be not comparable due to the different density of singlons, nearest-neighbor links, or other conserved quantities. This is shown in Fig. B.1, where curves of different half-filled lattices do not intersect when W increases. The major reason is that when varying the size of half-filled lattices, especially when changing from even to odd values of L, the fragment that has the $\bar{D}_f^{max}$ does not possess a fixed singlon density. This problem is not present a lower filling, since the fragment of $\bar{D}_f^{max}$ is simply the $l = 0$ one, where the density of singlons is by definition identical to the lattice filling. Another disadvantage of a half-filling lattice is that the fragment with the largest fractal dimension is very small compared to the overall Hilbert space. In contrast, the $l = 0$ fragment remains comparable to the whole Hilbert space as the filling decreases.

Although for quarter-filling we can just evaluate systems with $N/L = 4/16$ and $5/20$, the results show an intersection of the curves, that permits an estimation of the critical disorder W_c (see Fig. B.2). Figure B.2 (top left) shows W_c, for lattices with quarter filling as a function of V/J. For $V \to \infty$, $W_c/J \simeq 4$, which is in good agreement with the results in Ref. [167] (recall Sec. 4.5). Note that although Ref. [167] considered half-filling, the density of movers in their selected block was $N_{\mathbf{0}}/L = 1/4 - 1/L$ that approaches to $1/4$ when $L \to \infty$.

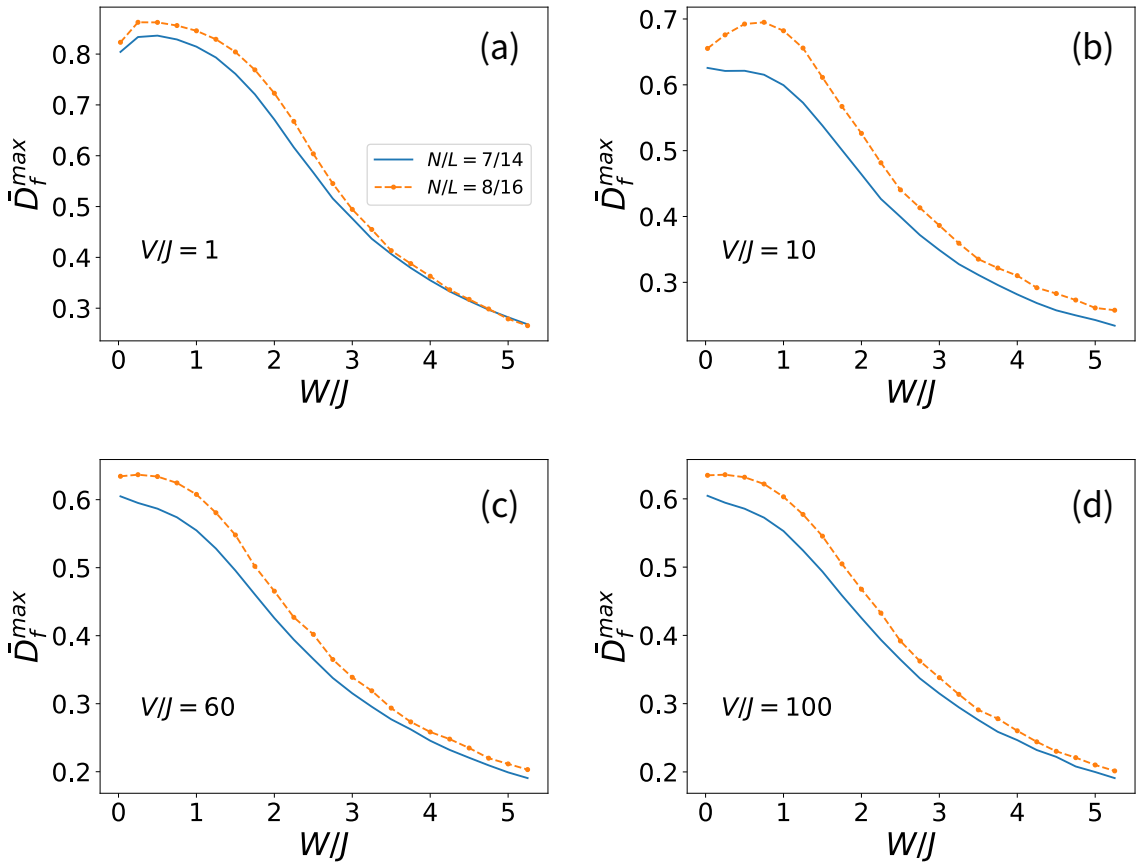

Figure B.1: Curves of $\bar{D}_f^{max}$ of different half-filled lattices, for $V/J = 1$ (a), $V/J = 10$ (b), $V/J = 60$ (c), and $V/J = 100$ (d). The unfixed density of siglons of the block that determines $\bar{D}_f^{max}$ leave the curves with no intersection (see text).

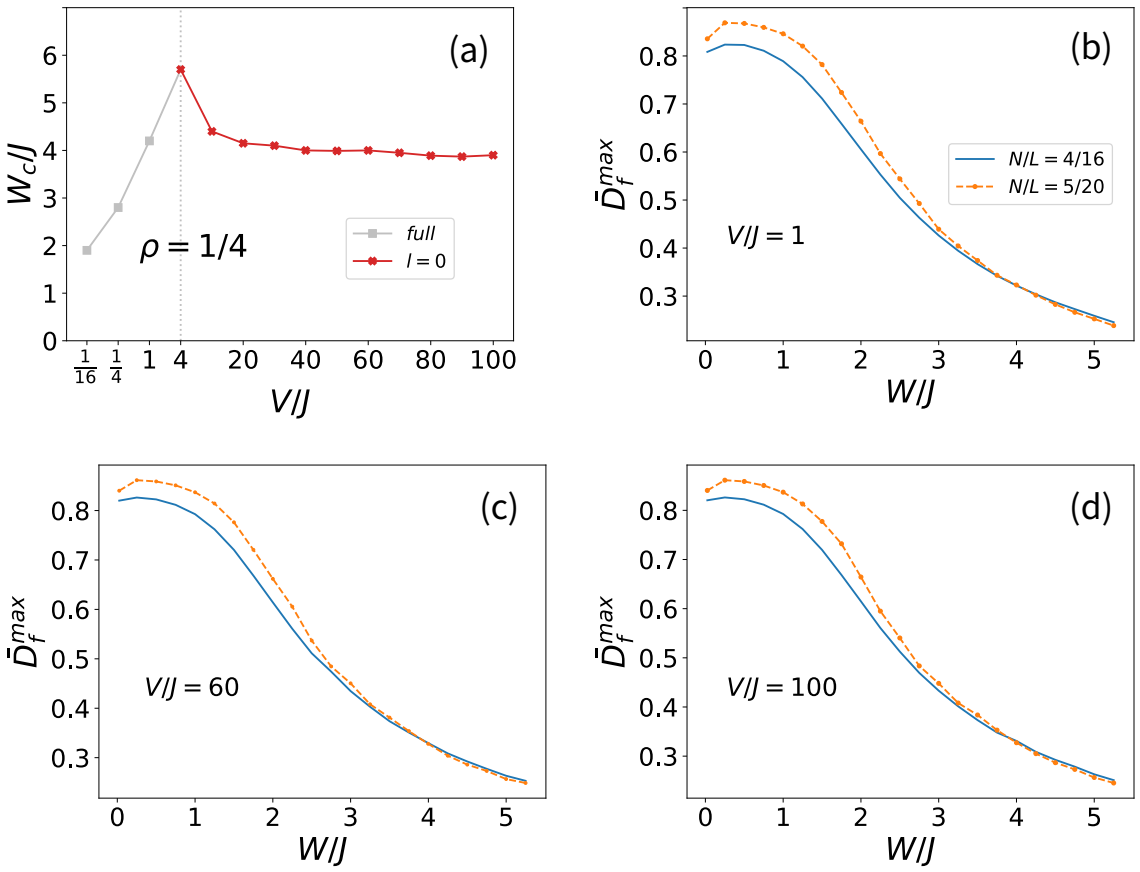

Figure B.2: (a) Critical disorder W_c as a function of V. The value of W_c is determined from the intersection of the $\bar{D}_f^{max}$ curves for different quarter-filled lattices. These intersections are depicted in Figs. (c)-(d), for $V/J = 1$ (b), $V/J = 60$ (c), $V/J = 100$ (d). Contrary to the half-filled cases, for a quarter filling the density of singlons is fixed in the block that determines $\bar{D}_f^{max}$, allowing a finite-size analysis that matches well with the results obtained in Ref. [167].

Appendix C

Suppressed critical disorder in polar lattice gases

In this Appendix we perform the analysis of fractal dimensions for 1D polar lattice gases, and show that the critical disorder of nearest-neighbor model (Appendix B) can be suppressed. Figure C.1 shows IPR_f for two polar lattice gases with low disorder and various V/J. The comparison with Fig. 4.6 shows clearly that the polar lattice gas is much more localized due to the shattering effects. Furthermore, the shattering-increased IPR_f make the most delocalized fragment of the nearest-neighbor model (green shades) not necessarily still the most delocalized one for a polar larrtce gas. To compare with the critical disorder in Appendix B, we consider the $\rho = 1/4$ lattices and focus on the most delocalized states, that is, the flat part where IPR_f remains close to zero (circled area).

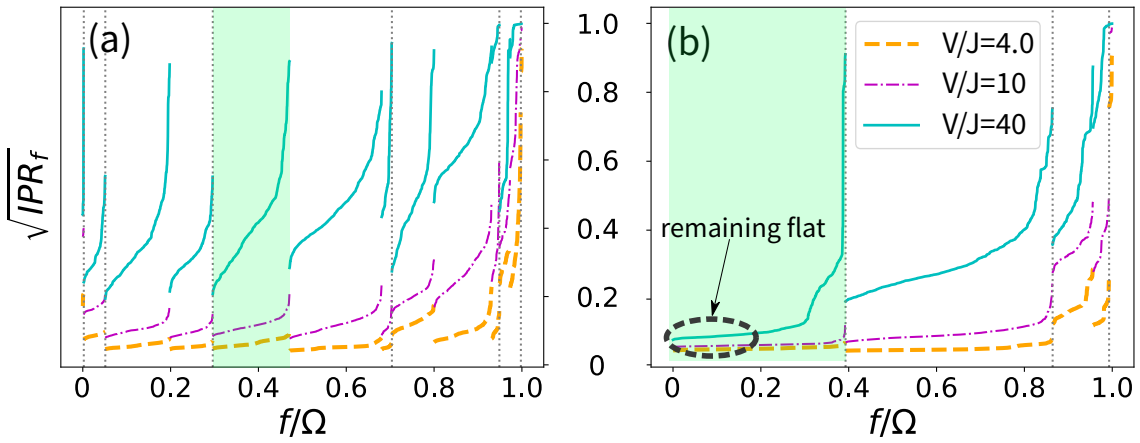

Figure C.1: (a) $\sqrt{\mathrm{IPR}_f}$ obtained from Eq. (5.1) with $N/L = 7/14$ and $W/J = 0.25$ for large V /J. The states are arranged following the same order as in Fig. 4.6.

Figure C.2 (a) and (b) shows the curves of averageed D_f in these flats, as V/J increases intersections that indicating W_c reduce to suppressed values. Though reliable phase boundary is not available because of small system sizes, we still provide a phase diagram here for a qualitative illustration. Figure C.2 (c) shows that the critical points significantly decrease after the Hilbert-space start to shatter severely ($V/J \sim 50$), indicating localization with suppressed critical disorder.

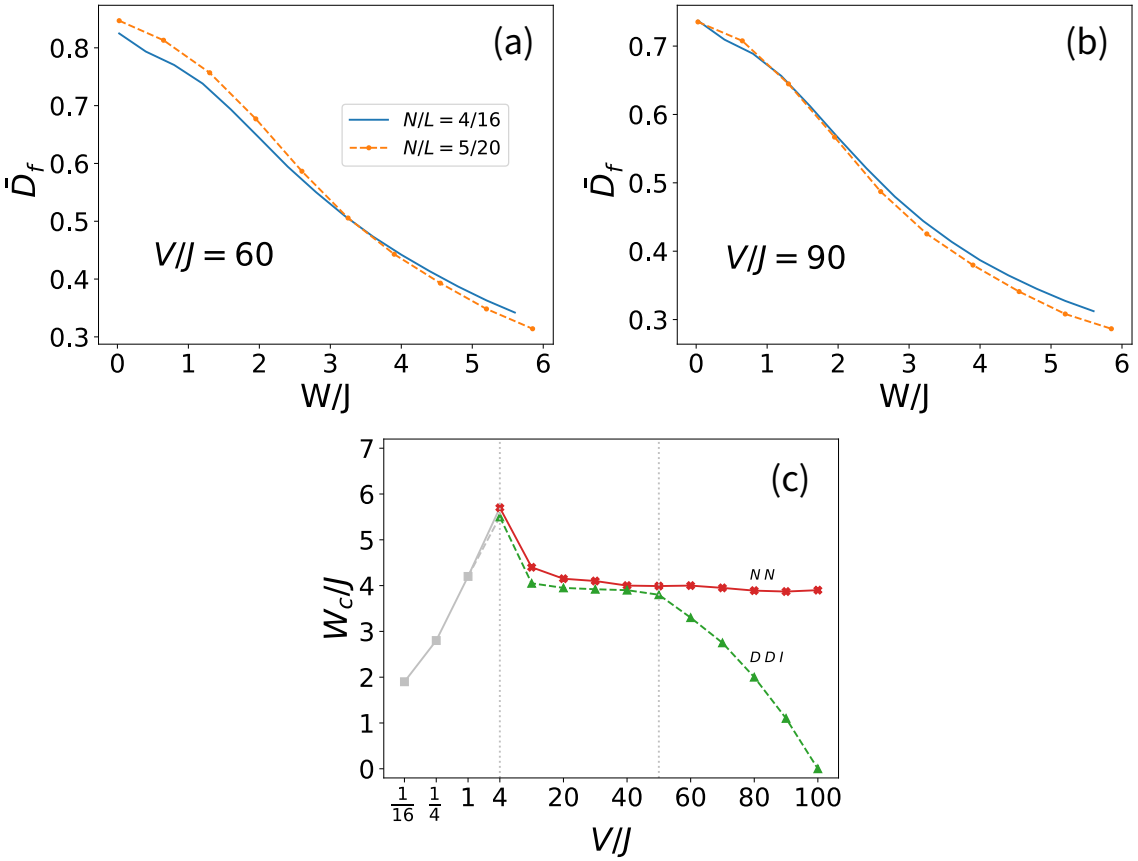

Figure C.2: (a), (b) Curves of $\bar{D}_f$ for different $\rho = 1/4$ lattices, the average is obtain the flat part of IPR_f in the $l = 0$ fragment (see the main text). (c) The critical disorder,W_c, as a function of V, for the nearest-neoghbor model, and for polar lattice gases.

Note that the flat part of IPR_f shrink as V/J increases, estimations are made within the regimes where the averaged D_f are stable. For $V/J \lesssim 4$, the full fragment is flat since there is no shattering effect, the average is taken over all D_f in the fragment. For $V/J = 10$ and 20, the shattering effect is weak, the flat accounts for $\sim 80\%$ of the fragment, and for $V/J = 30$ and 40, the shattering becomes obvious, the rate reduces to $\sim 45\%$ and $\sim 40\%$ respectively, and for $V/J \gtrsim 50$, where the shattering is severe, the rate is $\sim 30\%$. For each V/J, the intersections are stable when changing the corresponding percentage by $\sim \pm 2\%$.

Appendix D

Dimer bands for hard-core bosons in square lattices

In this Appendix we evaluate the band structure of the peculiar decorated square lattice (Fig. 6.8 (a)) that characterizes the dimer motion in hard-core systems of polar particles in a square lattice. The decorated lattice possess four-site unit cells, with inter-cell primitive vectors $\mathbf{a}_0 = \mathbf{e}_x$ and $\mathbf{a}_1 = \mathbf{e}_y$. This implies that the first Brillouin zone and the symmetry points are similar to those of an ordinary square lattice, i.e., $\Gamma = (0,0)$, $M = (\pi, 0)$, and $K = (\pi, \pi)$ (see Fig. D.1 (a)).

Let $\hat{d}^n_{\mathbf{j}}$ denote the dimer operator whose center of mass locates at the n^{th} site of the unit cell $\mathbf{j}$. The four internal states can be presented by the vector operator

$$\vec{d}_{\mathbf{j}} = \begin{pmatrix} \hat{d}^0_{\mathbf{j}} \\ \hat{d}^1_{\mathbf{j}} \\ \hat{d}^2_{\mathbf{j}} \\ \hat{d}^3_{\mathbf{j}} \end{pmatrix}. \tag{D.1}$$

The effective Hamiltonian describing the decorated square lattice is $H_{DS} = H_{\text{cell}} + \sum_{\mathbf{v}} H_{\mathbf{v}}$, where

$$H_{\text{cell}} = -J' \sum_{\mathbf{j}} \vec{d}^{\,\dagger}_{\mathbf{j}} \begin{pmatrix} 0 & 1 & 1 & 1 \\ 1 & 0 & 1 & 1 \\ 1 & 1 & 0 & 1 \\ 1 & 1 & 1 & 0 \end{pmatrix} \vec{d}_{\mathbf{j}}, \tag{D.2}$$

is given by the in-cell couplings, and $H_{\mathbf{v}}$ is the inter-cell hopping along the vector $\mathbf{v}$. There

are four cases, $\mathbf{v}_0 = \mathbf{e}_x$, $\mathbf{v}_1 = \mathbf{e}_y$, $\mathbf{v}_2 = \mathbf{e}_x + \mathbf{e}_y$, and $\mathbf{v}_3 = \mathbf{e}_x - \mathbf{e}_y$:

$$H_{\mathbf{v}_0} = -\sum_{\mathbf{j}} \left[J'(\hat{d}^{1\dagger}_{\mathbf{j}+\mathbf{e}_x} \hat{d}^{0}_{\mathbf{j}} + \hat{d}^{2\dagger}_{\mathbf{j}+\mathbf{e}_x} \hat{d}^{3}_{\mathbf{j}} + \text{H.c.}) + J''(\hat{d}^{2\dagger}_{\mathbf{j}+\mathbf{e}_x} \hat{d}^{0}_{\mathbf{j}} + \hat{d}^{1\dagger}_{\mathbf{j}+\mathbf{e}_x} \hat{d}^{3}_{\mathbf{j}} + \text{H.c.}) \right], \tag{D.3}$$

$$H_{\mathbf{v}_1} = -\sum_{\mathbf{j}} \left[J'(\hat{d}^{3\dagger}_{\mathbf{j}+\mathbf{e}_y} \hat{d}^{0}_{\mathbf{j}} + \hat{d}^{2\dagger}_{\mathbf{j}+\mathbf{e}_y} \hat{d}^{1}_{\mathbf{j}} + \text{H.c.}) + J''(\hat{d}^{2\dagger}_{\mathbf{j}+\mathbf{e}_y} \hat{d}^{0}_{\mathbf{j}} + \hat{d}^{3\dagger}_{\mathbf{j}+\mathbf{e}_y} \hat{d}^{1}_{\mathbf{j}} + \text{H.c.}) \right], \tag{D.4}$$

$$H_{\mathbf{v}_2} = -J' \sum_{\mathbf{j}} (\hat{d}^{2\dagger}_{\mathbf{j}+\mathbf{e}_x+\mathbf{e}_y} \hat{d}^{0}_{\mathbf{j}} + \text{H.c.}), \tag{D.5}$$

$$H_{\mathbf{v}_3} = -J' \sum_{\mathbf{j}} (\hat{d}^{1\dagger}_{\mathbf{j}+\mathbf{e}_x-\mathbf{e}_y} \hat{d}^{3}_{\mathbf{j}} + \text{H.c.}). \tag{D.6}$$

We may represent each cell using the basis of local eigenstates (i.e., the eigenstates of H_{cell}): $\vec{d_{\mathbf{j}}} = U \cdot \vec{a}_{\mathbf{j}}$, where

$$U = \frac{1}{2} \begin{pmatrix} 1 & 1 & 1 & 1 \\ 1 & 1 & -1 & -1 \\ 1 & -1 & 1 & -1 \\ 1 & -1 & -1 & 1 \end{pmatrix}. \tag{D.7}$$

This leads to the Hamiltonian for the decorated lattice

$$H_{DS} = -J'\lambda - \frac{J'}{2} \sum_{\mathbf{v}} \left(\vec{a}^{\,\dagger}_{\mathbf{j}+\mathbf{v}} M_{\mathbf{v}} \vec{a}_{\mathbf{j}} + \vec{a}_{\mathbf{j}}{}^{\dagger} M^T_{\mathbf{v}} \vec{a}_{\mathbf{j}+\mathbf{v}} \right), \tag{D.8}$$

where

$$\lambda = \begin{pmatrix} 3 & 0 & 0 & 0 \\ 0 & -1 & 0 & 0 \\ 0 & 0 & -1 & 0 \\ 0 & 0 & 0 & -1 \end{pmatrix}, \tag{D.9}$$

$$M_{\mathbf{v}_0} = \begin{pmatrix} 1+\gamma & 0 & 0 & -(1+\gamma) \\ 0 & 1-\gamma & -(1-\gamma) & 0 \\ 0 & 1-\gamma & -(1-\gamma) & 0 \\ 1+\gamma & 0 & 0 & -(1+\gamma) \end{pmatrix}, \tag{D.10}$$

$$M_{\mathbf{v}_1} = \begin{pmatrix} 1+\gamma & -(1+\gamma) & 0 & 0 \\ 1+\gamma & -(1+\gamma) & 0 & 0 \\ 0 & 0 & -(1-\gamma) & 1-\gamma \\ 0 & 0 & -(1-\gamma) & 1-\gamma \end{pmatrix}, \tag{D.11}$$

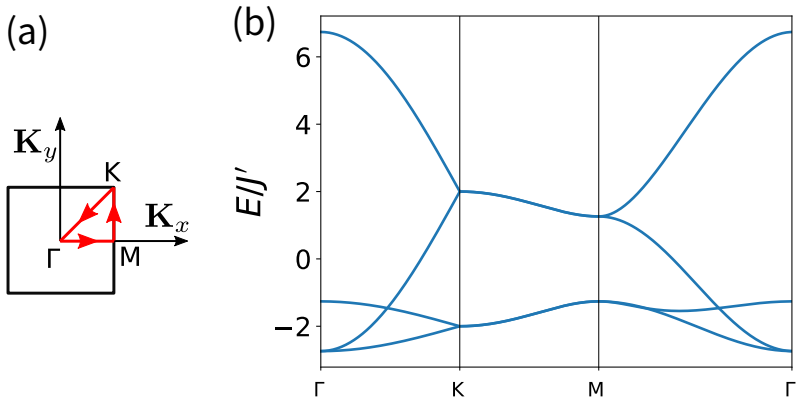

Figure D.1: (a) The first Brillouin zone of the decorated square lattice. (b) The four bands given by Eq. (D.14). The two relatively flat bands have width $\sim 2J'$, while the others have width $\sim 10J'$, thus two timescales are expected for a dimer of hard-core particles expanding in square lattices.

$$M_{\mathbf{v}_1} = \frac{1}{2}\begin{pmatrix} 1 & -1 & 1 & -1 \\ 1 & -1 & 1 & -1 \\ 1 & -1 & 1 & -1 \\ 1 & -1 & 1 & -1 \end{pmatrix}, \tag{D.12}$$

$$M_{\mathbf{v}_3} = \frac{1}{2}\begin{pmatrix} 1 & 1 & -1 & -1 \\ -1 & -1 & 1 & 1 \\ -1 & -1 & 1 & 1 \\ 1 & 1 & -1 & -1 \end{pmatrix}. \tag{D.13}$$

and $\gamma = J''/J' \sim 0.369$.

For a given quasi-momentum, $\mathbf{K}$, the Fourier transform $\vec{a}_{\mathbf{j}} = \frac{1}{\sqrt{\Omega}} e^{i\mathbf{K}\cdot\mathbf{j}} \vec{a}_{\mathbf{K}}$ gives $H_{DS}(\mathbf{K})$ as a 4×4 matrix,

$$H_{DS}(\mathbf{K}) = -J\lambda - \frac{J'}{2}\sum_{n=0}^{3} e^{-i\mathbf{K}\cdot\mathbf{v}_n} M_{\mathbf{v}_n} + e^{i\mathbf{K}\cdot\mathbf{v}_n} M_{\mathbf{v}_n}^T. \tag{D.14}$$

Along the high symmetry points the matrix decouples into two 2×2 matrices, where the diagonalization becomes simple. For $\mathbf{K}$ along $\Gamma \to M$ dispersion is $E(\mathbf{K})/J' = -2 \pm 2\gamma\cos(\frac{\mathbf{K}}{2})$ and $2 \pm (4 + 2\gamma)\cos(\frac{\mathbf{K}}{2})$, whereas for $\mathbf{K}$ along $M \to K$ the dispersion is $\pm 2\sqrt{1 - (2\gamma - \gamma^2)\sin^2(\frac{\mathbf{K}}{2})}$ (see Fig. D.1 (b)).

Bibliography

[1] I. Bloch, J. Dalibard, and W. Zwerger, Rev. Mod. Phys. **80**, 885 (2008).

[2] I. Georgescu, S. Ashhab, and F. Nori, Rev. Mod. Phys. **86**, 153 (2014).

[3] I. Bloch, J. Dalibard and S. Nascimbène, Nature Phys. **8**, 267 (2012).

[4] J. Cirac or P. Zoller, Nature Phys. **8**, 264 (2012).

[5] Ph. Courteille, *et al.*, Phys. Rev. Lett. **81**, 69 (1998).

[6] S. Inouye, *et al.*, Nature **392**, 151 (1998).

[7] C. Gross, and I. Bloch, Science **357**, 995 (2017).

[8] F. Schäfer, *et al.*, Nat. Rev. Phys. **2**, 411 (2020).

[9] C. Becker, *et al.*, New J. of Phys. **12**, 065025 (2010).

[10] G-B. Jo, *et al.*, Phys. Rev. Lett. **108**, 045305 (2012).

[11] L. Tarruell, *et al.*, Nature **483**, 302 (2012).

[12] K. Viebahn, *et al.*, Phys. Rev. Lett. **122**, 110404 (2019).

[13] M. Greiner, O. Mandel, T. Esslinger, T. Hänsch and I. Bloch, Nature **415**, 39 (2002).

[14] T. Stöferle, *et al.*, Phys. Rev. Lett. **92**, 130403 (2004).

[15] I. Spielman, W. Phillips, and J. Porto, Phys. Rev. Lett. **98**, 080404 (2007).

[16] M. Köhl, *et al.*, Phys. Rev. Lett. **94**, 080403 (2005).

[17] T. Esslinger, Annu. Rev. Condens. Mat. Phys. **1**, 129 (2010).

[18] T. Fukuhara, *et al.*, Nature **502**, 76 (2013).

[19] S. Hild, *et al.*, Phys. Rev. Lett. **113**, 147205 (2014).

[20] P. Jepsen, *et al.*, Nature **588**, 403 (2020).

[21] F. Görg, *et al.*, Nature **553**, 481 (2018).

[22] P. Jessen, and I. H. Deutsch, Adv. At., Mol., Opt. Phys. **37**, 95 (1996).

[23] W. Zwerger, J. Opt. B: Quantum Semiclass. Opt. **5** S9 (2003).

[24] C. Chin, R. Grimm, P. Julienne, and E. Tiesinga, Rev. Mod. Phys. **82**, 1225 (2010).

[25] M. Aizenman, *et al.*, Phys. Rev. A **70**, 023612 (2004).

[26] S. Fölling, *et al.*, Phys. Rev. Lett. **97**, 060403 (2006).

[27] G. Campbell, *et al.*, Science **313**, 649 (2006).

[28] J. Sherson, *et al.*, Nature **467**, 68 (2010).

[29] W. Bakr, *et al.*, Science **329**, 547 (2010).

[30] R. Jördens, *et al.*, Nature **455**, 204 (2008).

[31] U. Schneider, *et al.*, Science **322**, 1520 (2008).

[32] S. Trotzky, *et al.*, Science **319**, 295 (2007).

[33] A. B. Kuklov and B. V. Svistunov, Phys. Rev. Lett. **90**, 100401 (2003).

[34] L.-M. Duan, E. Demler, and M. D. Lukin, Phys. Rev. Lett. **91**, 090402 (2003).

[35] A. Mazurenko, *et al.*, Nature **545**, 462 (2017).

[36] R. Blatt and C. F. Roos, Nat. Phys. **8**, 277 (2012).

[37] P. Richerme, *et al.*, Nature **511**, 198 (2014).

[38] M. Saffman, T. G. Walker, and K. Mølmer, Rev. Mod. Phys. **82**, 2313 (2010).

[39] A. Browaeys and T. Lahaye, *Interacting cold Rydberg atoms: A toy many-body system*. The article is collected in the book *Niels Bohr, 1913-2013* edited by O. Darrigol, *et al.*, Springer Publishing (2016), as a part of the book series Progress in Mathematical Physics (volume 68).

[40] T. Lahaye, C. Menotti, L. Santos, M. Lewenstein, and T. Pfau, Rep. Prog. Phys. **72**, 126401 (2009).

[41] A. de Paz, *et al.*, Phys. Rev. Lett. **111**, 185305 (2013).

[42] B. Yan, *et al.*, Nature **501**, 521 (2013).

[43] S. Ospelkaus, *et al.*, Science **327**, 853 (2010).

[44] M. Mayle, G. Quéméner, B. P. Ruzic, and J. L. Bohn, Phys. Rev. A **87**, 012709 (2013).

[45] L. De Marco, *et al.*, Science **363**, 853 (2019).

[46] J-R. Li, *et al.*, Nature Phys. **17**, 1144 (2021).

[47] S. Baier, *et al.*, Science **352**, 201 (2016).

[48] K. Aikawa, A. Frisch, M. Mark, S. Baier, R. Grimm, and F. Ferlaino, Phys. Rev. Lett. **112**, 010404 (2014).

[49] S. Hensler, *et al.*, Appl. Phys. B **77**, 765 (2003).

[50] T. Sowinski, O. Dutta, P. Hauke, L. Tagliacozzo, and M. Lewenstein, Phys. Rev. Lett. **108**, 115301 (2012).

[51] P. Sengupta, L. Pryadko, F. Alet, M. Troyer, and G. Schmid, Phys. Rev. Lett. **94**, 207202 (2005).

[52] E. Dalla Torre, E. Berg, and E. Altman, Phys. Rev. Lett. **97**, 260401 (2006).

[53] A. Pikovski, M. Klawunn, G. Shlyapnikov, and L. Santos, Phys. Rev. Lett. **105**, 215302 (2010).

[54] A. Argüelles and L. Santos. Phys. Rev. A **75**, 053613 (2007).

[55] C. Trefzger, C. Menotti, and M. Lewenstein, Phys. Rev. Lett. **103**, 035304 (2009).

[56] D-W. Wang, M. Lukin, and E. Demler, Phys. Rev. Lett. **97**, 180413 (2006).

[57] M. Klawunn, J. Duhme, and L. Santos, Phys. Rev. A **81**, 013604 (2010).

[58] M. Baranov, M. Dalmonte, G. Pupillo, and P. Zoller, Chem. Rev. **112**, 5012 (2012).

[59] T. Kinoshita, T. Wenger and D. Weiss, Nature **440**, 900 (2006).

[60] E. H. Lieb and W. Liniger, Phys. Rev. **130**, 1605 (1963)

[61] M. Gring, *et al.*, Science **337**, 1318 (2012).

[62] S. Trotzky, *et al.*, Nature Phys. **8**, 325 (2012).

[63] M. Cheneau, *et al.*, Nature **481**, 484 (2012).

[64] U. Schneider, *et al.*, Nature Phys. **8**, 213 (2012).

[65] K. Winkler, *et al.*, Nature **441**, 853 (2006).

[66] F. Jendrzejewski, *et al.*, Nat. Phys. **8**, 398 (2012).

[67] C. D' Errico, *et al.*, Phys. Rev. Lett. **113**, 095301 (2014).

[68] M. Schreiber, *et al.*, Science **349**, 842 (2015).

[69] J. Choi, *et al.*, Science **352**, 1547 (2016).

[70] S. Kuhr, Natl. Sci. Rev., **3**, 170 (2016)

[71] C. Gross and W. Bakr, arXiv:2010.15407.

[72] A. Polkovnikov, K. Sengupta, A. Silva, and M. Vengalattore, Rev. Mod. Phys. **83**, 863 (2011).

[73] J. Eisert, M. Friesdorf and C. Gogolin , Nature Phys. **11**, 124 (2015).

[74] F. Borgonovi F. Izrailev L. Santos V. Zelevinsky, Phys. Rep. **626**, 1 (2016).

[75] P. Jurcevic, *et al.*, Nature (London) **511**, 202 (2014).

[76] M. Gärttner, *et al.*, Nature Phys. **13**, 781 (2017).

[77] J. Deutsch, Phys. Rev. A **43**, 2046 (1991).

[78] M. Srednicki, Phys. Rev. E **50**, 888 (1994).

[79] H. Tasaki, Phys. Rev. Lett. **80**, 1373 (1998).

[80] M. Rigol, V. Dunjko and M. Olshanii, Nature **452**, 854 (2008).

[81] B. Sutherland, *Beautiful Models, Ch. 2*, World Scientific, (2004).

[82] B. Sutherland, *Beautiful Models, Ch. 6*, World Scientific, (2004).

[83] *Yang-Baxter Equation in Integrable Systems*, edited by M. Jimbo, World Scientific (1990).

[84] M. Jimbo and T. Miwa, *Algebraic analysis of solvable lattice models*, American Mathematical Society (1993).

[85] R. Nandkishore and D. Huse, Annu. Rev. Condens. Mat. Phys. **6**, 15 (2015).

[86] L. Fleishman and P. W. Anderson, Phys. Rev. B **21**, 2366 (1980).

[87] I. Gornyi, A. Mirlin, and D. Polyakov, Phys. Rev. Lett. **95**, 206603 (2005).

[88] D. Basko, I. Aleiner, and B. Altshuler, Ann. Phys. **321**, 1126 (2006).

[89] G. Carleo, F. Becca, M. Schiró, and M. Fabrizio, Sci. Rep. **2**, 243 (2012).

[90] M. van Horssen, E. Levi, and J. Garrahan Phys. Rev. B **92**, 100305(R) (2015).

[91] J. Hickey, S. Genway and J. Garrahan, J. Stat. Mech. 054047 (2016).

[92] Z. Lan, M. van Horssen, S. Powell, and J. Garrahan, Phys. Rev. Lett. **121**, 040603 (2018).

[93] J. Feldmeier, F. Pollmann, and M. Knap, Phys. Rev. Lett. **123**, 040601 (2019).

[94] T. Grover, M. Fisher, J. Stat. Mech. 10010 (2014).

[95] M. Schiulaz, A. Silva, and M. Müller Phys. Rev. B **91**, 184202 (2015).

[96] Z. Papić, E. Stoudenmire, and D. Abanin, Ann. Phys. **362**, 714 (2015).

[97] L. Barbiero, C. Menotti, A. Recati, and L. Santos, Phys. Rev. B **92**, 180406(R) (2015).

[98] A. Smith, J. Knolle, D.L. Kovrizhin, and R. Moessner, Phys. Rev. Lett. **118**, 266601 (2017).

[99] R. Mondaini and Z. Cai, Phys. Rev. B **96**, 035153 (2017).

[100] M. Schulz, C. Hooley, R. Moessner, and F. Pollmann, Phys. Rev. Lett. **122**, 040606 (2019).

[101] E. van Nieuwenburga, Y. Bauma, and G. Refaela, PNAS. **116**, 9269 (2019).

[102] S.Taylor, M. Schulz, F. Pollmann, and R. Moessner, Phys. Rev. B **102**, 054206 (2020).

[103] T. Chanda, R. Yao, and J. Zakrzewski, Phys. Rev. Research **2**, 032039(R) (2020).

[104] R. Yao and J. Zakrzewski, Phys. Rev. B **102,** 104203 (2020).

[105] S. Scherg, *et al.*, Nat Commun. **12**, 4490 (2021).

[106] Q. Guo, *et al.*, arXiv:2011.13895.

[107] W. Morong, *et al.*, arXiv:2102.07250.

[108] R. Yao, T. Chanda, and J. Zakrzewski, arXiv:2101.11061.

[109] J. von Neumann, Z. Phys. **57**, 30 (1929), translated to English in Eur. Phys. J. H **35**, 201 (2010).

[110] M. Srednicki, J. Phys. A **29**, L75 (1996).

[111] M. Srednicki, J. Phys. A **32**, 1163 (1999).

[112] L. D'Alessio, Y. Kafri, A. Polkovnikov, and M. Rigol, Adv. Phys. **65**, 239 (2016).

[113] H. Goldstein, C. Poole and J. Safko, *Classical Mechanics Ch. 10 and Ch. 11*, third edition, Person Education (2002).

[114] P. Calabrese, F. Essler and G. Mussardo, J. Stat. Mech. 064001 (2016); P. Calabrese, F. Essler and M. Fagotti, Phys. Rev. Lett. 106 227203 (2011); P. Calabrese, F. Essler and M. Fagotti, Stat. Mech. 07022 (2012).

[115] F. Essler and M. Fagotti, J. Stat. Mech. 064002 (2016).

[116] E.A. Yuzbashyan, Ann. Phys. **367**, 288 (2016).

[117] L. Vidmar and M. Rigol, J. Stat. Mech. 064007 (2016).

[118] C-N. Yang and C-P. Yang, Phys. Rev. **150**, 321 (1966); **150**, 327 (1966); **151**, 258 (1966).

[119] S. Mukerjee, V. Oganesyan, and D. Huse, Phys. Rev. B **73**, 035113 (2006).

[120] L. Santos and M. Rigol, Phys. Rev. E **81**, 036206 (2010).

[121] E. Khatami, G. Pupillo, M. Srednicki and M. Rigol, Phys. Rev. Lett. **111**, 050403 (2013).

[122] R. Pathria and P. Beale *Statistical Mechanics, Ch. 2*, third edition, Elsevier/Academic Press (2011).

[123] T. Guhr, A. Müller-Groeling and H.A. Weidenmüller, Phys. Rep. **299**, 189 (1998).

[124] M. Mehta, *Random Matrices*, third edition, Elsevier/Academic Press, (2004).

[125] V. Kravtsov, arXiv:0911.0639 (2012).

[126] F. Haake, *Quantum Signatures of Chaos*, Springer (2010).

[127] H.-J. Stöckmann, *Quantum Signatures: An Introduction*, Cambridge University Press (2009).

[128] O. Bohigas, M.J. Giannoni and C. Schmit, Phys. Rev. Lett. **52**, 1 (1984).

[129] E. Bogomolny, B. Georgeot, M-J. Giannoni and C. Schmit, Phys. Rev. Lett. **69**, 1477 (1992).

[130] M. Berry, J. Phys. A **10**, 2083 (1977).

[131] M. Hillery, R.F. O'Connell, M.O. Scully and E.P. Wigner, Phys. Rep. **106**, 121 (1984).

[132] A. Polkovnikov, Ann. Phys. **325**, 1790 (2010).

[133] M. Berry and M. Tabor, Proc. Roy. Soc. A **356**, 375 (1977).

[134] A. Pandey and R. Ramaswamy, Phys. Rev. A **43**, 4237 (1991).

[135] K. Kudo and T. Deguchi, J. Phys. Soc. Jpn. **74**, 1992 (2005).

[136] D. Poilblanc, *et al.*, Europhys. Lett. **22**, 537 (1993).

[137] P. W. Anderson, Phys. Rev. **109**, 1492 (1958).

[138] J. Šuntajs, *et al.*, Phys. Rev. E **102**, 062144 (2020).

[139] R. Panda, *et al.*, EPL (Europhysics Letters) **128**, 67003 (2020).

[140] D. Abanin, *et al.*, Annals of Physics **427**, 168415 (2021).

[141] P. Sierant and J. Zakrzewski, arXiv:2109.13608 (2021).

[142] V. Oganesyan and D. Huse, Phys. Rev. B **75**, 155111 (2007).

[143] A. Pal and D. Huse, Phys. Rev. B **82**, 174411 (2010).

[144] J. Imbrie, J. Stat. Phys. **163**, 998 (2016).

[145] J. Billy, *et al.*, Nature (London) **453**, 891 (2008).

[146] G. Roati, *et al.*, Nature (London) **453**, 895 (2008).

[147] B. Deissler, *et al.*, Nat. Phys. **6**, 354 (2010).

[148] S. Kondov, W. McGehee, J. Zirbel, and B. DeMarco, Science **334**, 66 (2011).

[149] J. Imbrie , V. Ros, and A. Scardicchio, Ann. Phys. (Berlin) **529**, 1600278 (2017).

[150] M. Serbyn, Z. Papić, and D. Abanin, Phys. Rev. Lett. **111**, 127201 (2013).

[151] M. Serbyn, Z. Papić, and D. A. Abanin, Phys. Rev. B **90**, 174302 (2014).

[152] D. Huse, R. Nandkishore, and V. Oganesyan, Phys. Rev. B **90**, 174202 (2014).

[153] A. Chandran, I. Kim, G. Vidal, and D. Abanin, Phys. Rev. B **91**, 085425 (2015).

[154] M. Žnidarič, T. Prosen, and P. Prelovšek Phys. Rev. B **77**, 064426 (2008).

[155] J. Bardarson, F. Pollmann, and J. Moore, Phys. Rev. Lett. **109**, 017202 (2012).

[156] Y. Kagan, L. Maksimov, Zh. Eksp. Teor. Fiz. **87**, 348 (1984).

[157] Y. Kagan, L. Maksimov, Sov. Phys. JETP **60**, 201 (1984).

[158] N. Strohmaier et al., Phys. Rev. Lett. **104**, 080401 (2010).

[159] J. Ronzheimer, *et al.*, Phys. Rev. Lett. **110**, 205301 (2013).

[160] M. Valiente and D. Petrosyan, J. Phys. B **42**, 121001 (2009).

[161] J-P. Nguenang and S. Flach, Phys. Rev. A **80**, 015601 (2009).

[162] W. Li, *et al.*, Phys. Rev. Lett. **124**, 010404 (2020).

[163] R. Feynman, R. Leighton and M. Sands, Feynman Lecture on Physics, III Ch. 13.8, California Institute Of Technology (1965).

[164] D. Petrosyan, B. Schmidt, J. R. Anglin, and M. Fleischhauer, Phys. Rev. A **76**, 033606 (2007).

[165] M. Wall and L. Carr, New J. Phys. **14**, 125015 (2012).

[166] Y. Bar Lev, G. Cohen, and D. Reichman, Phys. Rev. Lett. **114**, 100601 (2015).

[167] G. De Tomasi, D. Hetterich, P. Sala, and F. Pollmann, Phys. Rev. B **100**, 214313 (2019).

[168] P. Sala, T. Rakovszky, R. Verresen, M. Knap, and F. Pollmann, Phys. Rev. X **10**, 011047 (2020).

[169] Z-C. Yang, F. Liu, A. Gorshkov, and T. Iadecola, Phys. Rev. Lett. **124**, 207602 (2020).

[170] V. Khemani, M. Hermele, and R. Nandkishore, Phys. Rev. B **101**, 174204 (2020).

[171] F. Pietracaprina and N. Laflorencie, Ann. Phys. 168502 (2021).

[172] L. Herviou, J. Bardarson, and N. Regnault, Phys. Rev. B **103**, 134207 (2021).

[173] S. Moudgalya, B. Bernevig, N. Regnault, arXiv:2109.00548.

[174] C. Turner, A. Michailidis, D. Abanin, M. Serbyn, and Z. Papić, Phys. Rev. B **98**, 155134, (2018).

[175] H. Bernien, *et al.*, Nature **551**, 579 (2017).

[176] M. Aizenman and S. Warzel, Commun. Math. Phys. **290**, 903 (2009).

[177] A. De Luca, and A. Scardicchio, Europhys. Lett. 101, 37003 (2013).

[178] R. Dias, Phys. Rev. B **62**, 7791 (2000).

[179] F. Evers and A. Rev. Mod. Phys. **80**, 1355 (2008).

[180] N Macé, F. Alet, and N. Laflorencie, Phys. Rev. Lett. **123**, 180601 (2019).

[181] X. Deng, G. Masella, G. Pupillo, and L. Santos, Phys. Rev. Lett. **125**, 010401 (2020).

[182] W. Li, X. Deng, and L. Santos, arXiv:2103.13780.

[183] A. Frisch, *et al.*, Phys. Rev. Lett. **115**, 203201 (2015).

[184] W. Yi, A. J. Daley, G. Pupillo, and P. Zoller, New J. Phys. **10**, 073015 (2008).

[185] S. Nascimbene, N. Goldman, N. Cooper, and J. Dalibard, Phys. Rev. Lett. **115**, 140401 (2015).

[186] S. Moses, J. Covey, M. Miecnikowski, D. Jin, and J. Ye, Nature Phys. **13**, 13 (2017).

[187] G. Salerno, G. Palumbo, N. Goldman, and M. Di Liberto, Phys. Rev. Res. **2**, 013348 (2020).

[188] W. Li, A. Dhar, X. Deng, and L. Santos, Phys. Rev. A **103**, 043331 (2021).

[189] D. Leykam, A. Andreanov, and S. Flach, Adv. Phys.: X **3**, 1473052 (2018).

[190] The TDVP calculations were performed using the TENPY Library (version 0.5.0) [191].

[191] J. Hauschild and F. Pollmann, SciPost Phys. Lect. Notes **5** (2018).

Related Publications

Disorderless quasi-localization of polar gases in one-dimensional lattices
Wei-Han Li, A. Dhar, X. Deng, K. Kasamatsu, L. Barbiero, and L. Santos, Phys. Rev. Lett. **124**, 010404 (2020).

Cluster dynamics in two-dimensional lattice gases with inter-site interactions,
Wei-Han Li, A. Dhar, X. Deng, and L. Santos, Phys. Rev. A **103**, 043331 (2021).

Hilbert space shattering and disorder-free localization in polar lattice gases,
Wei-Han Li, X. Deng, and L. Santos, arXiv:2103.13780 (accepted in Phys. Rev. Lett.).

Wei-Han Li
Email: wei-han.li@itp.uni-hannover.de